

# Using effective field theory to analyse low-energy Compton scattering data from protons and light nuclei

H. W. Griebhammer<sup>1</sup>, J. A. McGovern<sup>2</sup>,  
D. R. Phillips<sup>3</sup> and G. Feldman<sup>1</sup>

<sup>1</sup>Institute for Nuclear Studies, Department of Physics,  
The George Washington University, Washington DC 20052, USA

<sup>2</sup>Theoretical Physics Group, School of Physics and Astronomy,  
The University of Manchester, Manchester, M13 9PL, UK

<sup>3</sup>Institute of Nuclear and Particle Physics and Department of  
Physics and Astronomy, Ohio University, Athens OH 45701, USA

November 2, 2018

## Abstract

Compton scattering from protons and neutrons provides important insight into the structure of the nucleon. For photon energies up to about 300 MeV, the process can be parameterised by six dynamical dipole polarisabilities which characterise the response of the nucleon to a monochromatic photon of fixed frequency and multipolarity. Their zero-energy limit yields the well-known static electric and magnetic dipole polarisabilities  $\alpha_{E1}$  and  $\beta_{M1}$ , and the four dipole spin polarisabilities. The emergence of full lattice QCD results and new experiments at MAMI (Mainz), HI $\gamma$ S at TUNL, and MAX-Lab (Lund) makes this an opportune time to review nucleon Compton scattering. Chiral Effective Field Theory ( $\chi$ EFT) provides an ideal analysis tool, since it encodes the well-established low-energy dynamics of QCD while maintaining an appropriately flexible form for the Compton amplitudes of the nucleon. The same  $\chi$ EFT also describes deuteron and <sup>3</sup>He Compton scattering, using consistent nuclear currents, rescattering and wave functions, and respects the low-energy theorems for photon-nucleus scattering. It can thus also be used to extract useful information on the neutron amplitude from Compton scattering on light nuclei. We summarise past work in  $\chi$ EFT on all of these reactions and compare with other theoretical approaches. We also discuss all proton experiments up to about 400 MeV, as well as the three modern elastic deuteron data sets, paying particular attention to the precision and accuracy of each set. Constraining the  $\Delta(1232)$  parameters from the resonance region, we then perform new fits to the proton data up to  $\omega_{\text{lab}} = 170$  MeV, and a new fit to the deuteron data. After checking in each case that a two-parameter fit is compatible with the respective Baldin sum rules, we obtain, using the sum-rule constraints in a one-parameter fit,  $\alpha_{E1}^{(p)} = 10.7 \pm 0.3(\text{stat}) \pm 0.2(\text{Baldin}) \pm 0.8(\text{theory})$ ,  $\beta_{M1}^{(p)} = 3.1 \mp 0.3(\text{stat}) \pm 0.2(\text{Baldin}) \pm 0.8(\text{theory})$ , for the proton polarisabilities, and  $\alpha_{E1}^{(s)} = 10.9 \pm 0.9(\text{stat}) \pm 0.2(\text{Baldin}) \pm 0.8(\text{theory})$ ,  $\beta_{M1}^{(s)} = 3.6 \mp 0.9(\text{stat}) \pm 0.2(\text{Baldin}) \pm 0.8(\text{theory})$ , for the isoscalar polarisabilities, each in units of  $10^{-4} \text{ fm}^3$ . Finally, we discuss plans for polarised Compton scattering on the proton, deuteron, <sup>3</sup>He and heavier targets, their promise as tools to access spin polarisabilities, and other future avenues for theoretical and experimental investigation.

Keywords: Compton scattering, proton, neutron and nucleon polarisabilities, spin polarisabilities, Chiral Perturbation Theory, Effective Field Theory,  $\Delta(1232)$  resonance

# Contents

<b>1</b>	<b>Introduction</b>	<b>3</b>
1.1	<i>The importance of dipole electric and magnetic polarisabilities</i>	3
1.2	<i>Compton scattering from nucleons: data, structure and analysis tools</i>	5
1.3	<i>The role of Effective Field Theory</i>	6
1.4	<i>The elusive neutron: Compton scattering from light nuclei</i>	7
1.5	<i>Results and the future</i>	8
<b>2</b>	<b>Foundations</b>	<b>9</b>
2.1	<i>Overview</i>	9
2.2	<i>Polarisabilities from a multipole expansion</i>	11
2.3	<i>Kinematics</i>	13
2.4	<i>Observables</i>	14
<b>3</b>	<b>Experimental overview</b>	<b>16</b>
3.1	<i>Low-energy proton Compton scattering</i>	17
3.2	<i>High-energy proton Compton scattering</i>	19
3.3	<i>A critical look at the proton data</i>	22
3.4	<i>Low-energy deuteron elastic Compton scattering</i>	25
3.5	<i>Deuteron quasi-free Compton scattering</i>	28
<b>4</b>	<b>Compton scattering from the nucleon</b>	<b>29</b>
4.1	<i>Dispersion relations</i>	29
4.2	<i>Chiral EFT for <math>\gamma p</math> and <math>\gamma n</math> scattering</i>	33
4.3	<i>Comparing <math>\chi EFT</math> with Dispersion Relations</i>	44
4.4	<i>A new fit to the proton data</i>	46
4.5	<i>Other methods</i>	49
<b>5</b>	<b>Compton scattering from two- and three-nucleon systems</b>	<b>51</b>
5.1	<i><math>\chi EFT</math> for few-nucleon systems</i>	52
5.2	<i>Compton scattering from the deuteron in <math>\chi EFT</math></i>	52
5.3	<i>A new fit to the deuteron data</i>	60
5.4	<i>EFTs for very low energies</i>	63
5.5	<i>Deuteron Compton scattering: model calculations</i>	66
5.6	<i>Compton scattering from <math>^3\text{He}</math></i>	67
<b>6</b>	<b>The future</b>	<b>68</b>
6.1	<i>The case for investigating spin polarisabilities</i>	68
6.2	<i>Experiment</i>	70
6.3	<i>Theory</i>	71
6.4	<i>Conclusion</i>	73

# 1 Introduction

Compton scattering has played a major role in the development of modern Physics. In 1871, Lord Rayleigh employed the recently discovered nature of light as an electromagnetic wave to demonstrate that the cross section for light scattering with frequency  $\omega$  from neutral atoms behaves as  $\sigma \propto \omega^4$ , thereby explaining why the sky is blue [1, 2]. Fifty-six years later, Arthur Holly Compton won the Nobel Prize “for his discovery of the effect named after him”: X-rays have a longer wavelength after they are scattered from electrons, with the difference precisely predicted by a quantum treatment of the electromagnetic radiation and by the relativistic kinematics of the electron [3]. Compton’s experiment thus provided a unified demonstration of two of the great advances in Physics in the early 20th century: relativity and the particle-like nature of light.

In 1935, Bethe and Peierls performed the first calculation of Compton scattering from a nucleus: the deuteron [4]. The field gained momentum in the second half of the 20th century as it was realised that the photon provides a clean probe for Nuclear Physics. Its interactions with the target can be treated perturbatively, with the fine structure constant  $\alpha_{\text{EM}}$  as a small parameter.<sup>1</sup> The leading term in the scattering of radiation from a nucleus of mass  $M_X$  and atomic number  $Z$  in the long-wavelength limit was first calculated by Rayleigh’s student, J. J. Thomson:

$$\frac{d\sigma}{d\Omega} = \frac{Z^4 \alpha_{\text{EM}}^2}{M_X^2} \frac{1 + \cos^2 \theta}{2} , \quad (1.1)$$

where  $\theta$  is the scattering angle. Thirring, and independently Sachs and Austern, showed that Eq. (1.1) is not renormalised non-relativistically [5, 6]. It is also recovered as part of a low-energy theorem for a spin- $\frac{1}{2}$  target due to Low, Gell-Mann, and Goldberger [7, 8] which invokes only analyticity and gauge, Lorentz, parity and time-reversal invariance, and was generalised to arbitrary spin by Friar [9]. The theorem states that the nuclear magnetic moment is the only additional parameter needed to determine the leading spin dependence of the cross section.

## 1.1 The importance of dipole electric and magnetic polarisabilities

For a composite system, the first spin-independent piece of the Compton amplitude beyond the Thomson limit is parameterised by two structure constants: the electric and magnetic (scalar dipole) polarisabilities. Polarizabilities arise because the electric and magnetic fields of a real monochromatic photon with frequency  $\omega$  displace the charged constituents of the system and thus induce charge and current multipoles, even if the target is overall charge neutral. The dominant contributions are typically an induced electric dipole moment  $\vec{d}_{\text{ind}}$ , often generated by separating positive and negative charges along the dipole component of the electric field  $\vec{E}$ , and a magnetic dipole moment  $\vec{m}_{\text{ind}}$ , often generated from currents induced by the dipole component of the magnetic field  $\vec{B}$ . In addition, aligning microscopic permanent electric and magnetic dipoles in the external fields can generate mesoscopic induced electric and magnetic dipoles. The linear response in frequency space demonstrates that the induced dipoles are proportional to the incident electric and magnetic fields, i.e.,

$$\vec{d}_{\text{ind}}(\omega) = 4\pi\alpha_{E1}(\omega) \vec{E}(\omega) , \quad \vec{m}_{\text{ind}}(\omega) = 4\pi\beta_{M1}(\omega) \vec{B}(\omega) . \quad (1.2)$$

Neglecting recoil corrections, these induced dipoles then re-radiate at the same frequency  $\omega$  and with the angular dependence characteristic of  $E1$  and  $M1$  radiation, respectively. The proportionality constants in Eq. (1.2) are the *electric dipole polarisability*  $\alpha_{E1}(\omega)$  and the *magnetic dipole polarisability*  $\beta_{M1}(\omega)$ . They characterise the strength of the dipole radiation relative to the intensity of the incoming fields

---

<sup>1</sup>We use the Heaviside-Lorentz system of electromagnetic units and  $\hbar = c = 1$ , so  $e = -\sqrt{4\pi\alpha_{\text{EM}}}$ . The factor  $4\pi$  in Eq. (1.2) is absent in the Gaussian system, but present for SI units; cf. [10].

and vanish for objects with no internal structure. Since they lead to different angular dependences, they can be disentangled in the differential Compton scattering cross section at fixed frequency  $\omega$ .

Polarisabilities encode the temporal response of the target to a real photon of energy  $\omega$  and thus provide detailed information on the masses, charges, interactions, etc. of its active internal degrees of freedom. As an example, in the long-wavelength approximation, the Lorentz-Drude model assumes that the electric field of the photon displaces point-like, charged constituents  $q_n$  of mass  $m_n$ , bound in classical harmonic oscillators with resonance energies  $E_n$  and damping factors  $\Gamma_n$ :

$$\alpha_{E1}(\omega) = \sum_n \frac{q_n^2}{4\pi m_n} \frac{1}{E_n^2 - \omega^2 - i\Gamma_n \omega} . \quad (1.3)$$

One can estimate  $\alpha_{E1}(\omega)$  in the nucleon semiclassically by representing the constituents of its charged pion cloud as objects which are harmonically bound to the nucleon core with an eigenfrequency such that the pion cloud has the same root-mean-square radius as the nucleon, namely about 0.7 fm. Eq. (1.3) then leads to a value of  $\alpha_{E1}(0) \approx 10 \times 10^{-4} \text{ fm}^3$ . This model is unrealistic, of course, but the estimate is surprisingly close to the experimental value. Throughout this review, we therefore quote values for  $\alpha_{E1}(\omega)$  and  $\beta_{M1}(\omega)$  in the ‘‘canonical’’ units of  $10^{-4} \text{ fm}^3$ , and for the dipole spin polarisabilities discussed below, in units of  $10^{-4} \text{ fm}^4$ .

We also take the term ‘‘polarisabilities’’ to be the ‘‘Compton polarisabilities’’, defined in parallel to the above intuitive description by a multipole expansion of the Compton amplitudes, as elaborated in Section 2.2. In nonrelativistic Quantum Mechanics, they can be related to the spectrum of nucleon excited states  $|n\rangle$  with energies  $E_n$ , e.g.:

$$\alpha_{E1}(\omega) = 2 \sum_n \frac{\langle N|D_z|n\rangle \langle n|D_z|N\rangle}{E_n - \omega} + \dots , \quad (1.4)$$

where  $D_z$  is the electric dipole operator. (In Eq. (1.4) we have not explicitly written subtle but important corrections beyond non-relativistic second-order perturbation theory, which were emphasised by L’vov [11], and Bawin and Coon [12], and summarised by Schumacher [10].) Therefore,  $\alpha_{E1}(\omega)$  and  $\beta_{M1}(\omega)$  are strongly influenced by the lowest state with the quantum numbers of an electric or magnetic dipole excitation of the nucleon. For  $\alpha_{E1}$ , this is indeed the  $\pi N$  state. The  $M1$  excitation of the  $\Delta(1232)$  would appear to provide a sizable paramagnetic contribution to  $\beta_{M1}$  of order 10, but since the experimentally measured value is about an order of magnitude smaller, a diamagnetic contribution of similar magnitude but opposite sign exists whose precise nature is not yet determined.

Such excitations also set the energies at which the polarisabilities are manifest in the single-nucleon cross section:  $\omega \gtrsim 50 \text{ MeV}$ . In addition, Eq. (1.4) implies that the dynamical polarisabilities become complex once the first inelastic channel opens at the  $\pi N$  threshold. Finally, polarisabilities are in general related to the dielectric function  $\varepsilon(\omega)$  and magnetic permeability function  $\mu(\omega)$  of a macroscopic system. Since these, in turn, characterise optical properties, nucleon polarisabilities are related to the index of refraction and absorption coefficient of a bulk system of nucleons at a given frequency.

Though polarisabilities are naturally defined as functions of the photon energy  $\omega$ , historically much of the emphasis in the context of the proton and neutron has been on the *static polarisabilities*  $\alpha_{E1} \equiv \alpha_{E1}(\omega = 0)$  and  $\beta_{M1} \equiv \beta_{M1}(\omega = 0)$ , which are often simply termed ‘‘the polarisabilities’’. For clarity, we therefore refer to the functions as *energy-dependent* or *dynamical* polarisabilities [13, 14]<sup>2</sup>. The static polarisabilities are formally and uniquely defined via the Compton scattering amplitudes, as detailed in Section 2.1. Along with the anomalous magnetic moment, they parameterise the deviation of the proton

---

<sup>2</sup>For completeness, we note that the *generalised* polarisabilities of virtual Compton scattering are explored by an incoming photon of non-zero virtuality and can provide complementary information about the spatial charge and current distribution, see e.g. [15] for a review.

Compton cross section from that of a point-like particle in a low-energy expansion which is valid up to photon energies of roughly 80 MeV. Static polarisabilities can be conceptualised, again up to subtle corrections [10–12], as the proportionality constants between induced dipoles and external fields which would be “measured” were the nucleon placed into a parallel-plate capacitor or a pure N-S magnet. They also enter in other processes with sensitivity to nucleon structure; in particular, the relation of  $\beta_{M1}$  to doubly-virtual forward Compton scattering has attracted recent interest in connection with the two-photon-exchange contribution to the Lamb shift in muonic hydrogen [16] (see also Ref. [17] and references therein), and with the nucleon electromagnetic mass shift, see most recently [18].

The Effective Field Theory (EFT) methods which are discussed in this review predict both static and dynamical polarisabilities. They can be used to extract the values of static polarisabilities from experimental data taken at energies too high for the low-energy expansion to be valid. We present a new EFT extraction of polarisabilities from world data in Sections 4 and 5.

## 1.2 Compton scattering from nucleons: data, structure and analysis tools

Therefore, in this review, we examine real Compton scattering from the simplest stable strongly-interacting systems, namely protons and light nuclei, in order to obtain information on the photon-nucleon scattering amplitude. Compton scattering from larger nuclei is reviewed in Ref. [19]. In Section 2.2, we provide the detailed relation of  $\alpha_{E1}(\omega)$ ,  $\beta_{M1}(\omega)$  and the spin polarisabilities to the single-nucleon Compton amplitude. The spin polarisabilities have received much recent attention in both theoretical and experimental studies, since they are a low-energy manifestation of the spin structure of the nucleon, parameterising its spin-dependent response to external electric and magnetic fields.

How are polarisabilities explored? Until the last decades of the 20th century, all experiments investigating Compton scattering from nucleons and nuclei employed bremsstrahlung beams. This created difficulties in accurately measuring the small (nb/sr) cross sections at energies where the polarisabilities are particularly relevant. The advent of photon tagging in the 1980s facilitated a clean separation of elastic and inelastic processes, enabling measurements of the proton cross section with good energy resolution at  $\omega \lesssim 200$  MeV. At the turn of the Millennium, this led to a wealth of data for the proton from Illinois [20], Saskatoon [21, 22] and MAMI [23, 24], and for the deuteron from Illinois [25], Saskatoon [26] and Lund [27]. Since most of these experiments were reviewed by Schumacher [10], we only summarise the data in Section 3, with particular attention to statistical and systematic errors.

In parallel with these developments,  $\alpha_{E1}$  and  $\beta_{M1}$  were calculated in various theoretical models of nucleon structure [28–38]. Comparing these predictions with Compton-scattering data indicates how accurately these models describe electromagnetic excitations of the nucleon. Quark models which do not incorporate explicit pionic degrees of freedom tend to underpredict  $\alpha_{E1}$  and overpredict  $\beta_{M1}$ ; see e.g. Ref. [33]. Computations of  $\alpha_{E1}$  and  $\beta_{M1}$  in chiral quark models incorporate both long-distance ( $\pi$ N) and short-distance (other excitations) physics [30, 39, 40]. Direct determinations of nucleon polarisabilities from lattice simulations of the QCD path integral now appear imminent [41], with results reported in quenched [42–44], partially quenched [45, 46, 49, 50] and even full QCD [47, 48].

New plans for Compton-scattering experiments on protons and light nuclei at MAMI, the HI $\gamma$ S facility at TUNL and MAX-Lab in Lund make this an opportune time to re-examine our knowledge of nucleon Compton scattering at energies up to a few hundred MeV. We therefore delineate in this review what is known about the Compton amplitudes of the proton and neutron. Equation (1.4) implies that the polarisabilities are dominated by the lowest nucleonic states, namely by  $\pi$ N and  $\Delta(1232)$  dynamics, while sensitivity to higher excitations is suppressed. This means that Compton scattering at low energies,  $\omega \lesssim 300$  MeV, is dominated by long-distance properties of the nucleon. In particular, we note that the particles detected in the experiments are photons, nucleons and pions, not quarks themselves. Analysing Compton scattering at these energies in terms of quark degrees of freedom, such as in lattice QCD or models of nucleon structure, is thus not really profitable. Instead, such calculations



can be tested against the constraints extracted from data using a theoretical approach that includes the pertinent low-energy dynamics, provided that it is sufficiently general to encompass the data without undue prejudice. Effective Field Theory (EFT) fits these requirements.

### 1.3 *The role of Effective Field Theory*

The basic principle of an EFT is that many phenomena can be economically—i.e. effectively—described in terms of entities which are not elementary. The fact that the details of nucleon structure are not probed at low energies suggests that a low-energy EFT which includes nucleons, pions and photons should be a useful tool to extract information on nucleon polarisabilities.

In general, for an EFT approach to be successful, a *separation of scales* must exist between the energies involved and those required to excite the particular degrees of freedom of the system which are not treated dynamically. A famous example of an EFT is the Fermi theory of weak interactions, in which  $\beta$  decay is described by a contact interaction between the neutron and its decay products  $e^-$ ,  $\bar{\nu}_e$  and  $p$ . At energy scales of the order of a few MeV, the threshold for production of W and Z bosons is far off, and they can be “integrated out” to leave a simple energy-independent four-fermion interaction together with a series of further interactions, each of which is suppressed by powers of the small quantity  $p_{\text{typ}}/M_W$ , where  $p_{\text{typ}}$  is the typical momentum of a decay product. Similarly, at low enough energies—energies below those where pion degrees of freedom become relevant—a theory of heavy, point-like nucleons should suffice to describe the interactions of nucleons with one another and with photons. This theory has come to be known as the “Pionless Effective Field Theory” (EFT( $\not{\pi}$ )) of Nuclear Physics, and for NN scattering, it is equivalent to Bethe’s low-energy Effective Range Expansion [51–59]. As in all EFTs, “point-like” and “pionless” does not imply the absence of effects such as a non-zero anomalous magnetic moment which are due to nucleon structure, pions and heavier particles. Instead, they are taken into account through Lagrangian parameters—so-called low-energy constants (LECs)—but are not explained within the EFT itself.

The guiding principle in constructing an EFT Lagrangian is that *all* terms compatible with the symmetries of the underlying theory must be included, each proportional to an a priori unknown LEC. This infinite string of terms and couplings is organised according to the power of  $p_{\text{typ}}/\Lambda$  that each operator contributes to amplitudes, with  $p_{\text{typ}}$  the typical momentum of the process, and the breakdown scale  $\Lambda$  set by the mass of the lightest omitted degree of freedom ( $m_\pi$ , for example, in the case of EFT( $\not{\pi}$ )). Since all terms are included, the counterterms needed to renormalise the divergent loops at a given order in  $p_{\text{typ}}/\Lambda$  are automatically present. Unless the theory has a low-energy bound state, the renormalised loop contributions are suppressed, typically by  $p_{\text{typ}}^2/\Lambda^2$  for each loop. Therefore, only a finite number of terms in the Lagrangian need to be considered when working to a particular order in the small, dimensionless parameter  $p_{\text{typ}}/\Lambda$ . While the theory is thus not renormalisable in the conventional sense, only a finite and usually small number of terms are needed for renormalisability to a given order in  $p_{\text{typ}}/\Lambda$ . In addition, a rigorous assessment of residual theoretical uncertainties can be made for any process by estimating the accuracy of its momentum expansion.

Though the number of possible terms (and hence the number of LECs) in the Lagrangian grows rapidly with the order, any given process usually involves only a few of them. Once determined by one piece of data, an LEC enters in the prediction of other observables. Some LECs are related to familiar properties of the particles involved, like charge, mass, anomalous magnetic moment, decay constant, etc., but others are less easy to fix and interpret. Some LECs which govern pion interactions are now being computed by direct lattice simulations of QCD [60–62]. But even when LECs can be derived from the underlying theory, calculations of more complex processes are often more tractable in the EFT framework, as we shall see here for Compton scattering from protons and light nuclei.

Compton scattering in EFT( $\not{\pi}$ ) is discussed in Section 5.4.1. For the proton, it is of limited use, as it amounts to an expansion of the amplitude in powers of  $\omega/m_\pi \ll 1$ . Since only a small fraction

of the data is in the regime where this expansion is valid, the resulting errors on the polarisabilities are inevitably large. In the two-nucleon sector, though, the situation is different. The low-energy NN scattering amplitude is given as an expansion in powers of momenta, with the LECs determined by the scattering length, effective range, etc. Nuclear binding effects and photon-nuclear interactions are then fixed and the leading deuteron Compton amplitudes are predicted with no free parameters, as demonstrated in 1935 in a calculation by Bethe and Peierls [4].

The EFT( $\not{\pi}$ ) expansion breaks down for typical momenta of order  $m_\pi$ , and above this point, the pion itself must be included. While an EFT including the pion must exist because the next excitation, the  $\Delta(1232)$ , is far enough away to provide a separation of scales, there is no guarantee that it is viable. The size of the pion-nucleon coupling constant,  $g_{\pi NN} \approx 13$ , suggests that multi-loop diagrams including dynamical pions may not be suppressed. However, two crucial aspects make the theory manageable. First, the fact that the pion is much lighter than other hadrons is now understood as a consequence of the spontaneously broken (hidden) chiral symmetry of QCD. The up and down quarks are nearly massless on the scale of typical QCD energies. If they were actually massless, the Lagrangian would be invariant under independent isospin rotations of the left- and right-handed quarks,  $SU(2)_L \times SU(2)_R$ . However, only the vector (isospin) subgroup,  $SU(2)_V$ , is manifest in the hadron spectrum and the full symmetry is hidden in the physical QCD vacuum. The pions are then identified as the three Nambu-Goldstone bosons corresponding to the three axial rotations which are symmetry operations on the QCD Lagrangian, but not on the QCD vacuum. The small non-zero quark masses lead to pion masses which are again much smaller than typical QCD scales,  $m_\pi \ll \Lambda_\chi$ . The fact that the pion is a (pseudo-)Nambu-Goldstone boson leads to the second key point: in the “chiral” or zero-quark-mass limit, soft pions decouple so that their interactions with one another and with other hadrons vanish linearly with their momentum.

This provides a perturbative expansion of amplitudes in powers of  $P/\Lambda_\chi \equiv (p_{\text{typ}}, m_\pi)/\Lambda_\chi \ll 1$ , with the light EFT scales being the pion momenta and mass, and  $\Lambda_\chi$  being the scale associated with hadrons which are not explicitly included in the EFT,  $\Lambda_\chi \approx m_\rho$ . This EFT is known as “chiral EFT” ( $\chi$ EFT). The version without explicit  $\Delta(1232)$  degrees of freedom is often referred to as “Baryon Chiral Perturbation Theory” ( $B\chi$ PT), and the purely pionic one as Chiral Perturbation Theory ( $\chi$ PT). Details pertaining to Compton scattering are discussed in Section 4.2, including the special role of the  $\Delta$ . There we also show that photons are included in  $\chi$ EFT partly by invoking minimal substitution and partly by including the field strength tensor  $F_{\mu\nu}$  as a building block in the Lagrangian. Since the latter generates photon couplings which are not constrained by gauge invariance, new LECs enter, including ones which can (at successively higher orders) be related to the anomalous magnetic moment and the charge radius of the nucleon, and to non-chiral contributions to polarisabilities.

The resulting EFT framework provides predictions for the low-energy interaction of pions, photons and nucleons through calculations consistent with the known pattern of QCD symmetries and their breaking. Furthermore, because it is a quantum field theory,  $\chi$ EFT incorporates the requisite consequences of unitarity and Lorentz invariance at low energies. It is this framework which we use to analyse proton Compton scattering in Sections 4.2 and 4.4. In Sections 4.1, 4.3 and 4.5, we also compare  $\chi$ EFT to other approaches for analysing low-energy Compton scattering, most notably dispersion relations (DRs). (Full details of DRs are given in the review of Drechsel et al. [15].) The main differences between  $\chi$ EFT and DRs lie in the careful incorporation of chiral constraints in the former, its stringent agnosticism regarding high-energy details, and the fact that the presence of a small parameter allows an a priori estimate of residual theoretical uncertainties.

## 1.4 *The elusive neutron: Compton scattering from light nuclei*

Experiments on the proton reveal only half of the information in Compton scattering on the nucleon. The 14.7 minute lifetime of the neutron, coupled with the relative weakness of its electromagnetic

interactions, means that the neutron Compton amplitude must be inferred indirectly. While some results exist for scattering neutrons directly in the Coulomb field of heavy nuclei, more accurate data are available for Compton scattering in few-nucleon systems, where nuclear effects can be precisely calculated and taken into account in the analysis. However, it is clearly advantageous to use the same theoretical framework for both the nuclear and photon-nucleon dynamics. The  $\chi$ EFT low-momentum expansion again provides a controlled, model-independent framework for subtracting the nuclear binding effects and analysing the available elastic deuteron scattering data. Both the number and quality of these data, reviewed in Section 3.4, are appreciably inferior to the proton case, since the experiments are markedly harder. The substantial progress made to determine the neutron polarisabilities via this route is reviewed in Section 5. The key to extracting neutron polarisabilities from few-nucleon targets is that the coherent nature of deuteron Compton scattering allows us to observe the photon-neutron amplitude through its interference with the proton and meson-exchange amplitudes, while the Thomson limit imposes a stringent constraint on the few-nucleon amplitude that can be used to check these non-trivial calculations.

$\chi$ EFT work on the deuteron originates from Weinberg’s seminal papers [63], where the nucleon-nucleon potential is computed up to a fixed order in the momentum expansion and then iterated using the Schrödinger equation to obtain the scattering amplitude. The resulting wave functions are combined with operators for Compton scattering derived in  $\chi$ EFT. The photon-nucleon operators are given by the  $\chi$ EFT photon-nucleon amplitudes described above. However,  $\chi$ EFT also expands the nuclear current operators in powers of  $P$ . This has the crucial advantage that the chiral dynamics which drives low-energy Compton scattering is treated consistently in both the single- and few-nucleon operators, so that  $\chi$ EFT results for deuteron Compton scattering can be assessed for order-by-order convergence, too. Meanwhile, Compton scattering from the deuteron in quasi-free kinematics for the neutron was measured in Refs. [64–68], and values for  $\alpha_{E1}^{(n)}$  were extracted. These experiments are discussed in Section 3.5, but  $\chi$ EFT has not yet been extended to  $\gamma d \rightarrow \gamma np$ . Model calculations of elastic and inelastic scattering on the deuteron are briefly reviewed in Section 5.5.  $\chi$ EFT is also used to produce the first calculations, in any framework, of elastic scattering on  ${}^3\text{He}$  [69–71]; see Section 5.6. Since  ${}^3\text{He}$  is doubly charged, its cross section is larger by a factor of up to 4 compared to the proton or deuteron. In addition, polarised  ${}^3\text{He}$  is interesting since it serves as an effective polarised neutron target.

## 1.5 Results and the future

In Sections 4.4 and 5.3, we apply the  $\chi$ EFT methodology to the proton and deuteron databases, respectively, and present new central values and uncertainties for the proton and neutron dipole polarisabilities, as well as a detailed comparison of the  $\chi$ EFT predictions with data. Here we preview our best values of the proton and isoscalar (i.e. average nucleon) scalar dipole polarisabilities in a two-parameter fit:

$$\begin{aligned} \alpha_{E1}^{(p)} &= 10.5 \pm 0.5(\text{stat}) \pm 0.8(\text{theory}) \quad , \quad \beta_{M1}^{(p)} = 2.7 \pm 0.5(\text{stat}) \pm 0.8(\text{theory}) \\ \alpha_{E1}^{(s)} &= 10.5 \pm 2.0(\text{stat}) \pm 0.8(\text{theory}) \quad , \quad \beta_{M1}^{(s)} = 3.6 \pm 1.0(\text{stat}) \pm 0.8(\text{theory}) \quad . \end{aligned} \tag{1.5}$$

In a one-parameter fit employing the Baldin sum rules for the proton and isoscalar nucleon:

$$\begin{aligned} \alpha_{E1}^{(p)} &= 10.7 \pm 0.3(\text{stat}) \pm 0.2(\text{Baldin}) \pm 0.8(\text{theory}) \\ \beta_{M1}^{(p)} &= 3.1 \mp 0.3(\text{stat}) \pm 0.2(\text{Baldin}) \pm 0.8(\text{theory}) \\ \alpha_{E1}^{(s)} &= 10.9 \pm 0.9(\text{stat}) \pm 0.2(\text{Baldin}) \pm 0.8(\text{theory}) \\ \beta_{M1}^{(s)} &= 3.6 \mp 0.9(\text{stat}) \pm 0.2(\text{Baldin}) \pm 0.8(\text{theory}) \quad . \end{aligned} \tag{1.6}$$

In Section 6, we close this review with a discussion of future experiments which hold the promise of improving the Compton database and the determination of polarisabilities. We also describe upcoming



experimental efforts to extract the still relatively unexplored spin polarisabilities. Finally, we outline the anticipated  $\chi$ EFT developments that will help refine the analysis of these forthcoming data.

## 2 Foundations

### 2.1 Overview

We begin by parameterising the  $T$ -matrix for Compton scattering of a photon of incoming energy  $\omega$  from a nucleon with spin  $\vec{\sigma}/2$  by six independent invariant amplitudes [72], which read in the operator basis first appearing in Ref. [73] and usually employed in  $\chi$ EFT:

$$\begin{aligned}
 T(\omega, z) = & A_1(\omega, z) (\vec{\epsilon}'^* \cdot \vec{\epsilon}) + A_2(\omega, z) (\vec{\epsilon}'^* \cdot \hat{k}) (\vec{\epsilon} \cdot \hat{k}') \\
 & + i A_3(\omega, z) \vec{\sigma} \cdot (\vec{\epsilon}'^* \times \vec{\epsilon}) + i A_4(\omega, z) \vec{\sigma} \cdot (\hat{k}' \times \hat{k}) (\vec{\epsilon}'^* \cdot \vec{\epsilon}) \\
 & + i A_5(\omega, z) \vec{\sigma} \cdot \left[ (\vec{\epsilon}'^* \times \hat{k}) (\vec{\epsilon} \cdot \hat{k}') - (\vec{\epsilon} \times \hat{k}') (\vec{\epsilon}'^* \cdot \hat{k}) \right] \\
 & + i A_6(\omega, z) \vec{\sigma} \cdot \left[ (\vec{\epsilon}'^* \times \hat{k}') (\vec{\epsilon} \cdot \hat{k}) - (\vec{\epsilon} \times \hat{k}) (\vec{\epsilon}'^* \cdot \hat{k}') \right] ,
 \end{aligned} \tag{2.1}$$

where  $\hat{k}$  ( $\hat{k}'$ ) is the unit vector in the momentum direction of the incoming (outgoing) photon with polarisation  $\vec{\epsilon}$  ( $\vec{\epsilon}'^*$ ),  $\theta$  is the scattering angle, and  $z = \cos \theta$ . This form holds in the Breit and centre-of-mass (cm) frames. The first two amplitudes are spin-independent, while the other four parameterise interactions with the nucleon spin. The amplitude is related to the differential cross section by

$$\left. \frac{d\sigma}{d\Omega} \right|_{\text{frame}} = \Phi_{\text{frame}}^2 |T|^2 , \tag{2.2}$$

where  $\Phi_{\text{frame}}$  is a frame-dependent flux factor which tends to  $1/(4\pi)$  at low energies; see also Section 2.3.

For forward scattering,  $\vec{k} = \vec{k}'$ , and only the structures of  $A_1$  and  $A_3$  survive. The behaviour of these amplitudes as  $\omega \rightarrow 0$  is determined by low-energy theorems (LETs) which rely only on analyticity and gauge, Lorentz, parity and time-reversal invariance [7, 8]

$$\lim_{\omega \rightarrow 0} T(\omega, 1) = -\frac{e^2 Q^2}{M_N} \vec{\epsilon}'^* \cdot \vec{\epsilon} - i \frac{e^2 \kappa^2 \omega}{2M_N} \vec{\sigma} \cdot (\vec{\epsilon}'^* \times \vec{\epsilon}) + \mathcal{O}(\omega^2) , \tag{2.3}$$

where  $-eQ$  is the nucleon charge,  $\kappa$  is the anomalous magnetic moment (in nuclear magnetons) and  $M_N$  is the mass of the target. At  $\omega = 0$ , we recover the spin- and energy-independent Thomson term, and hence the corresponding cross section of Eq. (1.1).

Eq. (2.3) may also be obtained in the limit  $\omega \rightarrow 0$  from the pole diagrams in a calculation of Compton scattering using photons coupled to a Dirac nucleon via its charge and anomalous magnetic moment (with the spinors normalised to  $\bar{u}u = 1$ ), as shown in diagram (a) of Fig. 2.1.

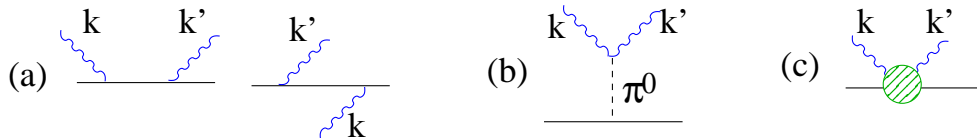


Figure 2.1: (a) Nucleon Born graphs for Dirac nucleons; (b) pion Born graph; (c) structure contribution.

As explained in the Introduction, our primary interest is to obtain information on the structure of the two-photon response of the nucleon, which requires going beyond the single-photon processes of the

Born terms. It is therefore useful to separate the amplitudes into “non-structure” and “structure” parts

$$A_i(\omega, z) = A_i^{\text{Born}}(\omega, z) + \bar{A}_i(\omega, z) . \quad (2.4)$$

Identifying the former with the pole (Born) contribution mentioned above, while not a unique choice, ensures that the LETs are satisfied by these terms alone. It also agrees with usage in dispersion relation (DR) calculations (see Section 4.1). There is another known contribution to spin-dependent scattering which comes from the  $t$ -channel exchange of a neutral pion, as shown in Fig. 2.1(b), which first contributes at  $\mathcal{O}(\omega^3)$ ; we choose to include this term in the Born or “non-structure” part as well, but the choice is not universal. The other term,  $\bar{A}_i$ , represented by Fig. 2.1(c), parameterises deviations from the “known” part of the amplitude and describes the nucleon as a polarisable object.

Expanding both nucleon Born and structure amplitudes in the Breit frame to order  $\omega^3$ , we have

$$\begin{aligned} A_1(\omega, z) &= -\frac{Q^2 e^2}{M_N} + \frac{e^2 \omega^2}{4M_N^3} \left( (Q + \kappa)^2 (1 + z) - Q^2 \right) (1 - z) + 4\pi\omega^2 (\alpha_{E1} + z\beta_{M1}) + \mathcal{O}(\omega^4) \\ A_2(\omega, z) &= \frac{e^2 \omega^2}{4M_N^3} \kappa (2Q + \kappa) z - 4\pi\omega^2 \beta_{M1} + \mathcal{O}(\omega^4) \\ A_3(\omega, z) &= \frac{e^2 \omega}{2M_N^2} \left( Q(Q + 2\kappa) - (Q + \kappa)^2 z \right) + A_3^{\pi^0} + 4\pi\omega^3 (\gamma_1 - (\gamma_2 + 2\gamma_4)z) + \mathcal{O}(\omega^5) \\ A_4(\omega, z) &= -\frac{e^2 \omega}{2M_N^2} (Q + \kappa)^2 + 4\pi\omega^3 \gamma_2 + \mathcal{O}(\omega^5) \\ A_5(\omega, z) &= \frac{e^2 \omega}{2M_N^2} (Q + \kappa)^2 + A_5^{\pi^0} + 4\pi\omega^3 \gamma_4 + \mathcal{O}(\omega^5) \\ A_6(\omega, z) &= -\frac{e^2 \omega}{2M_N^2} Q(Q + \kappa) + A_6^{\pi^0} + 4\pi\omega^3 \gamma_3 + \mathcal{O}(\omega^5) , \end{aligned} \quad (2.5)$$

where the  $\pi^0$  pole amplitudes are, with  $t = 2\omega^2(z - 1)$  and  $\tau_3$  the third Pauli matrix in isospin space:

$$A_3^{\pi^0} = \tau_3 \frac{e^2 g_{\pi NN} \omega^3 (z - 1)}{4\pi^2 f_\pi M_N (m_{\pi^0}^2 - t)} , \quad A_6^{\pi^0} = -A_5^{\pi^0} = \tau_3 \frac{e^2 g_{\pi NN} \omega^3}{8\pi^2 f_\pi M_N (m_{\pi^0}^2 - t)} . \quad (2.6)$$

To this order, the only difference in the cm frame is that  $A_2$  has an additional Born term  $e^2 Q^2 \omega / M_N$ . The omitted terms start one order lower in the cm frame (e.g.  $\mathcal{O}(\omega^3)$  in  $A_1$ ), because the amplitude does not have manifest crossing symmetry, whereas in the Breit frame it does. The “structure” parts of the amplitude are represented at this order by  $\alpha_{E1}$  and  $\beta_{M1}$ , namely the static spin-independent polarisabilities discussed above, and by the analogous spin polarisabilities  $\gamma_i$  [74]; see Section 2.2. The canonical units are  $10^{-4} \text{ fm}^3$  for the former and  $10^{-4} \text{ fm}^4$  for the latter. We denote proton and neutron polarisabilities by a superscript (e.g.  $\alpha_{E1}^{(p)}$ ) and define isoscalar and isovector polarisabilities as averages and differences, such that  $\alpha_{E1}^{(s)} = \frac{1}{2}(\alpha_{E1}^{(p)} + \alpha_{E1}^{(n)})$  and  $\alpha_{E1}^{(v)} = \alpha_{E1}^{(p)} - \alpha_{E1}^{(n)}$ .

For forward scattering, only  $\alpha_{E1} + \beta_{M1}$  and  $\gamma_0 = \gamma_1 - \gamma_2 - 2\gamma_4$  augment the LETs of Eq. (2.3), while the  $\pi^0$  pole terms do not contribute. Since forward scattering amplitudes can be related to inelastic cross sections via the optical theorem, two sum rules can be constructed for these quantities:

$$\alpha_{E1} + \beta_{M1} = \frac{1}{2\pi^2} \int_{\omega_\pi}^{\infty} d\omega' \frac{\sigma_T(\omega')}{\omega'^2} , \quad \gamma_0 = \frac{1}{4\pi^2} \int_{\omega_\pi}^{\infty} d\omega' \frac{\sigma_{1/2}(\omega') - \sigma_{3/2}(\omega')}{\omega'^3} , \quad (2.7)$$

where  $\sigma_T$  is the total cross section for an unpolarised target and  $\sigma_{1/2}$  ( $\sigma_{3/2}$ ) is the cross section for a photon-nucleon system of total helicity 1/2 (3/2). The integrals are over lab energies, starting at the

pion photoproduction threshold. The first of these is known as the Baldin Sum Rule [75, 76]. We adopt the evaluation of Olmos de León et al. [24] for the proton and that of Levchuk and L'vov [77] for the neutron:

$$\alpha_{E1}^{(p)} + \beta_{M1}^{(p)} = 13.8 \pm 0.4 \quad , \quad \alpha_{E1}^{(n)} + \beta_{M1}^{(n)} = 15.2 \pm 0.4 \quad , \quad (2.8)$$

which combine to give the isoscalar sum-rule value, with errors added in quadrature:

$$\alpha_{E1}^{(s)} + \beta_{M1}^{(s)} = 14.5 \pm 0.3 \quad . \quad (2.9)$$

Using information on pion photoproduction multipoles, together with a parameterisation of data at intermediate energies and a Regge form at higher energies, Babusci et al. [78] obtained  $\alpha_{E1}^{(p)} + \beta_{M1}^{(p)} = 13.69 \pm 0.14$ . However, using different parameterisations for  $\sigma_T$ , Levchuk and L'vov [77] obtained a central value of 14.0. The evaluation quoted above is more recent and more conservative [24]. Given the uncertainties associated with extracting neutron multipoles from deuterium data, perhaps it is not surprising that evaluations for the neutron are more variable. We regard the direct use of deuterium photodisintegration data above pion threshold as ill-advised (c.f. Ref. [78]). The value we quote uses neutron photoproduction multipoles obtained from proton ones via isospin considerations in a more reliable approach, although significant model dependence is still present [77].

Only the combinations  $\alpha_{E1} - \beta_{M1}$  and  $\gamma_\pi = \gamma_1 + \gamma_2 + 2\gamma_4$  enter for backward scattering. Because we have separated out the pion-pole contribution, our values for  $\gamma_\pi^{(p)}$  differ from those obtained when it is included. The difference is  $-e^2 g_{\pi NN} / (8\pi^3 f_\pi M_N m_{\pi^0}^2) = -46.4$ , using the proton value  $g_{\pi NN}^2 / 4\pi = 13.64$  [79].

Various low-energy cross sections have been constructed in the literature. All of these can be found by using various approximations to Eq. (2.5) in Eqs. (2.1) and (2.2). The simplest is the Klein-Nishina formula of a point-like Dirac particle, with  $\kappa = 0$  [80]. If  $\kappa \neq 0$  is included but the target is still structureless and terms of order  $\omega^3$  are discarded, one obtains the Powell cross section [81]. The Petrun'kin cross section additionally allows the inclusion of terms of order  $\omega^2$  arising from the interference of the leading structure contributions  $\alpha_{E1}$  and  $\beta_{M1}$  with the Thomson term in  $|A_1|^2$  and hence is complete at  $\mathcal{O}(\omega^2)$  [82, 83]. None of these includes spin polarisabilities, the  $\pi^0$  pole, or the energy dependence of the polarisabilities. We shall say more about their impact in the next section.

## 2.2 *Polarisabilities from a multipole expansion*

Many multipoles are induced inside an object that interacts with an electromagnetic field of frequency  $\omega$ . Each oscillates with that same frequency and thus emits radiation with a characteristic angular distribution. The proportionality constant between each photon field and the corresponding induced multipole moment is called a polarisability; each is an energy-dependent function which parameterises the stiffness of the internal degrees of freedom with particular quantum numbers against deformations of a given electric or magnetic multipolarity and energy. In this section, we generalise the picture presented in the Introduction to consider polarisabilities beyond the scalar dipole ones.

Hildebrandt et al. [13, 14] used the formalism of an energy-dependent multipole analysis established by Ritus [84–86] and summarised in Ref. [87] to define energy-dependent polarisabilities. Here we proceed differently, constructing the first few multipoles via the most general field-theoretical Lagrangian which describes the interactions between a nucleon field  $N$  with spin  $\vec{\sigma}/2$  and two photons of fixed, non-zero energy  $\omega$  and definite multiplicities. This includes the structure effects, i.e. the local coupling of the two photons to the nucleon. Taking into account gauge and Lorentz invariance, as well as invariance under parity and time-reversal, the interactions with the lowest photon multiplicities are

$$\begin{aligned} \mathcal{L}_{\text{pol}} = & 2\pi N^\dagger [\alpha_{E1}(\omega) \vec{E}^2 + \beta_{M1}(\omega) \vec{B}^2 + \gamma_{E1E1}(\omega) \vec{\sigma} \cdot (\vec{E} \times \dot{\vec{E}}) \\ & + \gamma_{M1M1}(\omega) \vec{\sigma} \cdot (\vec{B} \times \dot{\vec{B}}) - 2\gamma_{M1E2}(\omega) \sigma_i B_j E_{ij} + 2\gamma_{E1M2}(\omega) \sigma_i E_j B_{ij} + \dots] N \quad , \end{aligned} \quad (2.10)$$

with  $T_{ij} \equiv \frac{1}{2}(\partial_i T_j + \partial_j T_i)$ ,  $\vec{T} = \vec{E}, \vec{B}$ . These terms are straightforward extensions to the effective Lagrangian of zero-energy scattering in Refs. [88, 89]. The photons couple electrically or magnetically ( $X, Y = E, M$ ) and undergo transitions  $Xl \rightarrow Yl'$  of definite multiplicities  $l$  and  $l' = l \pm \{0, 1\}$ . The interactions are unique up to field redefinitions using the equations of motion. Dipole couplings are proportional to the electric and magnetic field directly, or to their time derivatives. Quadrupole interactions couple to the irreducible second-rank tensors  $E_{ij}$  and  $B_{ij}$ . Eq. (2.10) lists all contributions with coupling to at least one dipole field. Polarisabilities of higher multipolarity, e.g. the electric and magnetic quadrupole polarisabilities [88, 89], are denoted by ellipses. Thus far, such terms are not relevant for Compton scattering below 300 MeV [14, 90–93].

The two-photon response of the nucleon in the dipole approximation is therefore characterised by the six linearly independent, energy-dependent polarisabilities of Eq. (2.10). The spin-independent terms are parameterised by the two scalar functions already encountered in Section 1.1: the electric dipole polarisability  $\alpha_{E1}(\omega)$ , and the magnetic dipole polarisability  $\beta_{M1}(\omega)$ . The four spin polarisabilities parameterise the response of the nucleon spin to an external field. The two corresponding to dipole-dipole transitions,  $\gamma_{E1E1}(\omega)$  and  $\gamma_{M1M1}(\omega)$ , are analogous to the classical Faraday effect related to birefringence inside the nucleon [94]. They describe how an incoming photon causes a dipole deformation in the nucleon spin, which in turn leads to dipole radiation. The two mixed spin polarisabilities,  $\gamma_{E1M2}(\omega)$  and  $\gamma_{M1E2}(\omega)$ , encode scattering where the angular momenta of the incident and outgoing photons differ by one unit. In principle, the polarisabilities can be defined in any coordinate system in which the initial and final photon energies are identical. In practice, the centre-of-mass frame is usually used.<sup>3</sup>

We can now translate the interactions (2.10) into contributions to the structure amplitudes  $\bar{A}_i(\omega, z)$ :

$$\begin{aligned}
\bar{A}_1(\omega, z) &= 4\pi [\alpha_{E1}(\omega) + z \beta_{M1}(\omega)] \omega^2 + \dots \\
\bar{A}_2(\omega, z) &= -4\pi \beta_{M1}(\omega) \omega^2 + \dots \\
\bar{A}_3(\omega, z) &= -4\pi [\gamma_{E1E1}(\omega) + z \gamma_{M1M1}(\omega) + \gamma_{E1M2}(\omega) + z \gamma_{M1E2}(\omega)] \omega^3 + \dots \\
\bar{A}_4(\omega, z) &= 4\pi [-\gamma_{M1M1}(\omega) + \gamma_{M1E2}(\omega)] \omega^3 + \dots \\
\bar{A}_5(\omega, z) &= 4\pi \gamma_{M1M1}(\omega) \omega^3 + \dots \\
\bar{A}_6(\omega, z) &= 4\pi \gamma_{E1M2}(\omega) \omega^3 + \dots \quad ,
\end{aligned} \tag{2.11}$$

where the dots refer to omitted higher multipoles. The relations between the static polarisabilities of the multipole expansion and those of Ragusa [74] defined in Eq. (2.5) are

$$\begin{aligned}
\gamma_1 &= -\gamma_{E1E1} - \gamma_{E1M2} \quad , \quad \gamma_2 = \gamma_{M1E2} - \gamma_{M1M1} \quad , \quad \gamma_3 = \gamma_{E1M2} \quad , \quad \gamma_4 = \gamma_{M1M1} \\
\gamma_0 &= -\gamma_{M1E2} - \gamma_{M1M1} - \gamma_{E1E1} - \gamma_{E1M2} \quad , \quad \gamma_\pi = \gamma_{M1E2} + \gamma_{M1M1} - \gamma_{E1E1} - \gamma_{E1M2} \quad .
\end{aligned} \tag{2.12}$$

The first of the photon multiplicities in the subscripts of the spin polarisabilities is sometimes dropped in the literature (so  $\gamma_{M2} \equiv \gamma_{E1M2}$  etc).

We reiterate that polarisabilities are identified by a multipole analysis *at fixed energy*, i.e. only by the angular and spin dependence of the amplitudes. Eq. (2.11) emphasises that the complete set of energy-dependent polarisabilities does not contain more or less information than the untruncated Compton amplitudes  $\bar{A}_i(\omega, z)$ . However, the information is more accessible, since any hadronic mechanism and interaction leaves a characteristic signature in a particular multipole polarisability, as discussed in the Introduction. Thus, when the multipole expansion is truncated after the dipole terms, determining the six energy-dependent dipole polarisabilities is reduced, in principle, to an energy-dependent multipole

---

<sup>3</sup>The dynamical polarisabilities introduced here via Eq. (2.10) differ from those given in Refs. [13, 14] by a factor of  $\sqrt{s}/M_N$ . The polarisabilities are linear combinations of the multipole moments  $f_{XY}^{l\pm}$  of the Compton amplitudes; the details, including the relevant projection formulae, are given in Ref. [14].

analysis of the Compton scattering database. Such proof-of-principle results were reported in [92, 95, 96] but suffer at present from rather large error bars.

At very low energies, the functions encoding the dynamical polarisabilities can be approximated by their zero-energy values and therefore some experiments (most recently Ref. [20]) have used the Petrun'kin formula to extract the static polarisabilities  $\alpha_{E1}^{(p)}$  and  $\beta_{M1}^{(p)}$  directly from their data. Indeed, the low-energy expansion of the cross section could conceivably be extended to higher powers in  $\omega^2$ . At fourth order, not only do the spin polarisabilities enter, but also the next terms (slope parameters) in the expansion of  $\alpha_{E1}(\omega)$  and  $\beta_{M1}(\omega)$ :

$$\lim_{\omega \rightarrow 0} \alpha_{E1}(\omega) = \alpha_{E1} + \omega^2 \alpha_{E\nu} + \mathcal{O}(\omega^4) \quad , \quad \lim_{\omega \rightarrow 0} \beta_{M1}(\omega) = \beta_{M1} + \omega^2 \beta_{M\nu} + \mathcal{O}(\omega^4) \quad . \quad (2.13)$$

Static values of the next multipoles, the scalar quadrupole polarisabilities, also enter at  $\mathcal{O}(\omega^4)$ . (Contributions to  $T$  at  $\omega^4$  and  $\omega^5$  were discussed by Babusci et al. [88] and Holstein et al. [89].) However, the convergence is governed by the pion-production threshold (the first non-analyticity) and the expansion is thus in powers of  $\omega/m_\pi$ . With the slope correction to the scalar polarisabilities of size  $(\omega/m_\pi)^2$ , this leads to a correction of about 10% for photon energies as low as 50 MeV. The expansion is therefore useless where most high-accuracy data are taken.

Consequently, modern extractions of the static polarisabilities choose a different route. It is assumed that the energy dependence of the polarisabilities, and hence that of the amplitudes  $\bar{A}_i$ , is adequately captured in some framework (e.g. dispersion relations,  $\chi$ EFT). With the long-range part of the interactions thus fixed, one fits up to six low-energy constants which encode the short-distance dynamics and thereby determines the static polarisabilities from data. This is the approach taken in this review.

### 2.3 Kinematics

Consider Compton scattering on a nucleus  $X$  with mass  $M_X$ ,  $\gamma(\omega, \vec{k}) X(E, \vec{p}) \rightarrow \gamma(\omega', \vec{k}') X(E', \vec{p}')$ , with  $E$  and  $\vec{p}$  ( $E'$  and  $\vec{p}'$ ) the kinetic energy and momentum of the target before (after) the reaction. So far,  $\omega$  denoted a generic photon momentum and  $\theta$  a generic scattering angle. We now add subscripts to differentiate between the centre-of-mass (cm), laboratory (lab) and Breit frames, using relativistic kinematics throughout. The coordinate axes are specified as follows: the incident photon beam direction defines the  $z$ -axis, and the  $xz$ -plane is the scattering plane, with the  $y$ -axis perpendicular to it.

In the centre-of-mass (cm) frame, the total energy is the square-root of the Mandelstam variable  $s$ ,

$$\sqrt{s} = \omega_{\text{cm}} + \sqrt{M_X^2 + \omega_{\text{cm}}^2} \quad . \quad (2.14)$$

On the other hand, experiments are performed in the lab frame, where the incident and outgoing photon energy are related to one another by a recoil correction, and to  $\omega_{\text{cm}}$ , as follows:

$$\omega_{\text{lab}} = \omega_{\text{cm}} \frac{\sqrt{s}}{M_X} \quad , \quad \omega'_{\text{lab}} = \frac{M_X \omega_{\text{lab}}}{M_X + \omega_{\text{lab}}(1 - \cos \theta_{\text{lab}})} \quad . \quad (2.15)$$

The scattering angle transforms as

$$\cos \theta_{\text{cm}} = \frac{\cos \theta_{\text{lab}} - \beta}{1 - \beta \cos \theta_{\text{lab}}} \quad , \quad (2.16)$$

where  $\beta = \omega_{\text{lab}}/(\omega_{\text{lab}} + M_X)$  is the relative velocity between the cm and lab frames. The frame-dependent flux (phase-space) factor for cross sections (see Eq. (2.2)) is

$$\Phi_{\text{cm}} = \frac{M_X}{4\pi\sqrt{s}} \quad , \quad \Phi_{\text{lab}} = \frac{\omega'_{\text{lab}}}{4\pi\omega_{\text{lab}}} \quad . \quad (2.17)$$



It is also useful to introduce the Mandelstam variables  $t$  and  $\nu = (s - u)/(4M_X)$ :

$$t = 2\omega_{\text{lab}}\omega'_{\text{lab}}(\cos\theta_{\text{lab}} - 1) = 2\omega_{\text{cm}}^2(\cos\theta_{\text{cm}} - 1) = 2\omega_{\text{Breit}}^2(\cos\theta_{\text{Breit}} - 1) \quad , \quad \nu = \frac{1}{2}(\omega_{\text{lab}} + \omega'_{\text{lab}}) \quad , \quad (2.18)$$

where we have also listed variables in the Breit frame, with

$$\omega_{\text{Breit}} = \frac{2M_X\nu}{\sqrt{4M_X^2 - t}} \quad , \quad \cos\theta_{\text{Breit}} = 1 - \frac{\omega_{\text{cm}}^2}{\omega_{\text{Breit}}^2}(1 - \cos\theta_{\text{cm}}) \quad . \quad (2.19)$$

For  $\omega/M_X \rightarrow 0$ , i.e. small photon energy or large target mass, the three coordinate frames coincide. The Breit and lab frames coincide for  $\theta = 0^\circ$ , and the Breit and cm frames for  $\theta = 180^\circ$ .

In the Breit or “brick-wall” frame, the photon transfers no energy and the target recoils with the magnitude of its momentum unchanged but its direction exactly reversed,  $\vec{p}'_{\text{Breit}} = -\vec{p}_{\text{Breit}}$ . This has the advantage that the Compton amplitude is manifestly crossing-symmetric, i.e. invariant under the interchange of initial and final states:  $\omega_{\text{Breit}} \leftrightarrow -\omega_{\text{Breit}}$ ,  $\vec{k}_{\text{Breit}} \leftrightarrow -\vec{k}'_{\text{Breit}}$ ,  $\vec{\epsilon} \leftrightarrow \vec{\epsilon}'^*$ . By inspection of Eq. (2.1), the spin-independent amplitudes  $A_{1,2}$  are even in  $\omega_{\text{Breit}}$ , and the spin-dependent ones,  $A_{3-6}$ , are odd.

## 2.4 Observables

We can now relate the six independent amplitudes of Eq. (2.1) to scattering observables. A complete classification of unpolarised, single- and double-polarisation observables for a spin- $\frac{1}{2}$  target (nucleon or  $^3\text{He}$ ) by Babusci et al. [88] demonstrated that experiments in which up to two polarisations are fixed can be described by four independent observables below the first threshold and four more observables above it. Here, we list some of the combinations which either have been or will soon be explored experimentally or theoretically: unpolarised, linearly or circularly polarised beams and unpolarised or polarised targets, without the detection of final-state polarisations. We define them as they are measured, and—with the exception of the differential cross section—refer to the literature for formulae which relate them to the Compton amplitudes  $A_i$ . Observables with a vector-polarised nucleus can be understood by replacing the spin-polarised nucleon by the polarised nucleus. These will be discussed in Section 6.1.

In order to take into account nuclear binding for the deuteron and  $^3\text{He}$ , it is convenient to use a helicity basis for these targets:

$$A(M_f, \lambda_f; M_i, \lambda_i) = \langle M_f, \lambda_f | T | M_i, \lambda_i \rangle \quad , \quad (2.20)$$

where  $\lambda_{i/f} = \pm$  is the circular polarisation of the initial/final photon, and  $M_{i/f}$  is the magnetic quantum number of the initial/final target spin, i.e.  $M_{i/f} \in \{0; \pm 1\}$  for the deuteron and  $M_{i/f} \in \{\pm \frac{1}{2}\}$  for  $^3\text{He}$ . A target of spin  $S_X$  has  $[2(\text{photon helicities}) \times (2S_X + 1)(\text{target spins})]^2$  (in and out state) amplitudes, but parity and time reversal leave only  $2(S_X + 1)(2S_X + 1)$  independent components: 4 spin-0 helicity amplitudes become 2 independent ones,  $A_{1,2}$ ; 16 helicity amplitudes for spin- $\frac{1}{2}$  reduce to the 6 of Eq. (2.1); and 36 amplitudes for spin-1 yield 12 independent structures, constructed e.g. by Chen et al. [97].

**Unpolarised beam and target:** In this case, the only observable is the differential cross section. For the nucleon, it is obtained from Eq. (2.2) after averaging over the initial target spins and photon polarisations and summing over the final states; one finds in the basis of Eq. (2.1) (see e.g. Refs. [98, Chapter IV.2] and [92, Chapter 4.1]):

$$\begin{aligned} |T|^2 = & \frac{1}{2} |A_1|^2 (1 + z^2) + \frac{1}{2} |A_3|^2 (3 - z^2) + (1 - z^2) \left[ 4 \text{Re}[A_3^* A_6] + \text{Re}[A_3^* A_4 + 2A_3^* A_5 - A_1^* A_2] z \right] \\ & + (1 - z^2) \left[ \frac{1}{2} |A_2|^2 (1 - z^2) + \frac{1}{2} |A_4|^2 (1 + z^2) \right. \\ & \left. + |A_5|^2 (1 + 2z^2) + 3 |A_6|^2 + 2 \text{Re}[A_6^* (A_4 + 3A_5)] z + 2 \text{Re}[A_4^* A_5] z^2 \right] \quad . \end{aligned} \quad (2.21)$$

In the helicity basis, the unpolarised differential cross section is built with the flux factors of Eq. (2.17) by summing over all combinations of incident and outgoing quantum numbers  $(M_f, \lambda_f; M_i, \lambda_i)$  and including a symmetry factor from averaging over the initial target and photon polarisations:

$$\left. \frac{d\sigma}{d\Omega}(\omega, \theta) \right|_{\text{frame}} = \frac{1}{2(2S_X + 1)} \Phi_{\text{frame}, X}^2 \sum_{M_f, M_i; \lambda_f, \lambda_i} |A(M_f, \lambda_f; M_i, \lambda_i)|^2 \quad . \quad (2.22)$$

**Polarised beam, unpolarised target:** The cross section with a circularly polarised photon beam of arbitrary helicity is half of the unpolarised one and thus provides no additional information. With a linearly polarised beam, two observables can be constructed, see Fig. 2.2, with corresponding experiments approved at HI $\gamma$ S [99, 100]. The cross section for an incoming photon is denoted by  $\left[ \frac{d\sigma}{d\Omega} \right]_{x(y)}^{\text{lin}}$



Figure 2.2: (Colour online) Observables for linearly polarised photon incident on unpolarised target.

for an incoming photon polarised parallel (perpendicular) to the scattering plane. Their sum gives the unpolarised cross section, and the difference,

$$\Sigma_3(\omega, \theta) = \left( \left[ \frac{d\sigma}{d\Omega} \right]_x^{\text{lin}} - \left[ \frac{d\sigma}{d\Omega} \right]_y^{\text{lin}} \right) / \frac{d\sigma}{d\Omega} \quad , \quad (2.23)$$

is the beam asymmetry<sup>4</sup>. Its relation to the deuteron helicity basis is given in Refs. [71, 93, 101].

For the forward and backward spin polarisabilities,  $\gamma_0$  and  $\gamma_\pi$ , we already saw that the multipole expansion is a convenient tool to identify configurations in which a specific polarisability is isolated or suppressed. Such configurations were found for the proton by Maximon [102]. The interaction in Eq. (2.10) parameterised by  $\alpha_{E1}(\omega)$  vanishes when the polarisations of the incoming and outgoing photons are orthogonal, e.g. when a photon which is linearly polarised in the scattering plane scatters at  $90^\circ$  as in  $\left[ \frac{d\sigma}{d\Omega} \right]_x^{\text{lin}}(\theta_{\text{Breit}} = 90^\circ)$ , see Fig. 2.3. In that case, since the incoming magnetic field is orthogonal

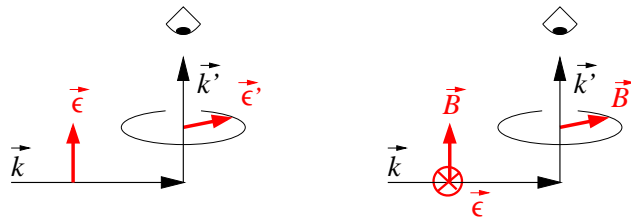


Figure 2.3: (Colour online) Left: Configuration for which an induced electric dipole cannot radiate an  $E1$  photon to an observer (“eye”) at  $\theta_{\text{Breit}} = 90^\circ$ ; right: same for radiating an  $M1$  photon.

to the scattering plane, the induced magnetic dipole radiates most strongly at  $90^\circ$ , providing maximal sensitivity to  $\beta_{M1}(\omega)$ . Similarly,  $\left[ \frac{d\sigma}{d\Omega} \right]_y^{\text{lin}}(\theta_{\text{Breit}} = 90^\circ)$  is independent of  $\beta_{M1}(\omega)$  but maximally sensitive to  $\alpha_{E1}(\omega)$ . When the nucleon is embedded in a nucleus, the relative motion of the  $\gamma N$  system may complicate this analysis.

<sup>4</sup>The subscript is omitted in Ref. [101]; the symbol used in Ref. [93] is  $\Pi^{\text{lin}}$ .

**Polarised beam, polarised target:** Figure 2.4 depicts double-polarisation observables with circularly polarised photons, as an example of observables that will be explored in the future; see Section 6.2. The target can be polarised in the scattering plane along  $\hat{x}$  or along the beam direction,  $\hat{z}$ . Cross-section

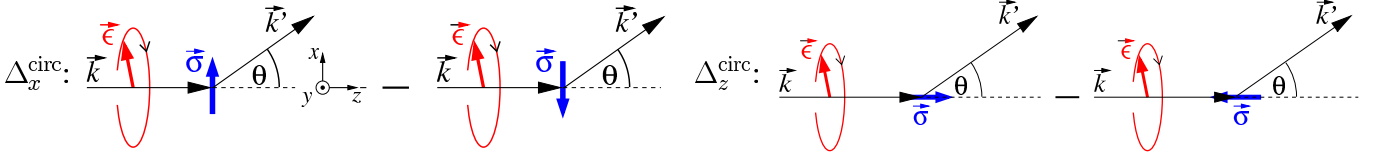


Figure 2.4: (Colour online) Observables for circularly polarised photon incident on polarised target.

differences can be defined by flipping the target polarisation:

$$\Delta_x^{\text{circ}}(\omega, \theta) = \left( \frac{d\sigma}{d\Omega} \right)_{\uparrow\rightarrow} - \left( \frac{d\sigma}{d\Omega} \right)_{\uparrow\leftarrow}, \quad \Delta_z^{\text{circ}}(\omega, \theta) = \left( \frac{d\sigma}{d\Omega} \right)_{\uparrow\uparrow} - \left( \frac{d\sigma}{d\Omega} \right)_{\uparrow\downarrow}. \quad (2.24)$$

The first arrow of the subscript denotes a positive beam helicity, the second the target polarisation.  $\Delta_x^{\text{circ}}$  compares a target polarised along  $+\hat{x}$  vs.  $-\hat{x}$ , i.e. perpendicular to the beam direction but in the scattering plane. Similarly,  $\Delta_z^{\text{circ}}$  is the difference with the target polarised parallel vs. anti-parallel to the beam helicity<sup>5</sup>. Both observables change sign for left-circularly polarised photons (negative beam helicity).

Polarisation asymmetries are defined as the ratio of the cross-section differences  $\Delta$  to their sums<sup>6</sup>:

$$\Sigma_x^{\text{circ}} = \frac{\left( \frac{d\sigma}{d\Omega} \right)_{\uparrow\rightarrow} - \left( \frac{d\sigma}{d\Omega} \right)_{\uparrow\leftarrow}}{\left( \frac{d\sigma}{d\Omega} \right)_{\uparrow\rightarrow} + \left( \frac{d\sigma}{d\Omega} \right)_{\uparrow\leftarrow}}, \quad \Sigma_z^{\text{circ}} = \frac{\left( \frac{d\sigma}{d\Omega} \right)_{\uparrow\uparrow} - \left( \frac{d\sigma}{d\Omega} \right)_{\uparrow\downarrow}}{\left( \frac{d\sigma}{d\Omega} \right)_{\uparrow\uparrow} + \left( \frac{d\sigma}{d\Omega} \right)_{\uparrow\downarrow}}. \quad (2.25)$$

Except for  $\Sigma_{x,z}^{\text{circ}}$  for a spin- $\frac{1}{2}$  target, the denominators are not the unpolarised cross sections [71, 92, 101]. Normalising to sums of cross sections removes many experimental systematic uncertainties and the frame dependence associated with the flux factors  $\Phi_{\text{frame}}$ . However, a small spin-averaged cross section in the denominator may enhance theoretical uncertainties or hide unfeasibly small count rates: cross-section differences  $\Delta$  set the scale for the beamtime necessary to perform these experiments. The asymmetries  $\Sigma_{x,z}^{\text{circ}}$  vanish in the static limit only for a proton target, but are nonzero for the neutron.

The relations of the double-polarisation observables (with arbitrary angle  $\phi$  between polarisation and scattering planes) to the amplitudes  $A_i$  are compiled in Ref. [92, Chapter 4.1] for complex amplitudes. For real amplitudes, i.e. below threshold, the relations for  $\Delta_{x,z}^{\text{circ}}$  and  $\Sigma_{x,z}^{\text{circ}}$  were first reported in Ref. [98, Chapter IV.2]. Those for the helicity amplitudes are compiled for the deuteron in [93, 101] and for  $^3\text{He}$  in [70, 71]. Similarly, double-polarisation observables with linearly polarised photons can also be defined— see e.g. [88, 92, 93] for definitions and figures analogous to the ones above.

### 3 Experimental overview

In this section, we review the experimental efforts on Compton scattering using proton and deuteron targets, spanning the past half-century. For the proton, we have divided the discussion into low-energy measurements (below pion threshold) and high-energy measurements (above pion threshold). There is a relatively clear distinction between experiments in these two energy regions, although some cases do overlap with both regions. There are also some polarised measurements on the proton in the modern era.

<sup>5</sup>In Ref. [97],  $\Delta_z^{\text{circ}}$  is denoted by  $2\Delta_{1\sigma}$ .

<sup>6</sup> $\Sigma_{x,z}^{\text{circ}}$  is denoted by  $\Sigma_{2x,2z}$  in Ref. [88] and  $\Sigma_{x,z}$  in Refs. [97, 101].

For the deuteron, there are again two categories—elastic Compton-scattering experiments and quasi-free measurements in which deuteron breakup is exploited to study the neutron explicitly in quasi-free kinematics (with the proton acting as a spectator).

Special emphasis will be placed on enumerating the statistical and systematic uncertainties of the proton and deuteron experiments, since these issues figure prominently in the fitting of the various data sets using the  $\chi$ EFT formalism. Somewhat cursory details are given about the experiments: many are discussed at greater length in the review by Schumacher [10].

### 3.1 *Low-energy proton Compton scattering*

The earliest low-energy Compton-scattering experiments on the proton (up to about  $\omega_{\text{lab}} \sim 100$  MeV) were reported in the mid-to-late 1950s by Pugh et al. [103], Oxley [104], Hyman et al. [105], Bernardini et al. [106] and Goldansky et al. [107]. These early experiments were not aimed at measuring the electromagnetic polarisabilities of the proton, as we think of them today. In fact, these experiments were more motivated by their ability to test recently developed dispersion-theory calculations of Gell-Mann and Goldberger and others. Nevertheless, it is noteworthy that in some of these early papers (most notably Goldansky et al. [107]), attempts were made to extract the proton polarisability.

These early experiments were pioneering efforts, given the difficulty of working with continuous bremsstrahlung photon beams and detector systems with very poor energy resolution. Large NaI photon detectors with good energy resolution were not yet available, and photon-tagging facilities were still decades in the future. Normalising the photon flux to obtain an absolute cross section is notoriously difficult with bremsstrahlung beams, not to mention that the incident continuous bremsstrahlung beam itself has no well-defined energy resolution. For example, the experiment of Oxley [104] had a central photon energy of 60 MeV, with a full width of 55 MeV—so it is remarkable that this experiment produced results for the cross section between 10.6 and 14.7 nb/sr from  $70^\circ$  to  $150^\circ$ , which is generally consistent with modern results.

Directed efforts were made in the experiment of Goldansky et al. [107] in 1960 to determine the proton polarisability. The same group continued these efforts many years later in the mid-1970s in the experiment of Baranov et al. [108, 109]. While uncertainties in the extracted polarisabilities were reduced by a factor of two in the later experiment, the experimental techniques during that period were still relatively crude compared to today. For this reason, it is reasonable to consider the data prior to 1980 to be exploratory in nature, and to not give very much credence to the absolute scale of the cross sections from those experiments.

Almost 20 years passed before the next proton Compton-scattering experiment was attempted. Two major developments in experimental techniques emerged in that period to make the new generation of Compton measurements considerably more reliable than their predecessors. First, the method of photon tagging was introduced, providing both a mono-energetic beam of photons and a means of normalising the photon flux by direct counting of the post-bremsstrahlung electrons. This revolutionised many photonuclear experiments. Second, new large-volume high-resolution NaI detectors (25.4 cm diameter  $\times$  25.4 cm long, and even larger) were available with a resolution  $\Delta E/E \sim 3\%$  for photons of 50–100 MeV. These two improvements in the beam and the detectors changed the game significantly, paving the way for a new era of Compton-scattering experiments designed specifically to pin down the proton polarisability.

The major experiments that have contributed in the modern era to the determination of the proton polarisability are those of Federspiel et al. [20], Zieger et al. [23], Hallin et al. [21], MacGibbon et al. [22], and Olmos de León et al. [24] covering the 10-year period between 1991 and 2001. All but two of them used tagged-photon beams of energy  $\omega_{\text{lab}} \leq 165$  MeV—the exceptions are Hallin, who used a continuous bremsstrahlung beam with energies up to 289 MeV, and Zieger, who used a bremsstrahlung beam with a proton-recoil detection technique. It is worth examining all of these low-energy experiments in more

detail to elucidate their relative merits and potential weaknesses.

The first of the modern experiments was conducted by Federspiel et al. [20] at the tagged-photon facility at Illinois. Tagged photons in the energy range  $\omega_{\text{lab}} = 32\text{--}72$  MeV impinged on a liquid hydrogen target; scattered photons were detected at fixed lab angles of  $60^\circ$  and  $135^\circ$  by two large  $25.4\text{ cm} \times 25.4\text{ cm}$  NaI detectors. This experimental configuration can be considered a “standard” tagged-photon experiment, in the sense that the well-characterised beam and the single-arm detector conditions are conceptually extremely simple. The data were divided into 8 bins over this energy range, each 4 MeV wide. The resulting cross sections had statistical uncertainties that were roughly  $\pm 10\%$ . Systematic uncertainties due to photon flux ( $\pm 1\%$ ), target thickness ( $\pm 1\%$ ), detector acceptance ( $\pm 1.4\%$ ) and simulation uncertainties ( $\pm 1\%$ ) were correlated among all data points and contributed in quadrature to give a total systematic error of  $\pm 2.2\%$  for this experiment. The data were predominantly limited by statistical accuracy, due to the low counting statistics in each tagger energy bin, as well as error propagation due to subtraction of random coincidences and empty-target background in the data analysis.

A follow-up experiment was performed by MacGibbon et al. [22] (including the Illinois group) at the tagged-photon facility at the Saskatchewan Accelerator Laboratory (SAL). This experiment was essentially identical to the lower-energy version at Illinois and used the same large NaI detectors, which had been transported to Saskatoon for this purpose. The tagged-photon energy range was  $\omega_{\text{lab}} = 70\text{--}100$  MeV, so it overlapped with the previous measurement, and the detector lab angles were  $90^\circ$  and  $135^\circ$ . One clever twist to this experiment, however, was the ability to extend the usable energy range into the untagged region ( $\omega_{\text{lab}} = 100\text{--}148$  MeV). The normalisation of the untagged data could be linked directly to the well-known normalisation of the data in the tagged region using the bremsstrahlung spectrum shape, so a reliable extrapolation of the cross section up to the endpoint energy of 148 MeV could be achieved. The tagged data were divided into 4 energy bins, each 8 MeV wide, and the untagged data were divided into 5 bins, each 10 MeV wide. Here again, the statistical accuracy of the data was the limiting factor—the lowest statistical uncertainty was about  $\pm 10\%$  and some points had errors close to  $\pm 20\%$ . Systematic uncertainties came from similar sources as the previous experiment, but were slightly larger. Correlated errors such as photon flux ( $\pm 1\text{--}2\%$ ), target thickness ( $\pm 1.2\%$ ) and detector acceptance ( $\pm 1.2\%$ ), as well as additional rate-dependent corrections ( $\pm 1\text{--}3\%$ ), added up to an overall systematic error of  $\pm 2.9\%$  for the untagged data and a range of  $\pm 3\text{--}4\%$  for the tagged data. Only a small part of that overall error ( $\pm 0.4\%$  for the tagged data and  $\pm 1.0\text{--}1.4\%$  for the untagged data) was uncorrelated among the data points. In the overlap region near 70 MeV for the  $135^\circ$  data, the MacGibbon results are in excellent agreement with those of Federspiel et al. [20].

The experiment of Hallin et al. [21] was also performed at SAL and included participants from the two experiments discussed above. The Hallin experiment had three major differences: (1) the photon beam was a continuous bremsstrahlung beam, (2) the beam energies were mostly above pion threshold (endpoint energies of  $\omega_{\text{lab}} = 170\text{--}298$  MeV), and (3) a single, large-volume NaI detector from Boston University was used (the BUNI detector, 50 cm diameter  $\times$  56 cm long). Since only a single photon detector was used, data for each lab angle in the  $25^\circ$  to  $135^\circ$  range of this experiment had to be measured sequentially (as opposed to simultaneously). As a bremsstrahlung experiment, the statistical uncertainties of the data can be relatively low, depending on how large a region of the bremsstrahlung distribution is utilised to generate the cross section. In this case, different regions were used for the angular distributions (15 MeV wide) as compared to the excitation functions (5 MeV wide)—hence, the statistical errors in the angular distributions tended to be lower, ranging from  $\pm 3.5\text{--}5.0\%$  at backward angles to  $\pm 10\text{--}18\%$  at forward angles. The major sources of (correlated) systematic uncertainties arose from determining the photon flux ( $\pm 3\%$ ) and the target thickness ( $\pm 2\%$ ), giving  $\pm 3.6\%$ . Additional contributions from, for example, detector efficiency ( $\pm 0.3\%$ ) and solid angle ( $\pm 0.3\%$ ), as well as other factors, led to point-to-point systematic errors in the range of  $\pm 1\text{--}2\%$ . Taken together, these systematic errors (correlated + uncorrelated) amounted to about  $\pm 3.7\text{--}4.2\%$  for the total systematic uncertainty in the final cross sections, which is quite good considering the inherent difficulties of normalising a



bremsstrahlung experiment.

One of the more novel experiments was a  $180^\circ$  scattering measurement by Zieger et al. at MAMI [23]. In this case, the forward proton (recoiling at  $0^\circ$ ) was detected in a magnetic spectrometer, yielding the scattered photon cross section in the backward direction ( $180^\circ$ ), where the result is exclusively sensitive to the difference of the electric and magnetic polarisabilities ( $\alpha_{E1}^{(p)} - \beta_{M1}^{(p)}$ ). The incident photon energies were  $\omega_{\text{lab}} = 98$  and  $132$  MeV, and each of the two data points constituted an energy bin of width  $16$  MeV. The forward proton cross sections were determined by comparing the Compton proton and electron yields—this enabled the absolute normalisation to be deduced without detailed knowledge of the shape or intensity of the incident bremsstrahlung spectrum. The statistical uncertainties for the two data points varied widely ( $\pm 18.4\%$  and  $\pm 5.4\%$ ), but the systematic uncertainties due to the subtraction of target backgrounds and the normalisation procedure were more consistent between the two data points ( $\pm 6.4\%$  and  $\pm 4.3\%$ , respectively). This experiment is the only measurement of the  $180^\circ$  (backward) Compton-scattering cross section for the proton.

The most comprehensive experiment to date was the one by Olmos de León et al. [24] at MAMI, covering the tagged-photon energy range  $\omega_{\text{lab}} = 59\text{--}164$  MeV and the lab angular range  $59^\circ\text{--}155^\circ$  simultaneously. This was possible by using the large TAPS array consisting of six separate assemblies of hexagonal  $\text{BaF}_2$  cells. Statistical errors varied from  $\pm 5\%$  at the lowest energies to about  $\pm 10\%$  at the higher energies. Systematic errors from photon flux ( $\pm 2\%$ ) and target thickness ( $\pm 2\%$ ) were added in quadrature to give an overall systematic error of  $\pm 3\%$  for the entire data set. In addition, random systematic uncertainties (point-to-point) due to the geometry of the individual array elements and the detector simulation contributed another  $\pm 5\%$  to each data point separately. These data overlapped with (and extended higher than) the energy regions of the previous data from Federspiel [20] and MacGibbon [22], and all three data sets are in excellent agreement in the overlap region. Regarding the extraction of proton polarisabilities, it is worth mentioning that the Olmos de León data set tends to dominate most global analyses due to the large number of data points and their relatively low statistical errors.

A summary of the low-energy proton experiments, from the 1950s up to the present day, is shown in the upper portion of Table 3.1. Plots of sample cross sections are also shown in Fig. 3.1.

### 3.2 High-energy proton Compton scattering

Compton-scattering experiments on the proton have also been explored above pion threshold, dating back to the 1960s. In the early experiments of DeWire et al. [110], Baranov et al. [111, 112], Gray and Hanson [113] and Genzel et al. [114], the main intent was to investigate the region of the  $\Delta(1232)$  resonance. In the 1990s, the emphasis of these experiments evolved to become more specific—studying the  $E2/M1$  ratio and determining the backward spin polarisability,  $\gamma_\pi^{(p)}$ , of the proton. These experiments had been interpreted in a dispersion-relation framework, but the recent evolution of EFT has made these experiments (below about  $400$  MeV) accessible to this theoretical treatment.

Most of the experiments have been conducted at MAMI or LEGS—in the main, they have been competing efforts and less complementary in nature. There have been some disagreements in the published cross sections, and as a result, there have been diverging interpretations, particularly with regard to  $\gamma_\pi^{(p)}$ . We now review the experiments from each laboratory in turn.

The MAMI experiments covered the energy region of the  $\Delta$  resonance and higher, roughly  $\omega_{\text{lab}} = 200\text{--}500$  MeV, using the photon-tagging facility with a typical tagger-channel energy width of about  $2.0\text{--}2.5$  MeV. For most of the cases, the scattered photon was detected in coincidence with the recoil proton—this kinematic redundancy helps tremendously in the reduction of background due to photons from the decay of neutral pions which are copiously produced above threshold. In some cases below about  $300$  MeV, however, the CATS large-volume NaI detector ( $48$  cm diameter  $\times$   $64$  cm long) was sufficient to cleanly separate the Compton events from the pion-production events due to its excellent

Legend	First Author	$\omega_{\text{lab}}$ (MeV)	$\theta_{\text{lab}}$ (deg)	Ref.	$N_{\text{data}}$	Symbol
Chicago 58	Oxley	25–87	70–150	[104]	4	◆
MIT 59	Hyman	50–140	50, 90	[105]	12	◆
Moscow 60	Goldansky	40–70	45–150	[107]	5	▼
Illinois 60	Bernardini	100–290	90, 129, 139	[106]	17	▲
MIT 67	Pugh	50–130	45, 90, 135	[103]	16	◆
Moscow 74	Baranov	82–111	90, 150	[108, 109]	7	▼
Illinois 91	Federspiel	32–72	60, 135	[20]	16	▲
MAMI 92	Zieger	98, 132	180	[23]	2	◆
SAL 93	Hallin	135–291	25–135	[21]	77	■
SAL 95	MacGibbon	70–148	90, 135	[22]	18	■
MAMI 01	Olmos de León	59–164	59–155	[24]	65	◆
Cornell 61	DeWire	275–425	75, 90, 120	[110]	5	◆
Tokyo 64	Nagashima	310–420	90	[113, 114]	2	■
Moscow 66	Baranov	214,237,249	55–150	[111, 112]	12	▼
Illinois 67	Gray	185–335	90, 135	[113]	5	▲
Bonn 76	Genzel	237–430	50–130	[114]	19	◆
MAMI 96	Peise	200–410	75	[115, 116]	17	◆
MAMI 96a	Molinari	250–500	90	[115, 117]	13	◆
MAMI 99	Wissmann	199–410	131	[120]	11	◆
MAMI 01a	Wolf	250–800	30–150	[118, 119]	294	◆
LEGS 01	Blanpied	213–334	65–135	[123]	77	★
MAMI 02	Camen	210–470	136	[121]	10	◆

Table 3.1: Compton-scattering experiments on the proton. The column for  $N_{\text{data}}$  shows *only* the number of points for each data set up to a cutoff of 400 MeV. The last column indicates the corresponding symbols used in the figures.

intrinsic energy resolution

In the paper by Hüniger et al. [115], two independent experiments at forward angles were reported—this constituted a summary of work already published. In one case, also reported earlier by Peise et al. [116], the CATS detector was located at  $\theta_{\text{lab}} = 60^\circ$  ( $\theta_{\text{cm}} = 75^\circ$ ) and a multi-element array of small NaI detectors was located at the corresponding angle of  $\theta_{\text{lab}} = 47^\circ$  on the other side of the beamline to intercept the forward recoil proton. For additional background suppression, a  $2\pi$  array of BaF<sub>2</sub> crystals was positioned close to the target, directly opposite CATS, serving as a supplemental veto for  $\pi^0$  production events. In the reported cross sections, the statistical uncertainties varied from as large as  $\pm 40\%$  for the very lowest energies, to  $\pm 10\text{--}15\%$  below the  $\Delta$  resonance, and then closer to  $\pm 5\%$  at and above the resonance peak. Systematic errors have been estimated to be  $\pm 4.4\%$  below 350 MeV,  $\pm 6\%$  for 350–380 MeV, and  $\pm 8\%$  above 380 MeV. Within these systematic errors, common sources of uncertainty for all data points arose from the photon flux ( $\pm 2\%$ ) and the target thickness ( $\pm 2\%$ ).

In the other case, also reported earlier by Molinari et al. [117], sets of 12 photon/proton detector

pairs were arranged azimuthally around the target, with all photon detectors at a polar angle of  $\theta_{\text{lab}} = 76^\circ$  ( $\theta_{\text{cm}} = 90^\circ$ ) and the corresponding proton detectors at  $\theta_{\text{lab}} = 44^\circ$  on the opposite side. The photon detectors were Pb-glass blocks and the proton detectors were  $\Delta E/E$  plastic scintillator telescopes. The good energy resolution of the proton arm and the small acceptance of each proton telescope enabled a clean separation of Compton and pion events. Moreover, the Pb-glass blocks are insensitive to neutrons, so the background from charged-pion production was reduced. Statistical uncertainties in the data are  $\pm 4\text{--}10\%$  below 400 MeV,  $\pm 10\text{--}25\%$  up to 450 MeV, and then rather large ( $\pm 50\%$  or more) up to 490 MeV. Systematic errors have been estimated to be  $\pm 4\%$  below 360 MeV and  $\pm 5\%$  above that energy due to background subtraction of  $\pi^0$  events. This included the common uncertainties due to the photon flux ( $\pm 2\%$ ), target thickness ( $\pm 2\%$ ), and detector efficiency ( $\pm 3\%$ ).

A broader survey of energies and angles was presented by Wolf et al. [118], which was also identically reported in Galler et al. [119]. This experiment used a large-acceptance detector array covering lab angles of  $30^\circ\text{--}150^\circ$  and photon energies of  $\omega_{\text{lab}} = 250\text{--}800$  MeV. Much of this data set (the upper half, generally) is beyond the applicable scale of  $\chi\text{EFT}$ . The photon arm of the detector configuration consisted of 10 large Pb-glass segments, each containing 15 individual Pb-glass blocks. The proton arm had two wire chambers and an array of tall plastic scintillator bars used for proton time-of-flight measurements. Below 400 MeV, relatively good separation between Compton and pion events could be achieved. However, above that energy, considerable overlap required a separate subtraction procedure based on comparing in-plane (Compton-scattering plane) and out-of-plane (pion production with a  $2\gamma$  decay) events to isolate the Compton events. This method could add a considerable uncertainty to the extracted cross sections for the data above 400 MeV. The random errors associated with each data point (which varied widely in magnitude across the extensive data set) included both the purely statistical error due to counting statistics as well as individual systematic errors due to detector efficiency, geometrical acceptance and background subtraction. Beyond that, there were overall scaling systematic errors related to photon flux ( $\pm 2\%$ ) and target thickness ( $\pm 2\%$ ) that affected the entire data set as a whole.

A separate experiment by Wissmann et al. [120] focused on a single backward angle ( $\theta_{\text{lab}} = 131^\circ$ ) in the energy range  $\omega_{\text{lab}} = 200\text{--}410$  MeV. The motivation was to compare free proton Compton scattering with quasi-free scattering, as a precursor to a similar quasi-free Compton experiment on the neutron. The experimental setup was simple, consisting of a single photon arm using the large-volume CATS detector, which could achieve good separation between Compton and pion-production events below 300 MeV. Above that point, there is some overlap which can be subtracted using a simulation of the pion events. The resulting data set had statistical uncertainties as large as  $\pm 20\text{--}40\%$  at the lowest energies and improved to  $\pm 8\text{--}13\%$  above about 275 MeV (approaching the  $\Delta$  peak and beyond). Systematic uncertainties due to photon flux, target thickness and detector acceptance were common to all data points and were combined in quadrature to be  $\pm 3\%$  overall.

Finally, in a related experiment, Camen et al. [121] obtained data at a similar backward angle ( $\theta_{\text{lab}} = 136^\circ$ ) at energies of  $\omega_{\text{lab}} = 200\text{--}470$  MeV in an effort to extract  $\gamma_{\pi}^{(p)}$ . This was related to a controversy based on an earlier extraction by LEGS [122, 123] which disagreed with standard dispersion theory and  $\chi\text{PT}$ . As expected, the disagreement can be traced to discrepancies in the measured cross sections at the two laboratories near the  $\Delta(1232)$  peak. The results from LEGS are discussed below. In the MAMI experiment, the CATS detector was used in conjunction with a recoil proton detector array consisting of 30 liquid scintillator cells located at  $\theta_{\text{lab}} = 18^\circ$  on the other side of the beamline. This experiment was similar to that of Wissmann [120], but the redundancy of detecting the coincident recoil proton helped discriminate Compton events from pion-production events without relying on a simulation for the latter. The statistical errors were typically in the range of  $\pm 7\%$  to  $\pm 15\%$  for all data points, but there was no mention in the published report of any information regarding systematic uncertainties. It is likely, however, that they would be similar to the ones stated by Wissmann [120].

Although LEGS covers a more limited energy range than MAMI, it offers the unique capability of delivering polarised photon beams. This is accomplished by backscattering polarised ultraviolet laser

photons from 2.6 GeV electrons in the Brookhaven National Laboratory synchrotron ring. Energies of  $\omega_{\text{lab}} = 210\text{--}333$  MeV can be covered using the photon-tagging facility at LEGS—the photon energy resolution is about 5 MeV, which is twice the width of the MAMI tagger channels. At LEGS (as at MAMI), these higher-energy experiments were performed by detecting the recoil proton in coincidence with the scattered photon, allowing a clean separation of Compton-scattering and pion-production events.

The LEGS polarised experiments were performed in a series of three groups of runs [123–125] covering scattering angles of  $\theta_{\text{cm}} = 65^\circ\text{--}135^\circ$ . Scattered photons were detected in a large-volume NaI detector (48 cm diameter  $\times$  48 cm long); a large array of plastic scintillator bars on the opposite side of the beamline was used to detect the recoil proton in coincidence. The proton arm also had wire chambers located near the target to reconstruct the proton angle more precisely. The kinematic overdetermination for Compton events not only served to isolate them from the larger background due to  $\pi^0$  decay photons, but it also enabled detector efficiencies to be determined directly from the data (instead of relying on simulations). This helped considerably in reducing systematic uncertainties.

The statistical precision of the LEGS cross sections is excellent in the vicinity of the  $\Delta(1232)$  peak, and the systematics also seem to be very much under control. The reported cross sections list the combination (in quadrature) of statistical and point-to-point systematic errors. Even with these combined errors, the uncertainties are only about  $\pm 2\%$  to  $\pm 5\%$  for data points between 275 and 325 MeV. Outside that energy range (the highest energy, 333 MeV, and 213–265 MeV), the error bars are in the  $\pm(5\text{--}10)\%$  range. The overall systematic error in the cross-section scale was evaluated to be  $\pm 2\%$  based on uncertainties in the target thickness, photon flux, and geometric solid angles.

With the exception of a much earlier measurement from Frascati [126] at 318 MeV, these are the first polarisation asymmetry measurements in this energy region for proton Compton scattering. Near the  $\Delta$  peak, the asymmetries are not small (0.1–0.5) and the combined statistical plus point-to-point systematic errors (arising solely from uncertainties in the photon beam polarisation for the two different polarisation states) are typically  $\pm(7\text{--}25)\%$  for most data points. Owing to the nature of the asymmetry measurement, there are no overall systematic errors that do not cancel out completely.

Regarding the cross sections, there are clearly discrepancies between the LEGS and the MAMI data. This is most apparent in Fig. 11 of Ref. [118] at backward angles close to the  $\Delta$  peak. It is this discrepancy which gives rise to a disagreement in the values extracted for the E2/M1 ratio and  $\gamma_\pi^{(p)}$ . At the backward angles, both of these quantities display the greatest sensitivity, especially the spin polarisability. The same discrepancy is shown in Fig. 2 of Ref. [121], which is in agreement with [118]. Data at the highest SAL energy of 286 MeV [21] appear to be intermediate between the two sets. It is worth recalling that both the LEGS experiments [123–125] and the MAMI experiments [118, 121] used coincidence methods to detect the scattered photon and the recoil proton, greatly reducing their susceptibility to backgrounds from pion production. By contrast, the experiment of Ref. [21] used bremsstrahlung (untagged photons) and had a single photon arm using the large-volume BUNI detector. It is difficult to know the source of the discrepancy between the MAMI and LEGS data sets.

A summary of the high-energy proton experiments is shown in the lower portion of Table 3.1. Plots of sample cross sections are also shown in Fig. 3.2.

### 3.3 *A critical look at the proton data*

As a precursor to the EFT fits presented in Section 4.4, we briefly provide a comparison of the various data sets that have been used in the proton fitting. Unless otherwise stated, energies and angles will always refer to the lab frame. We will use “low energy” to mean the region up to 170 MeV (ending just at the upper limit of the Olmos de León data), “intermediate energy” to mean 170–250 MeV (ending where the Wolf data set starts) and “high energy” to mean 250–400 MeV (“high” is to be understood in a low-energy EFT context). We have attempted to judge the consistency of the world data sets by

plotting them as a function of energy for a wide range of angles, as seen in Figs. 3.1 and 3.2. Initially we do not add any theory curves. There is not space here to present all the data in sufficient detail to appreciate all the points that can be made; more plots can be found in the supplemental material available online.

In the low-energy region (see Fig. 3.1), we note that there are no data below  $45^\circ$  and none above  $155^\circ$  (with the exception of the two Zieger  $180^\circ$  points). The only data below 55 MeV are from Federspiel. From 55 MeV to around 120 MeV, multiple data sets contribute; in addition to modern experiments (Federspiel, Olmos de León and MacGibbon), there are also a number of older data sets which look compatible with the modern data. From 120 to 170 MeV, the only data are from MacGibbon, Olmos de León and Hallin (with the exception of some points from Pugh with large error bars). Figure 3.2 shows a selection of data over the whole energy range up to 350 MeV (chosen to highlight kinematics where data exist from more than one experiment). From 170–210 MeV, Hallin is essentially the only data set, with Bernardini contributing three points and two separate MAMI experiments one point each (both with very large error bars). Above 210 MeV, much more data are available, both old and new, but the agreement is very problematic. Above 250 MeV, the Wolf data set dominates statistically.

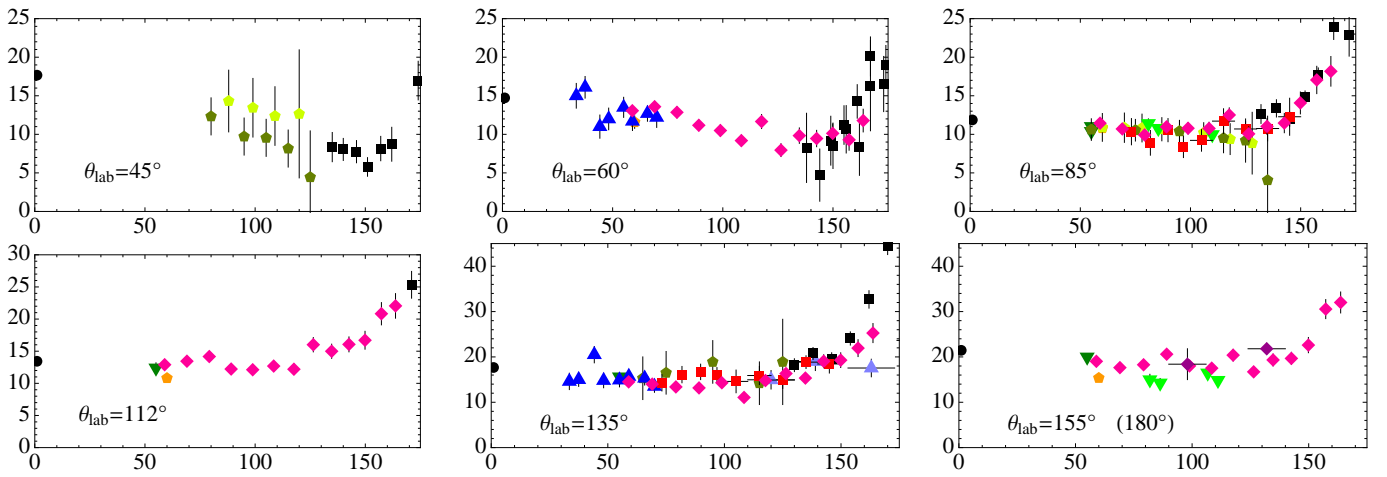


Figure 3.1: (Colour online) Data for Compton scattering on the proton below  $\omega_{\text{lab}} = 175$  MeV. Lab cross sections in nb/sr are plotted in bins of  $10^\circ$  lab angle as a function of lab photon energy in MeV. For greater comparability of data, a phenomenological parameterisation of the angular dependence has been used to shift data points to the nominal bin angle, but the effect is only perceptible for the Oxley and Goldansky points at  $70^\circ$  and  $120^\circ$ . The black dot at  $\omega_{\text{lab}} = 0$  indicates the cross section corresponding to the Thomson limit. See Table 3.1 for the key to the data symbols.

It has been recognised that the extensive data set of Olmos de León has larger fluctuations than are compatible with the quoted statistical errors, and we follow Wissmann [127] in adding a point-to-point systematic error of  $\pm 5\%$  in quadrature with the statistical error when fitting this set (not shown in plots)<sup>7</sup>. The Olmos de León  $133^\circ$  data tend to be low at energies around 100 MeV compared to other data, especially MacGibbon. There is an apparent discrepancy between the Baranov  $150^\circ$  and the Olmos de León  $155^\circ$  data, with the latter lying high.

Three points from the modern low-energy data are clearly outliers: Federspiel ( $135^\circ$ , 44 MeV), Olmos de León ( $133^\circ$ , 108 MeV) and Hallin ( $141^\circ$  (cm), 170 MeV). The Bernardini data set consists of 7 points in the range 120–200 MeV (in wide energy bins), and sufficiently many of these are low compared with the trend of the rest of the data that we do not include this set in our fits. The Oxley

<sup>7</sup>For the other proton data sets, we include all systematic uncertainties in a single floating normalisation for each respective set.



data set is broadly consistent with other sets, but the statistical errors are so tiny as to give it undue weight in any fit. Though we continue to plot all of these, we do not use them in fits.

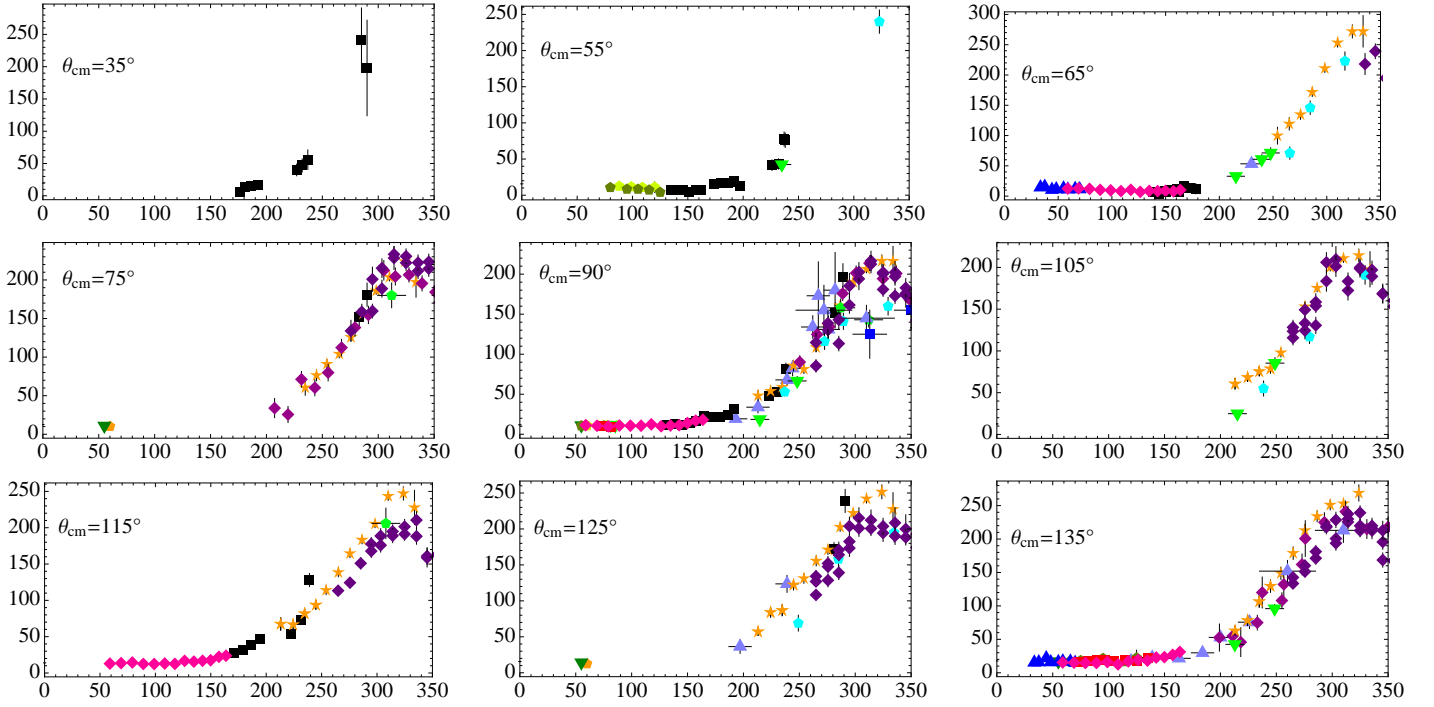


Figure 3.2: (Colour online) Selected data for Compton scattering on the proton below 350 MeV lab energy. Centre-of-mass cross sections in nb/sr are plotted in bins of  $10^\circ$  cm angle as a function of lab photon energy in MeV. See Table 3.1 for the key to the data symbols.

In the intermediate-energy region above about 200 MeV, the problems with consistency of the data are most significant. The lowest-energy Blanpied data are noticeably high compared to any plausible smooth interpolation between the low- and high-energy data; the Hallin data partially reinforce this trend. The older Gray and Baranov data lie much lower in this region, while agreeing well a little higher, and the few MAMI data points in this region are also lower, though with large error bars. That said, the 215 MeV Baranov data points at  $91.9^\circ$  and  $107.2^\circ$  (cm) are too low to be plausible.

In the high-energy region, the data are dominated by the Wolf data, and the other MAMI data look compatible with it (although two of the Wissmann points beyond the peak lie decidedly high). A number of points are available from older experiments and most are in good agreement, though as is well known, the Genzel, Nagashima and Gray data sets all have one or more points which are implausibly low. The major problem, however, is the lack of agreement between the Wolf and Blanpied data for angles above  $100^\circ$ , where the Blanpied data sit substantially above the Wolf data. At the worst point, the  $\Delta(1232)$  peak for  $\theta_{\text{cm}} = 115^\circ$ , the disagreement is almost 25%. But agreement at more forward angles such as  $\theta_{\text{cm}} = 90^\circ$  precludes an explanation in terms of an overall normalisation error. Viewed as a function of angle for constant energy, both data sets show more structure than one might expect, and it is hard to draw a conclusion about which is more internally consistent based on the data alone. The older data sets favour Wolf, while the few Hallin points in this region favour or even exceed Blanpied. This issue will be revisited later when discussing the proton EFT fits in Section 4.4.

### 3.4 Low-energy deuteron elastic Compton scattering

Compton-scattering experiments that have sought to investigate the electromagnetic polarisabilities of the neutron are considerably fewer in number than those on the proton, primarily due to the lack of free neutron targets. Moreover, for the proton, the electric ( $\alpha_{E1}^{(p)}$ ) and magnetic ( $\beta_{M1}^{(p)}$ ) polarisabilities enter at order  $\omega^2$  in the cross section (where  $\omega$  is the photon energy) due to an interference with the leading Thomson amplitude. For a “free” neutron, there is no Thomson term (the neutron is uncharged), so the polarisabilities enter at order  $\omega^4$  and are much harder to determine.

It is worthwhile to get a historical perspective on the subject of the neutron polarisabilities before proceeding with the Compton discussion. The first experiments designed to investigate this subject used a totally different technique. Neutron scattering at very low energies ( $E_n < 600$  keV) in the Coulomb field of a high- $Z$  target (such as  $^{208}\text{Pb}$ ) is sensitive to the electric polarisability of the projectile neutron. The initial experiments [128, 129] had very large error bars, but the later experiments of Schmiedmayer et al. [130, 131] reported a rather precise extraction of the neutron electric polarisability:  $\alpha_{E1}^{(n)} = 12.0 \pm 1.5(\text{stat}) \pm 2.0(\text{syst})$ . These results were challenged by Koester et al. [132, 133], who obtained  $\alpha_{E1}^{(n)} = 0 \pm 5$ , and by Enik et al. [134], who argued that Schmiedmayer [131] had underreported the systematic errors of the experiment and extracted  $\alpha_{E1}^{(n)} = 7\text{--}19$  using the Schmiedmayer data set. A more recent measurement by Laptev et al. [135] also raises questions about the result of Ref. [131]. This debate has not been resolved, and here we can only say that the neutron-scattering technique, although successful in determining polarisabilities in more weakly bound systems, appears to have led to a weak constraint on  $\alpha_{E1}^{(n)}$ , at best.

The failure of these attempts to measure the neutron electric polarisability in a reliable way motivated alternate efforts to access the neutron polarisabilities (both  $\alpha_{E1}^{(n)}$  and  $\beta_{M1}^{(n)}$ ). This led to the use of Compton scattering on deuterium, the simplest nuclear target containing a neutron, via either the quasi-free  $d(\gamma, \gamma'n)p$  reaction or the elastic-scattering  $d(\gamma, \gamma)d$  reaction. To date, there have been three quasi-free experiments—a pioneering experiment at MAMI [64, 65], a later experiment at SAL [66] and the most recent one at MAMI [68]. The last is the most precise, but, even so, the value of  $\alpha_{E1}^{(n)}$  was obtained to no better than 30% when the statistical, systematic and model errors are combined linearly. This emphasises the difficulty of the quasi-free measurements. By contrast, for elastic scattering on deuterium, the Thomson term is recovered, so the polarisability extraction is similar (in principle) to the proton case, except for the fact that only the *sum* of the proton and neutron polarisabilities ( $\alpha_{E1}^{(p)} + \alpha_{E1}^{(n)}$  and  $\beta_{M1}^{(p)} + \beta_{M1}^{(n)}$ ) can be unambiguously deduced from the data. However, a major experimental challenge must be confronted due to the fact that the deuteron breakup channel is only separated from the elastic channel by 2.225 MeV (plus recoil). As a result of this stringent requirement, only four measurements of the  $d(\gamma, \gamma)d$  reaction have been performed to date. These experiments are reviewed below, followed by the quasi-free experiments in Section 3.5.

The first elastic-scattering experiment was performed at Illinois by Lucas [25], using an identical setup to the experiment of Federspiel [20] on the proton. Two large 25.4 cm  $\times$  25.4 cm NaI detectors were used to detect scattered photons at four lab angles ( $50^\circ$ ,  $75^\circ$ ,  $110^\circ$ ,  $140^\circ$ ) at an incident photon energy of  $\omega_{\text{lab}} = 49$  MeV, as well as at two scattering angles ( $60^\circ$  and  $135^\circ$ ) at a photon energy of  $\omega_{\text{lab}} = 69$  MeV. To extract the elastic-scattering cross sections, the inelastic contributions to the measured scattering spectra were generated using the Impulse Approximation, and then the sum of elastic and inelastic contributions was fitted to the individual spectra. The statistical uncertainties for the deduced elastic cross sections were quite good ( $\pm 4\text{--}13\%$ ). However, one drawback is that these statistics were obtained at the cost of summing all of the tagger channels in the entire tagger focal plane for each energy point, so that each data point constitutes an average photon-energy bin width of 6.5 or 7.7 MeV, respectively. This is a rather wide energy bin, although if the cross section is linear with energy, there are no serious complications when comparing the data to theory. Systematic uncertainties were in the range  $\pm 3.6\text{--}$

4.0% for the data, primarily due to *correlated* factors such as photon flux ( $\pm 1\%$ ), detector acceptance ( $\pm 1\text{--}2\%$ ), target thickness ( $\pm 2\%$ ), possible contamination of the yield due to inelastic contributions ( $\pm 1\text{--}2\%$ ), and simulation uncertainties ( $\pm 1\%$ ), leading to a *correlated* systematic uncertainty of  $\pm 3\%$ . The remaining systematic uncertainties, at the level of  $\pm 2.0\text{--}2.5\%$ , were due to subtraction of randoms and empty-target contributions, giving an overall total of  $\pm 3.6\text{--}4.0\%$ .

The experiment of Lundin et al. [27] was conducted at Lund and was very similar in energy and angle to the Lucas experiment [25]. Three large NaI detectors were used at two “nominal” photon energies ( $\omega_{\text{lab}} = 55$  and  $66$  MeV) and at three “nominal” lab angles ( $45^\circ$ ,  $125^\circ$ ,  $135^\circ$ ). In this case, however, many separate runs were taken over an extended period of time, resulting in multiple independent data points which more or less overlap. There were 3 runs at  $54.6\text{--}55.9$  MeV and 3 runs at  $65.3\text{--}67.0$  MeV, where the actual photon energy varied slightly over those ranges. In each of the 6 runs, the detector angles also varied slightly from the nominal values, but the measured angles basically form two clusters—a forward cluster near  $45^\circ$  and a backward cluster near  $130^\circ$ . In the end, the total data set comprised 18 data points, although the overall kinematic coverage is actually rather limited due to the overlap of the various points. For this experiment, the inelastic contribution from deuteron breakup was not simulated, but rather it was excluded (to a large extent) from the elastic strength by setting a tight summing window in the scattered  $\gamma$ -ray spectra. The statistical uncertainties of the extracted cross sections are in the range  $\pm(8\text{--}24)\%$ , which are roughly double those of Lucas [25]. In addition, the energy width of each point was fairly broad (10 MeV wide) due to summing all tagger channels in the entire tagger focal plane to increase the statistics. Systematic uncertainties due to photon flux ( $\pm 5\%$ ), detector acceptance ( $\pm 4\%$ ), target thickness ( $\pm 2\%$ ), and possible contamination of the yield due to inelastic contributions ( $\pm 3\%$ ) were *correlated* among all the data points, for a total of  $\pm 7.5\%$ . In addition, background subtraction gave an uncorrelated systematic error of at most  $\pm 4\%$ , leading to an overall reported systematic uncertainty of  $\pm 7\text{--}14\%$  for the measured data. We note that the lower limit of this range ( $\pm 7\%$ ) is slightly inconsistent with the overall correlated systematic uncertainty stated above ( $\pm 7.5\%$ ); we cannot explain this discrepancy, although there are indeed several data points in Table I of Ref. [27] which have systematic errors below  $\pm 7.5\%$ .

Both of the previous experiments spanned an energy range which is only moderately sensitive to the polarisabilities. The experiment of Hornidge et al. [26] pushed the energy higher, where the sensitivity increases. This experiment was performed at SAL using the large-volume BUNI detector. In many respects, this experiment was similar to the Hallin experiment on the proton [21], except that Hornidge used tagged photons at energies  $\omega_{\text{lab}} = 84\text{--}105$  MeV and measured 5 angles sequentially in the lab angular range  $35^\circ\text{--}150^\circ$ . The BUNI detector was crucial for separating the elastic-scattering peak from the inelastic contributions which are only 2.2 MeV apart. With a scattered photon energy of  $\sim 100$  MeV, a large-volume NaI detector with an energy resolution better than  $\Delta E/E \sim 2\%$  was required to achieve this separation. With the use of a tight summing region in the scattering spectra, the BUNI resolution ensured that the elastic-scattering contributions could be cleanly determined. The resulting statistical uncertainties for the 5 data points are fairly good ( $\pm 5\text{--}10\%$ ). One issue, however, as seen before, is that the full focal plane was added together to improve the statistics, and, as such, the data points each constitute a broad energy bin with a width of 21 MeV. Systematics due to photon flux ( $\pm 1\%$ ), solid angle ( $\pm 1.6\%$ ), detection efficiency ( $\pm 3.6\%$ ), and target thickness ( $\pm 2.5\%$ ) were *correlated* among the data points for a total of  $\pm 5\%$ . In addition, uncertainties due to energy calibration ( $\pm 1\text{--}5\%$ ) give a range of  $\pm(5\text{--}7)\%$  for the overall systematic uncertainty of the data.

A potential issue in the analysis of the deuteron elastic-scattering data, as mentioned above, is that the widths of the energy bins themselves are often non-negligible, e.g. the data of Ref. [26] are combined into a single photon-energy bin that is 21 MeV wide. One might be concerned about how the energy dependence of experimental acceptances and systematic errors affect these data. However, some reassurance is provided by the analysis of Ref. [136], which showed that comparing the average cross section over a wide experimental bin with the point theoretical cross section at the centre of the bin,

as done in theoretical analyses thus far, is entirely reasonable. In fact, the difference between carefully averaging over the energy bin and simply taking the cross section at the central energy is less than 1%, even for the SAL bin widths of 21 MeV, and nearly an order of magnitude smaller for the other experiments; see also [137] for more details.

As in the proton case, the experimental systematic errors have been separated into two pieces: (1) point-to-point contributions which have been added in quadrature to the statistical error, and (2) overall scaling contributions for the whole data set which have been subsumed into a floating normalisation, see Eq. (4.19) in Section 4.4. We have checked that these separate contributions to the systematic error combine to give the overall stated systematic error of the data points. In cases where a discrepancy exists, as for some of the Lund data [27], the point-to-point contributions have been taken to be zero.

A summary of all of the deuteron experiments is included in Table 3.2. Overall, the three published experiments [25–27] provide a total of 29 data points in essentially 4 energy bins, centred at lab energies between 49 and 95 MeV. The angular coverage is rather limited and overlaps between experiments, with only 2 to 5 angles per energy bin. To a large extent, this is attributed to the difficulties in clearly differentiating between elastic and inelastic (deuteron breakup) Compton events, which are only separated by the small deuteron binding energy. Experimental statistical and systematic errors range

Legend	First Author	$\omega_{\text{lab}}$ (MeV)	$\theta_{\text{lab}}$ (deg)	Ref.	Reaction	$N_{\text{data}}$	Symbol
Illinois 94	Lucas	49, 69	50–140	[25]	elastic	6	●
SAL 00	Hornidge	94	35–150	[26]	elastic	5	◆
Lund 03	Lundin	55, 66	45, 125, 135	[27]	elastic	18	▲
Lund 10	Myers	67–116	60, 120, 150	[138]	elastic	8	
Lund 12	Shoniyozov	81–116	60,90,120,150	[139]	elastic		
MAMI 90	Rose	80–130	90, 135	[64, 65]	quasi-free	2	
SAL 00 QF	Kolb	247	135	[66]	quasi-free	1	
MAMI 02	Kossert	211–377	136	[67, 68]	quasi-free	9	

Table 3.2: Compton-scattering experiments on the deuteron, including elastic and quasi-free scattering. The last column indicates the corresponding symbols used in the figures for elastic scattering. The most recent Lund data (2010 and 2012) were not yet available to be included in these figures.

over  $\pm 5$  to  $\pm 24\%$  and  $\pm 4$  to  $\pm 14\%$ , respectively. At the present time, these are the data that have been included in global EFT fits aimed at extracting the neutron polarisabilities. We note that this limited deuteron database contains roughly 10% of the volume of data available for the proton, where the latter extends far into the  $\Delta(1232)$  resonance region and generally has substantially better energy resolution and angular coverage, as well as lower statistical and systematic uncertainties.

There is some promise, however, that the database will be expanded. A more recent experimental programme has been conducted at Lund [138, 139] in an energy range higher than the earlier Lundin data and comparable to that of Hornidge. The tagged energy range was broader than any previous experiment ( $\omega_{\text{lab}} = 67\text{--}116$  MeV) and covered four lab angles ( $60^\circ$ ,  $90^\circ$ ,  $120^\circ$  and  $150^\circ$ ). A key improvement, moreover, is that the measurements were performed using three large-volume high-resolution NaI detectors simultaneously in a single configuration—the BUNI detector already described, the CATS detector which had been transported from MAMI to Lund for this purpose, and the DIANA detector (60 cm diameter  $\times$  50 cm long) from the University of Kentucky. This enabled three angles to be measured simultaneously in a single run period. It also facilitated a cross-check on systematics by enabling the measurement of repeat angles with different NaI detectors over the various run periods. These data

are still being finalised, and so there are no results to be shown at the time of this review.

### 3.5 Deuteron quasi-free Compton scattering

Compton scattering on a “free” neutron is the objective of the quasi-free reaction  $d(\gamma, \gamma'n)p$  in which a kinematic configuration is chosen such that the proton is predominantly a spectator, and the scattered photon (backward direction) and recoil neutron (forward direction) are detected in coincidence. Since this is a breakup process, it has not yet been treated in Effective Field Theory, although it is now feasible to do so and work is beginning along these lines. Nevertheless, a brief review of quasi-free experiments to date is appropriate, since it so closely relates to the objective of obtaining precise information about the neutron polarisability.

The pioneering experiment was performed by Rose et al. [64, 65] at MAMI using a 130 MeV bremsstrahlung photon beam. Two 25.4 cm  $\times$  35.6 cm NaI detectors were located at 135° and 90° on one side of the beamline and four plastic scintillators were located at 22°, 31°, 39° and 49° on the other side. The data were summed over a wide energy range, from 80 MeV up to the endpoint. Since the endpoint was below pion threshold, all coincidence events were unambiguously from Compton scattering (i.e. no contamination from  $\pi^0$  production). Due to poor statistics and the low energy range of the measurement, only an upper limit could be established for the neutron electric polarisability  $\alpha_{E1}^{(n)}$ . Using a dispersion theory analysis, this experiment gave results of  $\alpha_{E1}^{(n)} = 10.7^{+3.3}_{-10.7}$  and  $\beta_{M1}^{(n)} = 5.3^{+10.7}_{-3.3}$  for the neutron, where a sum-rule value of  $\alpha_{E1}^{(n)} + \beta_{M1}^{(n)} = 16$  has been assumed. We note that this was the first experimental determination (1990) of the neutron polarisability via Compton scattering, since it precedes the initial elastic-scattering experiment of Lucas (1994) by 4 years.

At the low energies of the above experiment, there is a sizable model dependence in the polarisability values extracted from the dispersion analysis. Levchuk et al. [140, 141] determined that the model dependence could be minimised (and the sensitivity to polarisability maximised) by moving to higher energies like 200–300 MeV. At SAL, this was undertaken by Kolb et al. [66] using tagged photons at an average energy of 247 MeV (ranging over 236–260 MeV). Scattered photons were measured at 135° in the large-volume BUNI detector on one side of the beamline and the recoil neutrons were detected in an 85-cell liquid-scintillator array centred at 20° on the other side (note that this is much more forward than Rose [65]). An important consistency check was performed in this experiment by simultaneously measuring the quasi-free scattering reaction on the proton using the same setup and comparing those results to the known case of the free proton. For the extraction of the neutron quasi-free cross section at these energies, a simulation of the significant  $\pi^0$  background is absolutely necessary. This is rendered more difficult by the smearing of the Compton and pion events due to Fermi motion of the bound nucleon in deuterium. In the end, this experiment yielded an independent lower limit for the neutron electric polarisability  $\alpha_{E1}^{(n)}$ . Combining this lower limit with the upper limit from Rose, the final values obtained from a dispersion theory analysis gave  $\alpha_{E1}^{(n)} = 13.6^{+0.4}_{-6.0}$  and  $\beta_{M1}^{(n)} = 1.6^{+6.0}_{-0.4}$  for the neutron, based on a sum-rule value of  $\alpha_{E1}^{(n)} + \beta_{M1}^{(n)} = 15.2$  [141].

The most definitive quasi-free scattering experiment was performed at MAMI by Kossert et al. [67, 68] using the large-volume CATS detector at 136° and a 30-cell liquid-scintillator array at 21° on the opposite side of the beamline. The tagged-photon energy range was 200–400 MeV. This experiment was very similar to the SAL experiment [66] in design, but it produced 9 data points over this energy range, as compared to a single SAL point at 247 MeV. This data set allowed much tighter constraints to be placed on the extracted polarisability values for the neutron. The results from the Kossert experiment were  $\alpha_{E1}^{(n)} = 12.5 \pm 1.8(\text{stat})^{+1.1}_{-0.6}(\text{syst}) \pm 1.1(\text{theory})$  and  $\beta_{M1}^{(n)} = 2.7 \mp 1.8(\text{stat})^{+0.6}_{-1.1}(\text{syst}) \mp 1.1(\text{theory})$  with the inclusion of the sum-rule condition  $\alpha_{E1}^{(n)} + \beta_{M1}^{(n)} = 15.2$ . The model used to obtain these numbers will be discussed in Section 5.5, where a critical assessment of the theory error bar will be provided as well. In fact, these results for neutron polarisabilities depended on assuming the model value of  $\gamma_{\pi}^{(n)}$  obtained



by L'vov et al. [142]. As pointed out by Levchuk et al. [140], the quasi-free cross section in these kinematics is rather sensitive to the backward spin polarisability of the neutron,  $\gamma_\pi^{(n)}$ . It is therefore reassuring that the experiment also afforded an independent determination of this quantity. By allowing both  $\alpha_{E1}^{(n)} - \beta_{M1}^{(n)}$  and  $\gamma_\pi^{(n)}$  to vary as free parameters, a fit to the quasi-free cross section yielded a value of  $\gamma_\pi^{(n)} = 58.6 \pm 4.0$  (including the  $\pi^0$  pole contribution; cf. Section 2.1). This is entirely consistent with the model value employed to obtain the numbers quoted above. The addition of  $\gamma_\pi^{(n)}$  as a free parameter in fitting the cross section did not alter the extracted values of  $\alpha_{E1}^{(n)}$  and  $\beta_{M1}^{(n)}$  at all, except to slightly increase the statistical error bar. Up to the present, this remains the only experimental determination of the backward spin polarisability of the neutron.

## 4 Compton scattering from the nucleon

### 4.1 Dispersion relations

In this section, we review dispersion-relation (DR) calculations which have been used to extract proton polarisabilities from Compton-scattering data. For a thorough review, the reader is referred to Ref. [15]. A short description of the DR approach can also be found in Ref. [143].

To write down DRs, we must construct a complete set of amplitudes for Compton scattering in accordance with the dictates of Lorentz covariance, parity and time-reversal invariance. These amplitudes must be free of kinematical singularities. The basis of L'vov [142, 144, 145] has been employed in Refs. [88, 146]. These amplitudes are linear combinations of the  $A_i$ 's defined in Eq. (2.1), with coefficients which vary with angle. The relationship can be derived from Appendix A of Ref. [88]. The L'vov amplitudes, here denoted by  $B_i$ , are written as functions of Mandelstam  $t$  and the variable  $\nu$ , defined as  $\nu = (s - u)/(4M_N) = \omega_{\text{lab}} + t/(4M_N)$ . Under crossing symmetry, they obey  $B_i(-\nu, t) = B_i(\nu, t)$ . Within the DR approach, the  $B_i$ 's are constructed by adding the nucleon and pion-pole contributions to an integral over the spectrum of intermediate excitations. Applying Cauchy's theorem (with a suitable contour) to the function  $B_i(\nu', t)/(\nu' - \nu - i\epsilon)$  yields

$$\text{Re } B_i(\nu, t) = B_i^{\text{Born}}(\nu, t) + \frac{2}{\pi} P \int_{\nu_0}^{\infty} d\nu' \nu' \frac{\text{Im}_s B_i(\nu', t)}{\nu'^2 - \nu^2}, \quad (4.1)$$

with  $B_i^{\text{Born}}$  the contributions from the Born (nucleon- and pion-pole) graphs and  $P$  indicating a principal-value integral. This is an unsubtracted dispersion relation which applies at the chosen value of  $t$  if we may neglect the contribution from the semi-circle at infinity.  $B_i$  can then be reconstructed from the Born terms and its imaginary part,  $\text{Im}_s B_i$ , which itself is  $1/(2i)$  times the discontinuity across the  $s$ -channel cut of the Compton process. This imaginary part can thus be obtained from nucleon-pion photoproduction amplitudes, and the integral starts at  $\nu_0 = m_\pi + (m_\pi^2 + t/2)/(2M_N)$ , which is the  $\pi N$  threshold in the lab frame—the frame in which we choose to work throughout this sub-section. Pion photoproduction is the lowest channel that contributes to the imaginary part, since we neglect the process  $\gamma p \rightarrow e^+ e^- \gamma p$  (Delbrück scattering) and the effect of  $\gamma p$  intermediate states, as these contributions to  $\sigma_T$  are suppressed by powers of  $\alpha_{\text{EM}}$  compared to the hadronic ones.

The dispersion relations for  $t = 0$  (i.e.  $\theta = 0$ ) are of particular interest because the optical theorem states that the imaginary part of the forward amplitude is equal to a kinematic factor times the total cross section for photoabsorption. As discussed in Section 2.1, only two amplitudes ( $A_1$  and  $A_3$ ) survive for forward Compton scattering, and  $\sigma_T(\omega')$  does *not* fall off fast enough as  $\omega' \rightarrow \infty$  for  $A_1$  to obey an unsubtracted dispersion relation such as Eq. (4.1). To deal with this, we replace  $A_1(\omega_{\text{lab}}, z = 1)$  with the function  $A_1(\omega_{\text{lab}}, 1) - A_1(0, 1)$  in the argument that led to Eq. (4.1) and obtain the once-subtracted

dispersion relation:

$$\text{Re } A_1(\omega_{\text{lab}}, 1) = A_1(0, 1) + \frac{2\omega_{\text{lab}}^2}{\pi} P \int_{\omega_\pi}^{\infty} d\omega' \frac{\sigma_T(\omega')}{\omega'^2 - \omega_{\text{lab}}^2}, \quad (4.2)$$

with  $\omega_\pi = m_\pi + m_\pi^2/(2M_N)$ . In the case of  $A_3$ , however, Regge arguments allow us to anticipate an unsubtracted dispersion relation,

$$\text{Re } A_3(\omega_{\text{lab}}, 1) = \frac{\omega_{\text{lab}}}{\pi} P \int_{\omega_\pi}^{\infty} d\omega' \omega' \frac{\sigma_{1/2}(\omega') - \sigma_{3/2}(\omega')}{\omega'^2 - \omega_{\text{lab}}^2}, \quad (4.3)$$

where  $\sigma_{1/2}$  ( $\sigma_{3/2}$ ) is the total cross section for a photon-nucleon system of helicity 1/2 (3/2).

If the integrals in Eqs. (4.2, 4.3) converge, then each side may be expanded as a Taylor series about  $\omega_{\text{lab}} = 0$ . Inserting the low-energy expansions of Eq. (2.5) on the left-hand side then yields a variety of sum rules for the structure coefficients in those expansions. For example, from Eq. (4.2) we obtain the Baldin sum rule quoted in Eq. (2.7). Meanwhile, equating terms of  $\mathcal{O}(\omega_{\text{lab}})$  in Eq. (4.3) yields the famous sum rule of Gerasimov, Drell and Hearn (GDH) [147, 148] relating the square of  $\kappa^{(p)}$  to an integral over  $\sigma_{1/2} - \sigma_{3/2}$ . The terms of  $\mathcal{O}(\omega_{\text{lab}}^3)$  yield the Forward Spin Polarisability (or  $\gamma_0$ ) sum rule [8, 149], which was also listed in Eq. (2.7). Recently, Pasquini, Drechsel and Pedroni took such arguments one order further, obtaining and evaluating the sum rule for the ‘‘higher-order forward spin polarisability’’,  $\bar{\gamma}_0$  [150]:

$$\bar{\gamma}_0 = \frac{1}{4\pi^2} \int_{\omega_\pi}^{\infty} d\omega' \frac{\sigma_{1/2}(\omega') - \sigma_{3/2}(\omega')}{\omega'^5}, \quad (4.4)$$

which is defined as the second term in the Taylor expansion of the dynamical forward spin polarisability  $\gamma_0(\omega)$  about  $\omega = 0$ . These three sum rules demonstrate that higher-order terms in the Taylor expansion of  $A_1$  and  $A_3$  about  $\omega = 0$  correspond to integrands with additional powers of the excitation energy in the denominator. Consequently, higher-order coefficients are increasingly dominated by near-threshold physics, and so their dependence on assumptions regarding high-energy pieces of the integral decreases markedly. In particular, the GDH sum rule receives approximately 10% of its total value from contributions above  $\sqrt{s} - M_p = 2$  GeV, while less than 4% of the Forward Spin Polarisability sum rule comes from  $\sqrt{s} - M_p > 800$  MeV [15]. One corollary is that dispersion-relation results for  $\gamma_0$  and (even more so) for  $\bar{\gamma}_0$  are quite stable against assumptions about the high-energy behaviour. So, for instance, Ref. [15] quoted  $\gamma_0^{(p)} = -1.01 \pm 0.08(\text{stat}) \pm 0.10(\text{syst})$ , which was updated in Ref. [150] to  $\gamma_0^{(p)} = -0.90 \pm 0.08(\text{stat}) \pm 0.11(\text{syst})$ . Ref. [151] makes additional model assumptions and found a marginally consistent result:  $\gamma_0^{(p)} = -0.58 \pm 0.20$ . Another corollary is that dispersion relations for  $A_1$  and  $A_3$ , upon which multiple subtractions have been made, predict that the energy dependence of these functions is driven entirely by chiral (i.e. near-threshold) physics.

From such analyses we learn that unsubtracted dispersion relations do not hold for the L’vov amplitudes  $B_1$  and  $B_2$  and that the unsubtracted dispersion relation for the amplitude  $B_3$  converges only slowly. It is therefore more appropriate to consider once-subtracted dispersion relations at fixed  $t$  [146]:

$$\text{Re } \bar{B}_i(\nu, t) = \bar{B}_i(0, t) + \frac{2}{\pi} \nu^2 P \int_{\nu_0}^{\infty} d\nu' \nu' \frac{\text{Im}_s B_i(\nu', t)}{\nu'(\nu'^2 - \nu^2)}, \quad (4.5)$$

at least in the cases  $i = 1, 2, 3$ . (Here the  $\bar{B}_i$ ’s are the structure parts, in analogy to the  $\bar{A}_i$ ’s of Section 2.) In order to obtain predictions from Eq. (4.5), it is necessary to provide the function  $B_i(0, t)$  as input.

A dispersion relation can also be written for  $\bar{B}_i(0, t)$ :

$$\bar{B}_i(0, t) = \bar{B}_i(0, 0) + B_i^{\pi^0}(0, t) - B_i^{\pi^0}(0, 0) + \frac{t}{\pi} \int_{4m_K^2}^{\infty} dt' \frac{\text{Im}_t B_i(0, t')}{t'(t' - t)} + \frac{t}{\pi} \int_{-\infty}^{-2m_\pi^2 - 4Mm_\pi} dt' \frac{\text{Im}_t B_i(0, t')}{t'(t' - t)} . \quad (4.6)$$

The possible intermediate states in the  $t$ -channel yield cuts along the positive  $t$ -axis, but as long as  $t < 4m_K^2$ , this is saturated by  $\pi\pi$  intermediate states. The main contribution which needs to be calculated to evaluate the function  $B_i(0, t)$  is thus  $\gamma\gamma \rightarrow \pi\pi \rightarrow N\bar{N}$ . In Ref. [146], the  $\pi\pi \rightarrow N\bar{N}$  amplitudes of Ref. [152] were employed, and a model was constructed for  $\gamma\gamma \rightarrow \pi\pi$ .

Meanwhile, the  $s$ -channel integral in Eq. (4.5) is largely saturated by  $\pi N$  intermediate states, which mitigates the need for modelling of higher-energy physics in photoproduction. The  $\pi N$  contribution is evaluated using a contemporary parameterisation of the  $\gamma p \rightarrow \pi N$  data. Multi-pion intermediate states in the  $s$ -channel integral are evaluated from data on the inelastic decay channels of  $\pi N$  resonances, and their helicity structure is assumed to be the same as that of the  $\gamma p \rightarrow \pi N$  amplitudes. This introduces some model dependence in the DR evaluation, and there is also model dependence in the computation of the second,  $u$ -channel, integral in Eq. (4.6), since it requires the evaluation of amplitudes well into the unphysical region. However, the overall uncertainty in the evaluation of the DRs is very small since “...subtracted dispersion relations are essentially saturated at  $\nu = 0.4$  GeV.” [15]. Indeed, neglecting both the  $u$ -channel integral and the two-pion contributions changes the cross sections by only 3-5% [15].

The six subtraction constants  $b_i \equiv \bar{B}_i(0, 0)$  then remain as the only free parameters in this approach. These are equal to linear combinations of the six static dipole polarisabilities. In the results quoted below,  $b_4$ – $b_6$  are assumed to be derivable from unsubtracted forward dispersion relations, i.e. to obey:

$$b_i = \frac{2}{\pi} \int_{\omega_\pi}^{\infty} d\omega' \frac{\text{Im}_s B_i(\omega', 0)}{\omega'} \quad \text{with } i = 4, 5, 6 . \quad (4.7)$$

where  $b_3$  is often fixed from the Baldin sum rule. Therefore, at least three of the six static polarisabilities are assumed to be calculable from analyticity arguments, and only  $\alpha_{E1}$ ,  $\beta_{M1}$  and one spin polarisability (typically chosen to be  $\gamma_\pi$ ) are taken as free parameters in the fit. The formalism does not, however, demand that Eq. (4.7) be invoked. All six  $b_i$ 's could be taken as fit parameters, if sufficient data were available to determine them.

If one does not wish to take these parameters as input, one can continue to work with an unsubtracted dispersion relation instead, provided the Cauchy-theorem contour used in their construction is closed at a finite radius, rather than at  $\nu' = \infty$  [142]. This produces a third contribution on the right-hand side of Eq. (4.1),  $B_i^{\text{as}}$ , which is a piece resulting from integrating along a finite semi-circle of radius  $\nu_{\text{max}}$  in the complex plane. In Ref. [142] and subsequent works (see Ref. [153] for a review and Refs. [151, 154–156] for more recent developments), this contribution is parameterised by the exchange of a single particle in the  $t$ -channel, e.g. the  $\sigma$  meson in the case of  $B_1$ . Proceeding in this manner means that one is modelling the high-energy behaviour of the Compton amplitudes, and so a significant set of additional dynamical assumptions is introduced. The advantage of once-subtracted fixed- $t$  dispersion relations in which the subtraction function is fixed via Eq. (4.6) is that they contain minimal dynamical assumptions and are sensitive mainly to the well-constrained low-energy dynamics of the  $\pi N$  system.

Such dispersion relations do, however, require extrapolation of the imaginary parts into an unphysical region. In practice, this extrapolation is difficult to control for large values of  $t$ . Hyperbolic DRs provide a related approach, which, however, does not necessitate such an extrapolation. In hyperbolic DRs, the integration paths are hyperbolae in the Mandelstam plane which correspond to a fixed value of  $\text{cm}$  (or  $\text{lab}$ ) scattering angle. Thus they are often referred to as “fixed-angle dispersion relations”. The integrals in these calculations have a form similar to that found in subtracted fixed- $t$  DRs, but

additional kinematical factors are now present in the integrand. These factors cure the difficulties with the extrapolation of the integrand at large  $t$ , but lead to some problems with convergence at small angles. The two types of DRs are complementary: fixed- $t$  DRs are good at small angles, while fixed-angle dispersion relations work best at  $\theta_{\text{lab}} = 180^\circ$ . We note that such backward DRs have been used in their unsubtracted form to directly obtain sum rules for  $\alpha_{E1}^{(p)} - \beta_{M1}^{(p)}$  [157] and  $\gamma_\pi^{(p)}$  [158]. Results for these quantities from other analogous evaluations at  $\theta_{\text{lab}} = 180^\circ$  are given in Table 4.2 below. The values found for other angles within the domain of validity of the hyperbolic dispersion relations differ by  $\approx 10\%$  for  $\alpha_{E1}^{(p)} - \beta_{M1}^{(p)}$  and  $\gamma_\pi^{(p)}$  and by a few percent for other spin polarisabilities.

Reassuringly, if the same photoproduction data are used as input for both the hyperbolic and fixed- $t$  dispersion relations, then very good agreement is obtained for the shape of the low-energy  $\gamma p$  data (see Fig. 4.1). (The predictions for hyperbolic dispersion relations are only shown for  $\theta_{\text{lab}} \geq 107^\circ$ , as formally they do not converge forward of this point.) Within their expected range of validity, it is gratifying that all approaches agree at a level which is in accord with the size of the experimental error bars. However, we caution that when these curves are continued into the resonance region, more significant differences are seen [15, 159].

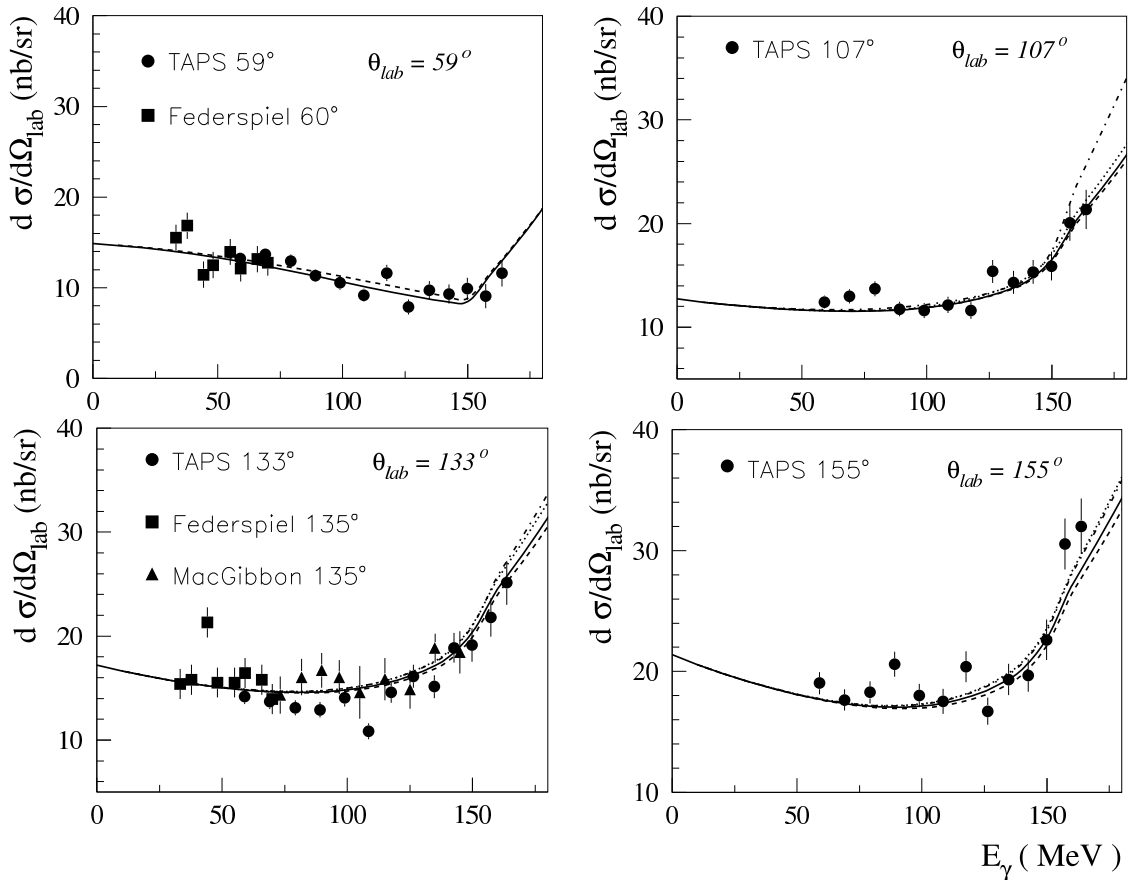


Figure 4.1: Differential cross section for  $\gamma p$  scattering as a function of  $\omega_{\text{lab}}$  at fixed lab angles. Experimental data are represented by the symbols, as indicated. Curves are for fixed- $t$  subtracted/unsubtracted DRs (solid/dashed) and for fixed-angle subtracted/unsubtracted DRs (dotted/dash-dotted). All results are shown for  $\alpha_{E1}^{(p)} - \beta_{M1}^{(p)} = 13.8$ ,  $\alpha_{E1}^{(p)} - \beta_{M1}^{(p)} = 10.0$ ,  $\gamma_\pi^{(p)} = 7$ . Figure modified from Fig. 20 in Ref. [15]. Used with permission.

Regardless, the good agreement in the vicinity of the pion threshold lends strong support to the extraction of proton polarisabilities using dispersion relations. Using fixed- $t$ , subtracted dispersion relations, the results of a fit to the data of Refs. [20, 22–24] for  $\alpha_{E1}^{(p)} + \beta_{M1}^{(p)}$  and  $\alpha_{E1}^{(p)} - \beta_{M1}^{(p)}$  are shown

in Table 4.2 in Section 4.3. The fit also determines  $\gamma_\pi^{(p)} = 10.4 \pm 1.8 \pm 3.2$  and has a  $\chi^2/\text{d.o.f.} = 1.2$ . In this global analysis, the normalisation of each data set was allowed to float (see Eq. (4.19) below) within an assigned uncertainty of 3%. The first error bar is obtained by fitting with fixed values of the normalisation constants, while the second represents the systematic uncertainty due to these normalisation effects.

## 4.2 Chiral EFT for $\gamma p$ and $\gamma n$ scattering

### 4.2.1 Principles of $\chi$ EFT

There are many excellent reviews of chiral EFTs, and we will give only a summary here. For those interested in learning more, the most comprehensive introduction to the subject are the lectures by Scherer and his subsequent book with Schindler [160, 161]. Recent reviews include Bijnens [162] for the meson sector and Bernard [163] for the baryon sector; see also references therein. The classic review of Bernard et al. [98] is still quite extensively used. Reviews covering the few-nucleon sector include those of Beane et al. [164], Bedaque and van Kolck [165], Epelbaum et al. [166], and Machleidt and Entem [167]. Phillips' review specifically covers the applications to electromagnetic reactions on nucleons and nuclei [168].

We start by briefly reviewing  $\chi$ PT, in which the dominant dynamics is directly linked to the chiral symmetry of QCD. Subsequently, we will introduce the  $\Delta(1232)$  as a dynamical degree of freedom in a more general chiral EFT.

Pionic  $\chi$ PT is a mature subject with a voluminous literature, but most of the details are scarcely relevant here. The Lagrangian initially includes all allowed terms with either two derivatives or one factor of  $m_\pi^2$ , reflecting the fact that soft pions are non-interacting in the chiral limit. The resulting  $\mathcal{L}_\pi^{(2)}$ —see Eq. (4.8)—contains one term of each type and generates the free-pion propagator away from the chiral limit. Writing  $\mathcal{L}_\pi^{(2)}$  in a chirally symmetric way generates non-vanishing amplitudes for 4, 6, ... pions interacting at a point, which are predictive at this order. These reproduce Weinberg's low-energy theorem for  $\pi\pi$  scattering [169] and give lowest-order predictions for the scattering lengths which are within 25% of currently accepted values. At next-to-leading order (NLO,  $\mathcal{O}(P^4)$ ) there are contributions both from terms in the fourth-order Lagrangian  $\mathcal{L}^{(4)}$  (with, e.g., four derivatives) and also from one-loop diagrams such as a single rescattering; at next-to-next-to leading order (N<sup>2</sup>LO) there are contributions from  $\mathcal{L}^{(6)}$ , from two-loop diagrams and also from one-loop diagrams in which one of the vertices is taken from  $\mathcal{L}^{(4)}$  [170]. Of course, beyond  $\mathcal{L}^{(2)}$  unknown LECs enter, and various strategies exist. One can fit to data and excellent agreement with the scattering amplitudes near threshold is obtained [162, 171, 172]. Alternatively, lattice QCD can now constrain the fourth-order LECs [60–62]. Whichever approach is taken,  $\pi\pi$  scattering is a textbook example of a systematically improvable EFT calculation.

A chiral Lagrangian with nucleon fields coupled to pions and photons was first investigated beyond tree level by Gasser et al. [173]. Since the Dirac equation is linear in derivatives, terms with both odd and even numbers of derivatives appear. It was immediately recognised that the simplest possible loop contribution to the self-energy, from one  $\pi N$  loop using dimensional regularisation, does not obey the power counting found in the pionic case; rather than being suppressed by some specific power of  $m_\pi/\Lambda_\chi$  relative to the leading nucleon mass, it generates an entire series of powers of  $m_\pi/M_N$ , including a contribution  $\sim M_N$ . This effectively precludes the possibility of a systematic calculation in which all omitted diagrams contribute at a higher order in  $m_\pi/\Lambda_\chi$  than the desired order.

In subsequent years, methods to tame this problem and restore power counting to the theory with Dirac nucleons were developed. The first solution which was proposed, and the one which has been used in most work on Compton scattering, is called Heavy-Baryon  $\chi$ PT (HB $\chi$ PT) [98, 174, 175]. Other approaches will be mentioned in Section 4.2.7. In the framework of HB $\chi$ PT, the nucleon mass is



recognised to be of the same magnitude as  $\Lambda_\chi$ , and so the free Dirac Lagrangian contains terms which contribute at different chiral orders in low-energy processes: specifically the mass and energy are zeroth order while the momentum is first order (i.e. of order  $m_\pi$ ). By decomposing the nucleon field into “large” and “small” components (upper and lower components in the nucleon rest frame) and by integrating out the “small” component, one is left with a theory of Pauli spinors. As guaranteed by the relativistic starting point, Lorentz invariance is maintained in the new Lagrangian, but perturbatively, with corrections of order  $(P/M_N)^{n+1}$  when working to  $n$ th order. The mass and its contribution to the energy cancel and disappear from the leading-order Lagrangian  $\mathcal{L}_{\pi N}^{(1)}$ —see Eq. (4.9). From  $\mathcal{L}_{\pi N}^{(2)}$  onward, terms appear which have been generated by the heavy-baryon reduction, and so terms with a fixed coefficient proportional to  $1/M_N^{n-1}$  at  $n$ th order occur, in addition to those with an undetermined LEC. In this theory, corrections to the bare nucleon mass arise as expected at second order, with a contribution proportional to  $m_\pi^2$  (or equivalently  $m_q$ ) with the LEC  $c_1$  as its coefficient (this also gives the leading contribution to the pion-nucleon sigma term—see Eq. (4.10)). Then, at third order, the loop diagram gives a finite contribution proportional to  $m_\pi^3$  only. (The contribution needs to be finite, because terms in the Lagrangian can only involve integer powers of  $m_q$  or equivalently, even powers of  $m_\pi$ . Thus there can be no LEC to cancel a divergence at  $m_\pi^3$ .) HB $\chi$ PT does have a transparent power counting which matches that in the mesonic theory. The Lagrangian to third order was developed in Refs. [176–179], and then to fourth order in Refs. [180, 181].

One comment on power counting and electromagnetic processes: since a single Lagrangian term with a gauged derivative can contribute either a power of momentum or a factor of  $|e| = \sqrt{4\pi\alpha_{\text{EM}}}$ , and since the magnitude of  $|e|$  and of  $m_\pi/\Lambda_\chi$  are comparable, they will be considered interchangeable in the perturbative expansion. This is just a matter of bookkeeping provided the only photons in the process are external ones: Compton scattering from the nucleon, for instance, will start with the Thomson term at  $\mathcal{O}(P^2)$ , and working to N<sup>2</sup>LO will involve terms from the fourth-order Lagrangian. Photon loops can also be included; their effects will generally be of the same size as strong isospin-splitting effects at the appropriate order, and both have so far been ignored in Compton scattering.

#### 4.2.2 The Lagrangian for Compton scattering in $\chi$ EFT

Here we discuss the relevant terms in the Lagrangian for the construction of the Compton scattering amplitude to fourth order in HB $\chi$ PT. The full Lagrangian needs to be written in terms of building blocks with appropriate chiral properties, and hence every term can give rise to interactions with multiple pions. The usual notation is compact but far from transparent. Below we retain only the relevant structures for our purposes:

$$\mathcal{L}_\pi^{(2)} = \frac{1}{2} \partial_\mu \phi \cdot \partial^\mu \phi + e A_\mu \epsilon_{3ij} \phi_i \partial^\mu \phi_j + \frac{1}{2} e^2 A_\mu A^\mu (\phi_1^2 + \phi_2^2) - \frac{1}{2} m_\pi^2 \phi^2 + \dots \quad (4.8)$$

$$\mathcal{L}_{\pi N}^{(1)} = \psi^\dagger (i v \cdot D + g_A u \cdot S) \psi \quad (4.9)$$

$$\begin{aligned} \mathcal{L}_{\pi N}^{(2)} = & \psi^\dagger \left\{ \frac{1}{2M_N} \left( (v \cdot D)^2 - D^2 - i g \{ S \cdot D, v \cdot u \} \right) + 4c_1 m_\pi^2 \left( 1 - \frac{1}{2f_\pi^2} \phi^2 \right) \right. \\ & \left. + \left( c_2 - \frac{g_A^2}{8M_N} \right) (v \cdot u)^2 + c_3 u \cdot u - \frac{i}{4M_N} [S^\mu, S^\nu] e F_{\mu\nu} \left( (1 + \kappa^{(s)}) + (1 + \kappa^{(v)}) \tau_3 \right) \right\} \psi + \dots \quad (4.10) \end{aligned}$$

$$\mathcal{L}_{\pi N}^{(4)} = 2\pi e^2 \psi^\dagger \left\{ \frac{1}{2} (\delta\beta^{(s)} + \delta\beta^{(v)} \tau_3) g_{\mu\nu} - ((\delta\alpha^{(s)} + \delta\beta^{(s)}) + (\delta\alpha^{(v)} + \delta\beta^{(v)} \tau_3) v_\mu v_\nu \right\} F^{\mu\rho} F^\nu{}_\rho \psi + \dots \quad (4.11)$$

where  $\psi$  is the nucleon field,  $\phi_a$  are the pion fields,  $F^{\mu\nu}$  is the electromagnetic field tensor and  $D^\mu \equiv \partial^\mu - ieQA^\mu$  is the gauged derivative;  $v^\mu = g^{0\mu}$  and  $S^\mu = (0, \vec{\sigma}/2)$  in the rest frame of the nucleon. Since this is meant to be an expansion around the chiral limit of QCD, the LECs written here as  $g_A$ ,  $f_\pi$ ,  $\kappa$  etc. are actually “bare” quantities which will differ from the physical quantities by loop corrections which

only vanish in the chiral limit. This distinction is relevant at  $\mathcal{O}(P^4)$ . The object  $u_\mu$  is given by

$$u_\mu = -\frac{1}{f_\pi}(\tau_a \partial_\mu \phi_a + e\epsilon^{a3b} \tau_a \phi_b A_\mu + \dots) . \quad (4.12)$$

For the physical values, we use  $m_\pi^\pm = 139.6$  MeV,  $f_\pi = 92.42$  MeV,  $M_N = M_p = 938.3$  MeV,  $g_A = 1.267$ ,  $\kappa^{(s)} = -0.22$  and  $\kappa^{(v)} = 3.71$ . The neutral pion mass,  $m_{\pi^0} = 134.98$  MeV, is typically used in the  $\pi^0$  pole diagram but not elsewhere; other isospin-breaking effects are neglected. The second-order LECs are less well known. They have been determined by fits to both  $\pi N$  and  $NN$  scattering (since two-pion exchange is a significant part of the  $NN$  force); we take the values of Bernard [163]  $c_1 = -0.9_{-0.5}^{+0.2}$ ,  $c_2 = 3.3 \pm 0.2$ ,  $c_3 = -4.7_{-1.0}^{+1.2}$ , all in  $\text{GeV}^{-1}$ .

### 4.2.3 Born terms

We now discuss the  $\text{HB}\chi\text{PT}$  nucleon Compton amplitude in  $\chi\text{PT}$ . First, we focus on the Born terms. The low-energy theorems of Compton scattering provide a simple example of how the same physics plays out in the Dirac and heavy-baryon pictures; we refer to Eqs. (2.3) and (2.5). In the Dirac picture, the Born (non-structure) terms come from the two diagrams with an intermediate nucleon, with direct and crossed photons (Fig. 4.2(a)). If the resulting amplitude is expanded in powers of  $1/M_N$ , the Thomson term is reproduced in the amplitude  $A_1$ ; at one order higher, when the anomalous magnetic moment is included in the photon coupling, the Born terms in  $A_{3-6}$  appear.

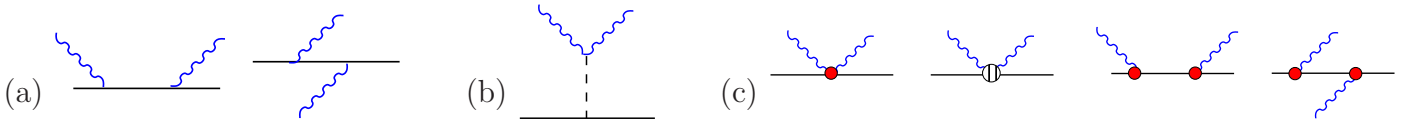


Figure 4.2: (Colour online) (a) Nucleon Born diagrams for Dirac nucleons; (b) Pion Born diagram; (c) Born diagrams in  $\text{HB}\chi\text{PT}$  up to  $\mathcal{O}(P^3)$ : solid (red) dots indicate vertices from  $\mathcal{L}_{\pi N}^{(2)}$  and open sliced dots from  $\mathcal{L}_{\pi N}^{(3)}$ . In the counting schemes to be introduced in Sections 4.2.6 and 4.2.7, the first diagram of (c) counts as  $\epsilon^2$  and  $e^2$ , and (b) and the rest of (c) count as  $\epsilon^3$  and  $e^2\delta^2$ .

In  $\text{HB}\chi\text{PT}$ , however, the leading (electric) photon-nucleon coupling is sufficiently simple that the direct and crossed diagrams just cancel. Indeed, for real photons it is possible to work in a gauge in which this vertex is actually absent (transverse or radiation gauge, corresponding to a purely space-like photon polarisation vector  $\vec{k} \cdot \vec{\epsilon} = 0$  in the nucleon's rest frame). The  $\text{HB}\chi\text{PT}$  diagrams which do contribute to the Born terms of Eq. (2.5) up to  $\mathcal{O}(P^3)$  are shown in Fig. 4.2(c). In transverse gauge, the leading  $\gamma NN$  vertex comes from  $\mathcal{L}_{\pi N}^{(2)}$  and includes a magnetic coupling proportional to the sum of the Dirac and anomalous magnetic moments. Thus, the two right-most diagrams in Fig. 4.2(c) give a third-order contribution proportional to  $1/M_N^2$ , accounting for the  $(Q + \kappa)^2$  Born terms in  $A_3$  to  $A_5$  and also for the Born term in  $A_6$ . However, the missing terms in  $A_1$  and  $A_3$  come from photon-nucleon seagulls at second and third order, respectively. In particular, the Thomson term comes from gauging the leading kinetic term in the Lagrangian; as discussed above, it counts as second order even though it has no powers of chiral momenta because it is proportional to  $\alpha_{\text{EM}}$ . This demonstrates that the distinction between Born and non-Born in  $\text{HB}\chi\text{PT}$  cannot be equated with (apparent) one-particle reducibility or the lack thereof. It is always safest to define Born terms via Dirac nucleons.

Of course, strictly speaking, in all these Born diagrams, it is the chiral-limit magnetic moment,  $\kappa^{(0)}$ , which appears, not the experimental value. The difference between  $\kappa$  and  $\kappa^{(0)}$  is  $\mathcal{O}(m_\pi)$ , and so this affects the amplitude only at fourth order. This issue will, however, recur below. The  $\pi^0$ -pole diagram Fig. 4.2(b) also contributes to amplitudes  $A_3$  to  $A_6$  at third order; its contribution is denoted by  $A_i^{\pi^0}$  in Eq. (2.6).

#### 4.2.4 Leading-order structure contributions and polarisabilities

It is gratifying that the basic low-energy theorems of Eq. (2.3) are reproduced in this EFT, but our interest is in the predictions made by the theory for the structure-dependent amplitudes, including the static polarisabilities  $\alpha_{E1}$ ,  $\beta_{M1}$  and the  $\gamma$ 's. As just described, the leading-order HB $\chi$ PT Compton-scattering amplitude is simply the Thomson term. At NLO— $\mathcal{O}(P^3)$ —there are the spin-dependent Born contributions described above, but there are also contributions from pion loops [182], specifically the diagrams depicted in Fig. 4.3. Individually these diagrams are divergent and violate the LETs, but

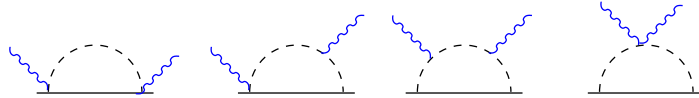


Figure 4.3: (Colour online)  $\mathcal{O}(P^3)$  loop diagrams in HB $\chi$ PT; all orderings of vertices and crossed as well as direct photons are implied. Vertices (shown without dots) are all from the LO Lagrangian, that is,  $\mathcal{L}_{\pi N}^{(1)}$  for the nucleonic coupling and  $\mathcal{L}_{\pi}^{(2)}$  for the  $\gamma\pi$  couplings. These also count as  $\epsilon^3$  and  $e^2\delta^2$ .

the sum is finite and leaves the Born contributions intact. Thus the sum of the loop diagrams contributes only to the structure parts of the six amplitudes and hence vanishes quadratically for  $A_1$  and  $A_2$  as  $\omega \rightarrow 0$  and as the third power of  $\omega$  for  $A_{3-6}$ . The coefficients of these terms are the polarisabilities, and at this order they are the same for both the proton and neutron. The results, first calculated by Bernard et al. [98, 182], are

$$\alpha_{E1} = 10\beta_{M1} = \frac{10\alpha_{\text{EM}}g_A^2}{192\pi m_\pi f_\pi^2} = 12.5 \quad , \quad \gamma_{E1E1} = 5\gamma_{M1M1} = -5\gamma_{M1E2} = -5\gamma_{E1M2} = -\frac{5\alpha_{\text{EM}}g_A^2}{96\pi^2 m_\pi^2 f_\pi^2} = -5.6. \quad (4.13)$$

It should be stressed that up to third order the full amplitudes, as well as the polarisabilities, are entirely predicted in terms of the well-known quantities  $m_\pi$ ,  $f_\pi$  and  $g_A$ ; there are no free parameters. Of course, the best method to analyse experiments for extracting even  $\alpha_{E1}$  and  $\beta_{M1}$  is the subject of this review, but nonetheless, the many attempts made in the past to measure these quantities all come out close to these values for both the proton and neutron; in particular, the order-of-magnitude difference between  $\alpha_{E1}$  and  $\beta_{M1}$  and their nearly isoscalar nature is not easily understood in most models. This has long been lauded as a stunning early success of HB $\chi$ PT. (As the spin polarisabilities are less well known, it is harder to judge these predictions; see Section 4.3.)

There are a number of caveats, however. Even strictly within HB $\chi$ PT, one would expect higher-order corrections to be of order  $P/\Lambda_\chi$ —around 20% if the scale of the expansion were  $\Lambda_\chi \sim m_\rho$ . There is also good reason to expect that for  $\beta_{M1}$  (as well as  $\gamma_{M1M1}$ ), the scale is actually set by the much smaller  $\Delta$ -nucleon mass difference  $M_\Delta - M_N$ . Furthermore, in a relativistic framework, the predictions from the diagrams in Fig. 4.3 are substantially smaller:  $\alpha_{E1}^{(p)} = 6.8$ ,  $\beta_{M1}^{(p)} = -1.8$  [183, 184]. But, before dismissing the success of third-order HB $\chi$ PT as a fluke, we should step back and remember that the calculation gives us full amplitudes as a function of  $\omega$ , not merely the static polarisabilities. As will be shown in more detail subsequently, the full third-order cross section extends the region in which data can be well described substantially beyond that where the Petrun'kin cross section (Born plus static scalar polarisabilities) is valid. In particular, it reproduces the pronounced cusp at the photopion threshold which is seen at forward scattering angles (see Fig. 3.1). Beyond that point, the data show a huge rise in the cross section which is obviously due to the  $\Delta(1232)$  (see Fig. 3.2), and one could not expect a theory without the  $\Delta(1232)$  to work in that region.

For completeness, we should mention that a handful of calculations of polarisabilities have been done in the framework of  $SU(3)\times SU(3)$  chiral perturbation theory, involving kaons as well as pions and

all the octet baryons. Bernard et al. calculated the spin-independent static polarisabilities in HB $\chi$ PT [185] and showed that for nucleons the effect of kaon loops was small (see also Butler and Savage [186]); Vijaya Kumar et al. found a similar result for  $\gamma_0$  [187]. Dynamical polarisabilities  $\alpha_{E1}(\omega)$  and  $\beta_{M1}(\omega)$  have also been calculated at NLO in a covariant framework by Aleksejevs and Barkanova [188].

#### 4.2.5 Structure beyond leading order

Although the ability of third-order HB $\chi$ PT to qualitatively describe low-energy data is encouraging, the lack of any free parameters limits its use as a tool to extract more information from those data. This situation changes at fourth order, because at that order we can construct Lagrangian terms like  $\psi^\dagger F^{\mu\nu} F_{\mu\nu} \psi$  which are multiplied by new, undetermined LECs. Such terms give rise to photon-nucleon seagull diagrams which contribute terms proportional to  $\omega^2$  to the amplitudes  $A_1$  and  $A_2$  [189]. In the enumeration of Ref. [181], there are actually six such terms (numbers 89-94) but in the photon-nucleon sector only four independent combinations of LECs enter, which we can call  $\delta\alpha_{E1}^{(p)}$ ,  $\delta\alpha_{E1}^{(n)}$ ,  $\delta\beta_{M1}^{(p)}$  and  $\delta\beta_{M1}^{(n)}$  (see  $\mathcal{L}_{\pi N}^{(4)}$ , Eq. (4.11), and Fig. 4.4). These are contributions to the spin-independent polarisabilities of the proton and neutron which come from non-chiral physics—for example, quark substructure, or resonances, according to perspective, and they obviously encode the leading effects of a  $\Delta(1232)$  pole. In addition, at fourth order a new set of  $\pi N$  diagrams has to be included. Finally, all the N<sup>2</sup>LO terms in the expansion of the relativistic Born contributions to  $A_1$  and  $A_2$  are also generated via fourth-order seagulls and diagrams like those of Fig. 4.4 with either one vertex taken from  $\mathcal{L}_{\pi N}^{(2)}$  or with an NLO nucleon propagator.

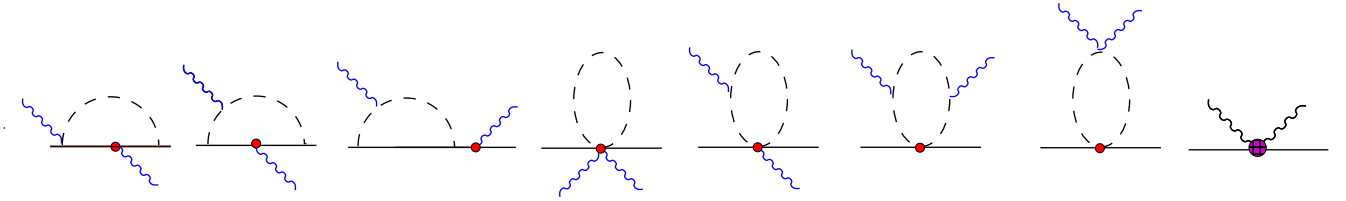


Figure 4.4: (Colour online)  $\mathcal{O}(P^4)$  diagrams in HB $\chi$ PT; vertices labelled as in Figs 4.2 and 4.3 with the addition of a (magenta) doted dot for the fourth-order counterterms  $\delta\alpha_{E1}^{(p)}$  etc. of  $\mathcal{L}_{\pi N}^{(4)}$ . All orderings of vertices and crossed as well as direct photons are implied. Omitted are all diagrams obtained from those in Fig. 4.3 by substituting an NLO vertex or propagator for an LO one. These also count as  $\epsilon^4$  and  $e^2\delta^4$ , though the final diagram is included at one order lower if polarisabilities are fit.

Of the loop diagrams, many are  $1/M_N$  corrections to the diagrams of Fig. 4.3 (no new LECs enter in these). However, there are also two new types of diagrams—those with magnetic-moment couplings as well as a pion loop, and those with a pion-nucleon seagull, as shown in Fig. 4.4. In the former, the only new LECs are the well-known proton and neutron anomalous magnetic moments. In the latter, however, the three  $\pi N$  LECs  $c_1$ ,  $c_2$  and  $c_3$  enter.

This time, the sum of all loop diagrams does make a  $\mathcal{O}(\omega)$  contribution to the Born terms. The contributions are exactly those which are needed to replace the chiral-limit  $\kappa^{(0)}$  with the correction that shifts  $\kappa$  to its experimental value at this order. In the expansion of the  $\gamma N$  vertex, this shift comes from a diagram in which the photon couples to a pion loop, as in the third diagram of Fig. 4.4, but in Compton scattering this is not the only diagram which gives  $\delta\kappa$  corrections to the Born term, nor is such a correction the only contribution from this diagram [190–192]. The  $\mathcal{O}(\omega^2)$  piece of the sum of all fourth-order loop diagrams produces a logarithmically divergent result for the spin-independent polarisabilities. These divergences are cancelled by the divergent parts of  $\delta\alpha_{E1}^{(p)}$  etc. to leave a finite but undetermined total fourth-order contribution to the spin-independent polarisabilities [189]. By contrast, the  $\mathcal{O}(\omega^3)$

parts of all these loop diagrams yield a finite shift for the spin polarisabilities [190–194]; in particular the contribution of the one-nucleon-reducible diagrams in Fig. 4.4 may not be omitted [194, 195].

There are actually a number of subtleties in the fourth-order calculation which are not present at third order, one of which is the frame dependence. Since the kinetic energy  $p^2/(2M_N)$  of a nucleon is one chiral order higher than that of a photon (which is the same as its three momentum and assumed to be of order  $m_\pi$ ), at lowest order the incoming and outgoing photon momenta are the same, and the same in any frame in which the heavy-baryon reduction is valid. That includes the lab, Breit and centre-of-mass (cm) frames. Thus, in the lowest-order ( $\mathcal{O}(P^3)$ ) loop calculation, we do not need to specify in which frame we are working. At  $\mathcal{O}(P^4)$ , however, that is no longer the case. The Breit frame is the simplest in which to calculate and has the additional merit over the commonly used cm frame that the amplitudes are crossing-symmetric. (Already at third order the cm frame violates this: the Born terms, but not the loops, are different in the two frames.) Furthermore, in identifying the terms  $\alpha_{E1}^{(p)}\omega^2$  etc. in the amplitudes, it is desirable that this is as close as possible to what is used in other determinations of the polarisabilities. In the Petrun’kin cross section, it is  $\omega_{\text{lab}}\omega'_{\text{lab}}$  which multiplies the polarisabilities; in DR analyses, it is  $\nu^2$ . These differ from one another and from  $\omega_{\text{Breit}}^2$  by terms of order  $\omega^2/M_N^2$  (which matters only at  $\mathcal{O}(P^5)$ ), whereas  $\omega_{\text{cm}}^2$  differs at  $\mathcal{O}(\omega/M_N)$ . Having obtained the Breit-frame amplitudes, those in other frames can be obtained from a boost, expanded to the appropriate order in  $1/M_N$ . Whereas at  $\mathcal{O}(P^3)$  the cross section differs noticeably depending on which frame is chosen, at  $\mathcal{O}(P^4)$  this dependence is negligible. (This frame dependence at  $\mathcal{O}(P^3)$  can be confusing, given the lack of frame dependence in the *form* of the amplitudes. But the variables in the two frames,  $(\omega_{\text{cm}}, \theta_{\text{cm}})$  and  $(\omega_{\text{Breit}}, \theta_{\text{Breit}})$ , are *not* the same as functions of the lab variables, see Section 2.3.)

A more physical issue than the choice of frame, passed over in the discussion of third order above, is the fact that any amplitude calculated to finite order will put the photoproduction threshold at  $\omega = m_\pi$  (irrespective of the frame in which  $\omega$  is defined). This is because the incoming nucleon kinetic energy is included perturbatively and is not present in the nucleon propagator in the  $\pi N$  loop. Of course, within the heavy-baryon amplitude there will be a string of terms which would be generated by the  $1/M_N$  expansion of a loop in which the nucleon is allowed to recoil, and, as noted by Bernard et al. [196], the solution is to resum these terms to put the threshold at the correct place. In practice, that involves replacing  $\omega$  within loop integrals by a new variable  $\omega_s(\omega)$ , which differs from  $\omega$  by terms of  $\mathcal{O}(\omega/M_N)$  and which equals  $m_\pi$  when  $\omega = \omega_{\text{th}}$ , and then writing a Taylor expansion in powers of  $\omega_s/M_N$  and retaining only those terms required at the order to which one is working. At third order, no expansion is required, and there is simply a substitution of variable; that has always been done before comparison with experiment. At fourth order, the third-order loop pieces do need to be expanded, and indeed only with such a prescription are the amplitudes finite at threshold [196].  $\omega_s$  is not uniquely determined by this prescription, but it is commonly taken to be  $\omega_s = \sqrt{s} - M_N$ . A different choice was made in Refs. [196–199].

In Ref. [197], McGovern took the values of  $\alpha_{E1}^{(p)}$  and  $\beta_{M1}^{(p)}$  from the Particle Data Group (which were very close to the third-order values) and made a comparison with all extant data below 180 MeV. The resulting conclusion was that there was a modest improvement over the third order up to around the photoproduction threshold, but no improvement beyond that point, with particularly poor agreement at backward angles. Of course, there is still no  $\Delta(1232)$ , but the tadpole diagrams of Fig. 4.4 would be obtained from a theory in which an explicit  $\Delta(1232)$  had been integrated out to leave the pion seagull terms proportional to the LECs  $c_2$  and  $c_3$ , so it was somewhat surprising that they did not extend the fit a little further. Of course, the biggest contribution from an explicit  $\Delta(1232)$  would be the pole diagram, and it is clear from comparison to the data that by 200 MeV, replacing this with one term of a polynomial expansion ( $\delta\beta_{M1}^{(p)}\omega^2$  etc.) is quite inadequate (see Fig. 4.6). In Ref. [198, 199], Beane et al. instead fitted  $\alpha_{E1}^{(p)}$  and  $\beta_{M1}^{(p)}$  to the data in the same region (with a cut on  $|t|$  as well as  $\omega$ ). As will be discussed in Section 4.4, there are problems with the data set which precluded a fit with an



acceptable  $\chi^2$ . Nevertheless, a fairly robust conclusion emerged in which a higher value of  $\beta_{M1}^{(p)}$  than that generally accepted was required by the data—the central value quoted was 3.4. If the Baldin sum rule was imposed, this value was decreased to 2.8 (see Table 4.2 in Section 4.3 for detailed results).

#### 4.2.6 Including the $\Delta(1232)$ in the small-scale expansion

The  $\Delta(1232)$  resonance has long been recognised as hugely important in the physics of nucleons. In  $\chi$ PT it is not explicitly present, but its influence is felt through LECs such as  $c_{2,3}$  and  $\delta\beta_{M1}^{(p)}$ . But, as the radius of convergence of an EFT is set by the scale of the lowest degree of freedom which has not been included, the  $\Delta(1232)$  can be expected to severely restrict the applicability of  $\chi$ PT at least in those processes in which it contributes, with the convergence governed by the scale  $\Delta_M \equiv M_\Delta - M_N$ . And any glance at Compton-scattering data above 200 MeV, as in Fig. 3.2, confirms that this is such a process.

In fact, since  $\Delta_M \approx 2m_\pi$ , it could be argued that these two scales are similar and should be included on the same footing. This is the basis of the so-called “small-scale” or “ $\epsilon$ ” expansion developed by Hemmert et al. [200, 201] (see also the earlier work of Butler et al. [186, 202]). Explicit  $\Delta(1232)$  fields are included in the Lagrangian, as first shown by Manohar and Jenkins [175], and  $\Delta_M/\Lambda_\chi$  is counted like  $p_{\text{typ}}/\Lambda_\chi$  and  $m_\pi/\Lambda_\chi$  in determining the order of a diagram. The heavy-baryon expansion is used, ensuring that only  $\Delta_M$  and not  $M_\Delta$  appears.

The relevant terms in the Lagrangian are the following:

$$\mathcal{L}_\Delta^{(1)} = (\Delta_\nu^i)^\dagger (-i\nu \cdot D + \Delta_M) \Delta^{i\nu} \quad (4.14)$$

$$\mathcal{L}_{\pi N \Delta}^{(1)} = -\frac{g_{\pi N \Delta}}{f_\pi} (\psi^\dagger \partial^\nu \phi^i \Delta_\nu^i + (\Delta_\nu^i)^\dagger \partial^\nu \phi^i \psi + \dots) \quad (4.15)$$

$$\mathcal{L}_{\gamma N \Delta}^{(2)} = \frac{-ieb_1}{M_N} \left( \psi^\dagger S_\rho F^{\mu\rho} \Delta_\mu^3 - (\Delta_\mu^3)^\dagger S_\rho F^{\mu\rho} \psi \right) \quad (4.16)$$

where  $\Delta_\nu^i$  is the heavy-baryon reduction of an  $I = \frac{3}{2}$ ,  $S = \frac{3}{2}$  Rarita-Schwinger field  $\Psi_\nu^i$ , with  $i$  and  $\mu$  being the indices on the (iso)spin-1 vector coupled to the (iso)spin- $\frac{1}{2}$  spinor. The coupling constant  $g_{\pi N \Delta}$  is fit to the  $\Delta(1232)$  width and varies significantly depending on whether relativistic or non-relativistic kinematics are used. The transition magnetic moment  $b_1$  also has no single widely accepted value. Both will be specified when we use them later.<sup>8</sup> It is also worth displaying here the alternative form of  $\mathcal{L}_{\gamma N \Delta}^{(2+3)}$  used in the  $\delta$  expansion, see later (here  $\psi$  is the nucleon Dirac spinor and other notation is that of Ref. [205]):

$$\mathcal{L} = \frac{3e}{2M_N(M_N + M_\Delta)} \left( \bar{\psi} (ig_M \tilde{F}^{\mu\nu} - g_E \gamma_5 F^{\mu\nu}) \partial_\mu \Psi_\nu^3 - \bar{\Psi}_\nu^3 \overleftarrow{\partial}_\mu (ig_M \tilde{F}^{\mu\nu} - g_E \gamma_5 F^{\mu\nu}) \psi \right) . \quad (4.17)$$

The leading (magnetic) term in the heavy-baryon reduction of this Lagrangian is equivalent to the one above with the identification

$$g_M = b_1(1 + M_\Delta/M_N)/3 \quad (4.18)$$

(though it is important to note that if the full vertex is used, there are substantial sub-leading terms), but there is also a sub-leading electric coupling  $g_E$ . The ratio of these two couplings (at the  $\Delta(1232)$  pole) can be obtained from the E2/M1 ratio to be  $-0.34$  [206, 207]. Being third order, the electric contribution to the amplitudes is suppressed by a power of  $\omega/M_N$  relative to the magnetic one. In the following, we will sometimes use  $b_2$  for the electric coupling, defined via  $g_E = b_2(1 + M_\Delta/M_N)/3$ .

<sup>8</sup>There is some confusion in the literature by what is meant by the magnetic coupling  $b_1$ . The early papers of Hemmert, Holstein et al. [200, 201, 203, 204] were not always consistent with one another and did not always specify which Lagrangian was being used, so that signs and factors of 2 come and go. Although it is not stated in the paper, Hildebrandt et al. [92] use the Lagrangian displayed above, which gives a contribution to  $\beta_{M1}$  of  $2\alpha_{\text{EM}} b_1^2 / (9\Delta_M M_N^2)$ .

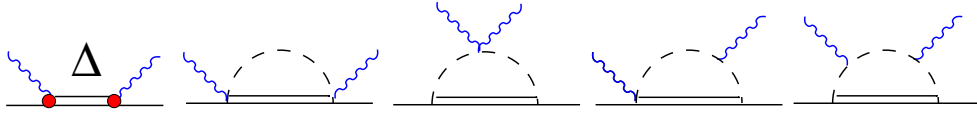


Figure 4.5: (Colour online)  $\Delta(1232)$  contributions to Compton scattering at  $\epsilon^3$  and  $e^2\delta^3$  (see text for explanation). All orderings of vertices and crossed as well as direct photons are implied.

In the small-scale expansion,  $\Delta(1232)$  propagators  $(v \cdot p - \Delta_M + i\eta)^{-1} \sim \epsilon^{-1} \sim m_\pi^{-1}$  have the same counting as nucleon ones  $(v \cdot p + i\eta)^{-1}$ , and so the diagrams of Fig. 4.5 are also third order (denoted now  $\mathcal{O}(\epsilon^3)$  rather than  $\mathcal{O}(P^3)$ ). Those vertices of the theory without external  $\Delta$ s are unchanged, except that the LECs  $c_2$  and  $c_3$  need to be retuned to exclude the  $\Delta(1232)$  contribution; this is done by subtracting the  $\Delta$ -pole contribution to soft  $\pi N$  scattering. There are significant complications in including spin- $\frac{3}{2}$  fields, not least of which is the need to ensure that unphysical spin- $\frac{1}{2}$  degrees of freedom do not propagate, but at leading order this is not an issue. The contribution of the  $\Delta(1232)$  to the polarisabilities in this framework was calculated in Refs. [203, 204] (see also [186, 202]) and to the full Compton amplitudes in Refs. [90, 92, 203]. Of course, these are dependent on new and rather poorly known coupling constants, namely the  $\pi N \Delta$  coupling constant and the  $\gamma N \Delta$  transition magnetic moment.

Long before Hemmert's work, though, it was known that the  $\Delta$ -pole diagrams give a huge paramagnetic (isoscalar) contribution to  $\beta_{M1}$ . The exact value depends on the parameter values, but Mukhopadhyay et al. estimated  $\delta\beta_{M1}^\Delta = 7.0$  [208], and Hemmert et al. obtained values of 7.2–12 [203, 204]. In the latter work and in Ref. [186], it was also shown that the  $\pi\Delta$  loop diagrams made a substantial contribution to  $\alpha_{E1}$ . With no counterterm to adjust at third order, there was no possibility of agreement with data. The pragmatic solution, adopted by Hildebrandt et al. in Refs. [14, 90, 92], was to promote the fourth-order isoscalar counterterms  $\delta\alpha_{E1}$  and  $\delta\beta_{M1}$  to third order, so that these unwanted large contributions to the polarisabilities could be cancelled. The prediction for the rest of the amplitudes remained intact, of course.

In these works, the third-order theory with an explicit  $\Delta(1232)$  was fit to the Olmos de León and Hallin data up to 240 MeV ( $\omega_{\text{cm}} = 200$  MeV). In view of the uncertainty in the  $\Delta$ -sector parameters in this formulation, the transition magnetic-moment strength  $b_1$  was also fit along with  $\alpha_{E1}$  and  $\beta_{M1}$ . ( $\Delta_M = 271.3$  MeV was fit to the real part of the  $\Delta$  pole position, and  $g_{\pi N \Delta} = 1.12$  to the imaginary part using the non-relativistic formula for the width.) A good description of the data was obtained. The value of  $b_1 = 4.7$  may seem high compared to the value of 3.7 obtained from a recent fit to photoproduction data [206, 207], but since the latter used the Lagrangian of Eq. (4.17), no direct comparison can be made. As expected, the problem at backward angles that was evident without the  $\Delta(1232)$  was cured and no restriction on  $|t|$  was required. Perhaps surprisingly, the values of  $\alpha_{E1}$  and  $\beta_{M1}$  obtained were close to those of Beane et al., although with less tension with the Baldin sum rule. The value of  $\beta_{M1}^{(p)} = 3.4$ , in particular, is again higher than the traditional value and appears to be a feature of chiral EFT fits. It should be noted that though the theory now includes the  $\Delta(1232)$ , its reach is still limited to  $\omega_{\text{lab}} \lesssim 240$  MeV, since the power counting suppresses the loop diagrams which need to be resummed to give the  $\Delta$  a width, and so the amplitudes diverge as  $\omega \rightarrow \Delta_M$ .

#### 4.2.7 The $\delta$ expansion

As important as the  $\Delta(1232)$  is above the photoproduction threshold, its influence on the cross section diminishes rapidly as the energy is reduced. Arguably, with the particular values of  $\Delta_M (= M_\Delta - M_N)$  and  $m_\pi$  obtaining in the real world, counting the two as the same scale gives undue prominence to the  $\Delta(1232)$  in the region where static polarisabilities are important. An alternative counting was proposed by Pascalutsa and Phillips [205] in which  $m_\pi/\Delta_M$  and  $\Delta_M/\Lambda_\chi$  are counted as proportional to the same

expansion parameter  $\delta$  (the so-called “ $\delta$  expansion”). In this counting, the  $\Delta$ -less theory is an expansion in powers of  $\delta^2$ , and, for low energies, the first contributions from the  $\Delta$  (the pole diagrams and the  $\pi\Delta$  loops) intercalate between the third and fourth orders of  $\chi$ PT. The main advantage of this expansion, however, is that it allows for two separate energy regions,  $\omega \sim m_\pi$  and  $\omega \sim \Delta_M$ , and, in the latter regime, there is no suppression of  $\pi N$  loop contributions to the  $\Delta$  propagator. Thus, these must be resummed, and the  $\Delta$  becomes an unstable particle with a width  $\Gamma$ , with the new propagator going as  $(\not{p} - M_\Delta + i\Gamma(p^2)/2)^{-1}$ . For  $\omega \sim \Delta_M$ , the one- $\Delta$  reducible diagram dominates (that is, the direct  $\Delta$ -pole diagram), with all other contributions being sub-leading. In order to have amplitudes which could be used over the entire energy region, Pascalutsa and Phillips added just the resummed, direct  $\Delta$ -pole diagram to the standard third-order  $\chi$ PT amplitudes. This includes all contributions to  $\mathcal{O}(e^2\delta^2)$  in each region, at the expense of having an incomplete set of higher-order contributions in each.<sup>9</sup> This meant that the sub-leading electric  $\gamma N\Delta$  coupling was also included. (Two further technical details relevant to Ref. [205] are that: (a) the  $\Delta$  Lagrangian used was one developed by Pascalutsa [209, 210] which ensures freedom from spin- $\frac{1}{2}$  degrees of freedom via the imposition of an extra local gauge symmetry; and (b) the direct  $\Delta$ -pole contribution was included with relativistic kinematics and the full Dirac vertex rather than being expanded in powers of  $1/M_N$ .) Importantly, in this approach there is no promotion of the  $\delta\alpha_{E1}$  etc. terms of Eq. (4.11), and the polarisabilities are *predicted* in terms of the two  $\gamma N\Delta$  couplings  $g_M$  and  $g_E$ , which were fit to Compton data. Because  $\pi\Delta$  loops are absent,  $\alpha_{E1}$  is close to its HB $\chi$ PT value (there is a small negative contribution  $\propto g_E^2$ ). Since the  $u$ -channel  $\Delta$  diagram is missing and the magnetic coupling is somewhat smaller than previously assumed, the usual huge enhancement of  $\beta_{M1}$  is significantly reduced, and the net value is  $\beta_{M1}^{(p)} = 3.9$ . The fit in the low-energy region is not dissimilar to that of Hildebrandt, but a good description of the data is obtained even in the  $\Delta$ -resonance region. From the point of view of deducing  $\alpha_{E1}$  and  $\beta_{M1}$  from the low-energy data, the main message again is that a good description is obtained with a larger value of  $\beta_{M1}$  than the previously accepted one. Unfortunately, the amplitude used by Pascalutsa and Phillips for  $\pi N$  loops in this work did not have the correct analytical continuation above the  $\pi N$  threshold, thereby rendering both the real and imaginary parts of those loops incorrect. The description of data between  $\omega_{\text{lab}} \approx 150$  MeV and the  $\Delta(1232)$  peak published in Ref. [205] is influenced by these loops, and thus cannot be regarded as definitive. This may also account for their finding that the best results were obtained with a value of  $g_E \sim -2.3g_M$  which is much larger than that usually deduced from the E2/M1 ratio.<sup>10</sup>

More recently, Lensky and Pascalutsa [184, 211] extended the previous calculation to include all contributions that enter at  $\mathcal{O}(e^2\delta^3)$ , which includes both  $s$ - and  $u$ -channel  $\Delta$ -pole diagrams, as well as  $\pi\Delta$  loops. However, unlike previous work on Compton scattering in EFT, they did not use the heavy-baryon framework, but worked in terms of Dirac nucleons. It is beyond the scope of this review to detail modern developments in baryon  $\chi$ PT; these avoid expanding the Lagrangian in powers of  $1/M_N$ , while ensuring that positive powers of  $M_N$  which would spoil the power counting do not enter (see Bernard [163] for a summary). The various schemes in use all yield results which have several features in common: they aim at a Lorentz-covariant amplitude; when expanded in powers of  $1/M_N$ , they agree with one another and with HB $\chi$ PT up to the order of validity of the calculation; they also agree for any term which is non-analytic in  $m_\pi^2$ ; but they may differ with regard to effects that are higher-order in  $1/M_N$ . Ultimately, of course, LECs (which are different in the different schemes) will absorb these differences. For low-order calculations, however, the difference between schemes can produce significant effects in observables. The calculations of Refs. [184, 211] were performed in one such version of Baryon  $\chi$ PT.

<sup>9</sup>In the literature on  $\delta$  counting, contrary to common usage in  $\chi$ PT, a factor of  $e^2$  is pulled out before the counting starts, so  $\mathcal{O}(e^2\delta^2) \sim \mathcal{O}(P^3)$ .

<sup>10</sup>Note also the following misprints in that paper: in the expression for the  $\Delta$  width in Eq. (42),  $s + M_N^2 - m_\pi^2$  should be replaced by  $((\sqrt{s} + M_N)^2 - m_\pi^2)/2$ ; Eq. (51) should contain  $\mathcal{O}_5^{\mu\nu} = q^\mu q'_\alpha \gamma^{\alpha\nu} + \gamma^{\mu\alpha} q_\alpha q'^\nu$ ,  $\mathcal{O}_6^{\mu\nu} = q^\mu q_\alpha \gamma^{\alpha\nu} + \gamma^{\mu\alpha} q'_\alpha q'^\nu$  and  $\mathcal{O}_8^{\mu\nu} = i\epsilon^{\mu\nu\alpha\beta} q_\alpha q'_\beta$ . Eq. (54) should have  $-\mathcal{O}_7$  on the left-hand side. The unwritten convention is  $\epsilon_{0123} = 1$  so the penultimate equation of footnote (2) should be  $\gamma^{\mu\nu\alpha} = -i\epsilon^{\mu\nu\alpha\beta} \gamma_\beta \gamma_5$ .

Although the nucleons obey relativistic kinematics, antinucleons are not—and should not be—included in the effective theory.

While some of the  $1/M_N$  terms which are automatically included in the covariant case produce effects relevant to low-energy dynamics, e.g. terms which must be resummed to put the threshold in the right place in the HB $\chi$ PT approach, others act as a regulator on loop integrals. They therefore have no meaning when separated from the higher-order LECs, except perhaps as an estimate of the likely size of uncertainties due to omitted higher-order physics. Nevertheless, the polarisabilities constitute one case in which such higher-order effects make a sizable difference in a low-order calculation. The covariant B $\chi$ PT diagrams to be evaluated at third order include all those in Fig. 4.3, as well as those from Fig. 4.4 where the  $\gamma$ NN vertex is generated by the  $1/M_N$  expansion of the relativistic Lagrangian. An example is the Dirac magnetic moment of the Lagrangian; diagrams where both photons couple to a nucleon line also enter the relativistic calculation of polarisabilities at LO. The integrals differ from the HB $\chi$ PT case in that they depended on the nucleon mass as well as on the pion mass, and the net effect of the sub-leading  $m_\pi/M_N$  terms is to substantially reduce  $\alpha_{E1}$  and  $\beta_{M1}$ . Once the  $\Delta(1232)$  is added in (with the parameters of Ref. [184, 211], which are taken from photoproduction studies), we return to familiar values of  $\alpha_{E1} = 10.8$  and  $\beta_{M1} = 4.0$ —but the difference from the fourth-order HB $\chi$ PT case is that these are predictions rather than fits. Since this calculation includes all the dynamics relevant for  $\omega_{\text{lab}} \leq 170$  MeV, it is not surprising that the data description in this domain is good (see Fig. 4.6).

	$\pi$ N loops	$\Delta$ pole	$\pi\Delta$ loops	Higher resonances, $\sigma$ pole
$\mathcal{O}(P^3)$	LO	$\times$	$\times$	$\times$
$\mathcal{O}(\epsilon^3)$	LO	$s$ - and $u$ -channel	$\checkmark$	$\times$
$\mathcal{O}(\epsilon^3)$ (mod.) [14]	LO	$s$ - and $u$ -channel	$\checkmark$	In 2 CTs
$\mathcal{O}(P^4)$ [199]	NLO	In 2 CTs	In 2 CTs	In 2 CTs
$\mathcal{O}(e^2\delta^{2+})$ [205]	LO	$s$ -channel, width, M1+ E2	$\times$	$\times$
$\mathcal{O}(e^2\delta^{3+})$ [184]	LO + pNLO	$s$ - and $u$ -channel, width, M1 + E2	$\checkmark$	$\times$

Table 4.1: Comparison of the different mechanisms included in different EFT variants. All calculations include the nucleon Born and pion-pole term.  $\mathcal{O}(X^n+)$  indicates some contributions beyond the stated order; pNLO indicates some effects which would be NLO in HB $\chi$ PT. CT denotes the  $\gamma$ N contact interactions of Eq. (4.11); at  $\mathcal{O}(P^4)$  the  $\pi$ N contact interactions  $\propto c_i$  also encode resonance physics.

#### 4.2.8 EFT fits in relation to the data

At this point, it will be useful to summarise the different counting schemes in use. In HB $\chi$ PT without the  $\Delta(1232)$ , the counting is the usual one, in powers of  $P/\Lambda_\chi$  with as  $P$  the pion mass, a typical momentum or the photon energy. For the multipoles to which the  $\Delta$  is known to contribute, though,  $\Lambda_\chi \sim M_\rho$  is replaced by  $\Delta_M (= M_\Delta - M_N)$ . The lowest-order contribution to Compton scattering is the Thomson term which is  $\mathcal{O}(P^2)$  (since  $|e| \sim P/\Lambda_\chi$ ). When the  $\Delta$  is included in the small-scale expansion [200, 201], we treat  $\Delta_M \sim P$  and call the expansion parameter  $\epsilon \equiv (\Delta_M, P)/\Lambda_\chi$ . In the low-energy regime, both  $\Delta$  and nucleon propagators scale as  $\epsilon^{-1}$  and so  $\pi\Delta$  loops and  $\Delta$ -pole diagrams enter at  $\mathcal{O}(\epsilon^3)$  along with the corresponding nucleon diagrams. Short-range contributions to  $\alpha_{E1}^{(p)}$  etc. only enter at fourth order, but have often been promoted to third order—partly to provide diamagnetic strength to counteract the  $\Delta$ ; we refer to this as modified  $\mathcal{O}(\epsilon^3)$ . In the region of the  $\Delta$  resonance, diagrams which give the  $\Delta$  a finite width must be included, but this has not been done in the  $\epsilon$  expansion. An

alternative counting is given by the  $\delta$  expansion [205], in which away from the resonance region  $\Delta$  propagators are suppressed relative to nucleon ones by one power of  $\delta \approx m_\pi/\Delta_M$ ; here the Thomson term is  $\mathcal{O}(e^2)$ , LO N-pole and  $\pi$ N are  $\mathcal{O}(e^2\delta^2)$ , LO  $\pi\Delta$  and  $\Delta$ -pole are  $\mathcal{O}(e^2\delta^3)$ , and NLO N-pole and  $\pi$ N diagrams are  $\mathcal{O}(e^2\delta^4)$  (see Figs. 4.2–4.4). The ingredients of several calculations that use different  $\chi$ EFT expansions are summarised in Table 4.1.

An important difference not noted in the table is that, in order to facilitate the treatment of the pole region where finite-width  $s$ -channel  $\Delta$ -pole diagrams are leading order, all work in the  $\delta$  expansion has used a relativistic form for the  $\Delta$  propagator with the  $\gamma$ N $\Delta$  vertex from Eq. (4.17), even for  $\omega \ll \Delta_M$ . At sufficiently low energies, the two magnetic  $\gamma$ N $\Delta$  coupling constants,  $b_1$  from Eq. (4.16) and  $g_M$  from Eq. (4.17), are related by Eq. (4.18), which translates  $g_M = 2.9$  [206, 207] to  $b_1 = 3.8$ ; with this identification, the two give exactly the same contribution to  $\beta_{M1}$ . However, the two vertices are not equivalent at higher energies. If the full  $\beta_{M1}$  is fit to data and hence does not directly depend on  $b_1$  ( $g_M$ ), significant  $\omega/M_N$  effects from Eq. (4.17) mean that a substantially higher value of  $b_1$  is required to give broadly the same cross section. Numerical studies show that values of  $g_M = 2.9$  and  $b_1 = 4.8$ – $5.0$  give similar cross sections up to 150 MeV, if the parameters and other ingredients of the modified  $\epsilon^3$  and modified  $e^2\delta^3$  are the same. (The closeness of the dynamical polarisabilities can be seen in Fig. 4.7.) Hildebrandt et al. [14, 90, 92] found that a slightly lower value of  $b_1 \approx 4.7$  gave the best results, but they use pole-position rather than  $\Delta$ -resonance parameters.

Figure 4.6 shows the results of the various calculations and fits described in the previous section; see Table 4.1 for ingredients and Table 4.2 for a summary of results for the static polarisabilities. In attempting to extract polarisabilities from the low- and possibly intermediate-energy data, there are competing pressures. On the one hand, EFTs are clearly most reliable at low energy. On the other hand, the effects of the polarisabilities grow with energy, and the more data that can be included in a fit, the better the resulting statistical errors are expected to be. Using HB $\chi$ PT to  $\mathcal{O}(P^4)$  but without the  $\Delta(1232)$ , Beane et al. applied a cut of 180 MeV in both  $\omega_{\text{lab}}$  and  $\sqrt{-t}$ , the latter meaning that the maximum energy was in fact only reached for angles up to  $60^\circ$ , dropping to 90 MeV at  $180^\circ$ . The resulting extraction was therefore free from any of the issues discussed above concerning the data at intermediate energies, but the statistical errors of  $\pm 1.1$  on  $\alpha_{E1}^{(p)}$  and  $\beta_{M1}^{(p)}$  compared unfavourably with those obtained, for instance, by Baranov et al. [212] using all data up to 150 MeV prior to Olmos de León ( $\pm 0.8$  on  $\alpha_{E1}^{(p)}$  and  $\pm 0.9$  on  $\beta_{M1}^{(p)}$ ). Hildebrandt et al. did include the  $\Delta$  in the small-scale expansion and fit to the Olmos de León and Hallin data up to 240 MeV. Without a finite width, their  $\Delta$ -pole amplitude starts to deviate from a Breit-Wigner-like shape which could continue into the resonance region above 200 MeV, more strongly at backward angles. Some of the nice agreement with the Hallin data in the intermediate-energy region shown in Hildebrandt’s thesis may therefore be fortuitous. The relatively high errors (of  $\pm 1.4$  on  $\alpha_{E1}^{(p)}$  and  $\beta_{M1}^{(p)}$ ) may be due to the fact that they did not allow the normalisation of the data sets to float or that they did not include the older data.

Pascalutsa and Phillips resum  $\Delta$  self-energy diagrams, however, generating a width and a Breit-Wigner-like propagator, and the resulting form gives at least a qualitatively good description of the data up to the pole region. All the ingredients for an extraction that also incorporates the effects of  $\pi$ N loops,  $\pi\Delta$  loops and the  $\Delta$ -pole diagrams—with a finite width where necessary—now exist. While Hildebrandt et al. could not access the resonance region and hence had to fit the crucial  $\gamma$ N $\Delta$  magnetic coupling constant to the low- and intermediate-energy data, in the  $\delta$  expansion it should be possible to fit purely  $\Delta$  parameters in the resonance region, leaving only  $\alpha_{E1}^{(p)}$  and  $\beta_{M1}^{(p)}$  to be fit to low-energy data. Such a strategy should also be able to bypass the problems of the intermediate region, although the issue of Blanpied (LEGS) versus Wolf (MAMI) cannot be avoided. Details of such a calculation will be presented in Section 4.4.



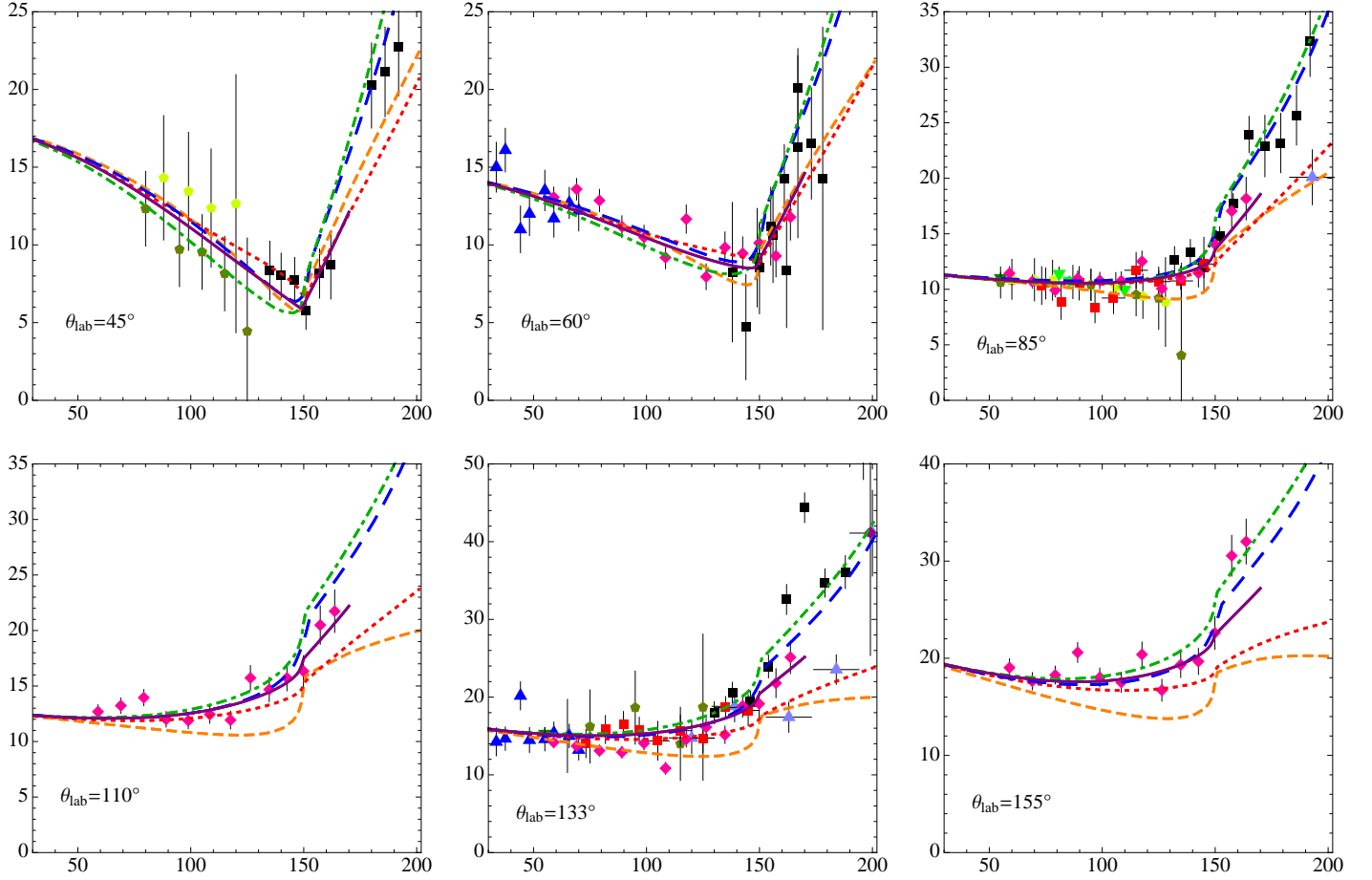


Figure 4.6: (Colour online) Previous results. Working from the lowest cross section up in the last frame, the lines are as follows: Medium dash (orange):  $\mathcal{O}(P^3)$  Babusci et al. [78]; short dash (red):  $\mathcal{O}(P^4)$  Beane et. al. [199]; solid (purple): partial  $\mathcal{O}(e^2\delta^3+)$  Lensky and Pascalutsa [184]; long dash (blue):  $\mathcal{O}(\epsilon^3)$  Hildebrandt et al. [14]; dash-dot (green):  $\mathcal{O}(e^2\delta^2+)$  Pascalutsa and Phillips. [205]. For Refs. [14, 199], the fits without imposition of the Baldin sum rule are shown. For Ref. [205], the coding error mentioned in the text has been corrected, and photoproduction values are used for  $b_1$  and  $b_2$  [206, 207]. The data key is in Table 3.1. The  $180^\circ$  curves are all extremely close to the  $155^\circ$  ones and hence are not shown.

### 4.3 Comparing $\chi$ EFT with Dispersion Relations

We compare the values for various polarisabilities extracted from various DR and  $\chi$ EFT calculations in Table 4.2. Overall, the agreement is very good. We note that the integral for  $\alpha_{E1}^{(p)} - \beta_{M1}^{(p)}$  in the hyperbolic dispersion relation is somewhat sensitive to assumptions about high-energy physics, but the value found there is within the error bar of the various EFT fits. The result for  $\alpha_{E1}^{(p)} + \beta_{M1}^{(p)}$  is even more sensitive to high-energy physics, which makes it remarkable that the agreement with the  $\mathcal{O}(P^3)$   $\chi$ PT prediction is so good. The apparent variation of the static values of the spin polarisabilities may be settled in the near future by a series of ongoing and planned experiments with polarised targets and beams (see Section 6.1).

Far more informative than the static ( $\omega = 0$ ) values of the polarisabilities are their full functional forms. These were calculated in (modified)  $\mathcal{O}(\epsilon^3)$  by Hildebrandt et al. [14] and compared with the results of the DR analysis of Drechsel et al. [15], as updated in Ref. [14]. In Fig. 4.7 we show results

	$\mathcal{O}(P^3)$	$\mathcal{O}(P^4)$ [192, 198]	Mod. $\mathcal{O}(\epsilon^3)$ [14]	Fixed-t [15, 88, 89]	Fixed- $\theta=180^\circ$ [15]
$\alpha_{E1}^{(p)} + \beta_{M1}^{(p)}$	13.8	$15.4 \pm 1.4^*$	$13.8 \pm 0.4^\dagger$	$13.2 \pm 0.9 \pm 0.7^*$	N/A
$\alpha_{E1}^{(p)} - \beta_{M1}^{(p)}$	11.3	$8.8 \pm 1.6^*$	$8.3 \pm 1.9^*$	$11.1 \pm 1.1 \pm 0.8^*$	10.9
$\alpha_{E1}^{(p)}$	12.5	$12.1 \pm 1.1 \pm 0.5^*$	$11.0 \pm 1.4^*$	$12.2 \pm 0.7 \pm 0.5^*$	N/A
$\beta_{M1}^{(p)}$	1.25	$3.4 \pm 1.1 \pm 0.1^*$	$2.8 \mp 1.4^*$	$1.1 \pm 0.7 \pm 0.5^*$	N/A
$\gamma_{E1E1}^{(p)}$	-5.7	-1.3	-5.7	$-3.85 \pm 0.45$	-3.8
$\gamma_{M1M1}^{(p)}$	-1.1	3.3	3.1	$2.8 \pm 0.1$	2.9
$\gamma_{E1M2}^{(p)}$	1.1	0.2	1.0	$-0.15 \pm 0.15$	0.5
$\gamma_{M1E2}^{(p)}$	1.1	1.7	1.0	$2.0 \pm 0.1$	1.6

Table 4.2: Previous calculations of proton polarisabilities.  $\dagger$  indicates that the Baldin sum rule was used.  $*$  indicates that the result was obtained by fitting to  $\gamma p$  data. In the  $\mathcal{O}(P^4)$  column, the second errors are theory errors; the errors of the modified  $\mathcal{O}(\epsilon^3)$  calculation are statistical only. In the fixed-t DR column, the second errors are from floating normalisations (see Section 4.1) and the numbers for spin polarisabilities are obtained by averaging the calculations of Refs. [88, 89] with uncertainties reflecting the range. The DR calculations presented here predict *all* spin polarisabilities, in contrast to the fit of Ref. [15] discussed in Sec. 4.1.

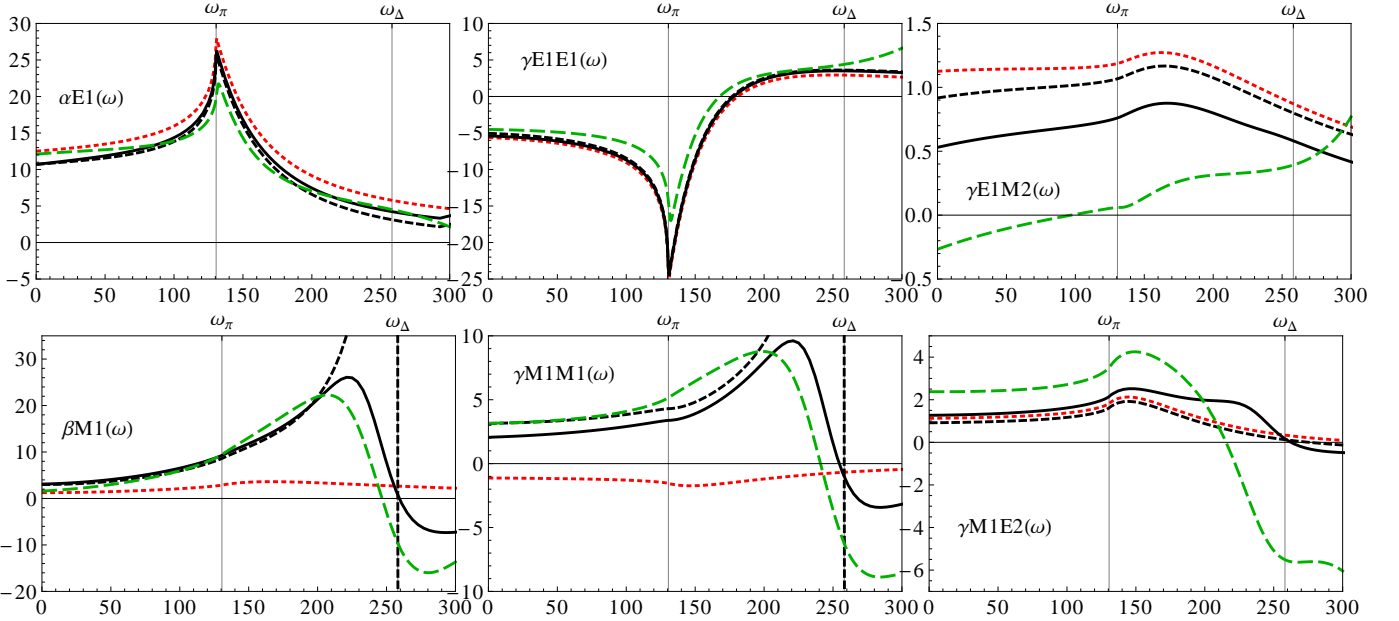


Figure 4.7: (Colour online) Comparison of DR results [15] (green long-dashed line) and  $\mathcal{O}(P^3)$ , modified  $\mathcal{O}(\epsilon^3)$  and modified  $\mathcal{O}(e^2\delta^3)$  EFT results (red dotted, and black dashed and solid lines respectively) for the real parts of the six dipole proton polarisabilities, as a function of cm energy. The  $\mathcal{O}(e^2\delta^3)$  EFT results use the parameters  $\alpha_{E1} = 10.7$ ,  $\beta_{M1} = 3.1$  and  $b_1 = 3.66$  as determined in the Baldin-constrained fit of Section 4.4, whereas the  $\mathcal{O}(\epsilon^3)$  result uses the same polarisabilities but a non-relativistic  $\Delta(1232)$  propagator and hence  $b_1 = 5$  as discussed in Section 4.2.8. The threshold for pion production and the peak of the  $\Delta(1232)$  Breit-Wigner cross section are marked by  $\omega_\pi$  and  $\omega_\Delta$  respectively. Note the difference in scales and the inherent theoretical uncertainties of each approach.

for EFT fits with the parameters which will be obtained from the proton Compton data in Section 4.4. Keeping in mind the inherent theoretical uncertainties of the DR and EFT approaches, the shapes of all six dynamical dipole polarisabilities agree remarkably well up to photon energies of around 200 MeV (centre-of-mass). For the modified  $\mathcal{O}(e^2\delta^3)$  EFT which includes a  $\Delta(1232)$  width, the shape agreement continues above 200 MeV for all but the two mixed spin polarisabilities. However, for most energies, these are numerically small so that higher-order effects may be more prominent. The similarity emphasises the point that the energy dependence of  $B_i(\nu, t)$  is driven by near-threshold dynamics, even if the value of  $B_i(0, t)$  is sensitive to higher-energy physics. Its origin is the fact that HB $\chi$ PT captures the large  $E_{0+}$  photoproduction multipole that generates a significant  $E1$  excitation of the pion cloud of the nucleon. This is clearly seen in the cusps at the pion-production threshold, most prominent in the polarisabilities of  $E1E1$  multipoles. We see in the table that the static  $\mathcal{O}(P^3)$  value for  $\alpha_{E1}^{(p)}$  agrees exceptionally well with the DR result, while that for  $\gamma_{M1M1}^{(p)}$  is in reasonable accord with DR.

However, the  $M1$  excitation is not properly described in  $\chi$ EFT until the  $\Delta(1232)$  is included. This is reflected in the improved agreement between DRs and the  $\chi$ EFT calculation with dynamical  $\Delta(1232)$  in the second block of the table, compared to the  $\Delta$ -less calculation of the first block, and even more so by the prominence of the  $\Delta(1232)$  resonance in the polarisabilities containing an  $M1$  multipole in Fig. 4.7. The poor agreement around the  $\Delta$  peak for  $\gamma_{M1E2}$  is rather surprising in this regard, since the  $E2$  electric transition vertex is included in the EFT Lagrangian (4.17). The pronounced structure in the DR description in the 160–250 MeV region is markedly different from what is seen in the  $\chi$ EFT calculation; this discrepancy needs further study.

Finally, even a  $\mathcal{O}(e^2\delta^4)$   $\chi$ EFT calculation does not have the strong  $\pi\pi$  interactions in the  $t$ -channel which generate a substantial contribution to  $\alpha_{E1}^{(p)} - \beta_{M1}^{(p)}$  that offsets the effect of the  $\Delta(1232)$  in that quantity. Whether this contribution is modelled as a  $\sigma$  or constructed through the  $t$ -channel DR (4.6), it is present in the numbers given in the last two columns. It is incorporated in current  $\chi$ EFT calculations only as a contribution to a  $\alpha_{E1}^{(p)} - \beta_{M1}^{(p)}$   $\gamma$ N contact operator. Therefore, the fact that the static and dynamical scalar polarisabilities in  $\chi$ EFT and DR agree suggests that the energy dependence of this process is negligible below about 300 MeV, which is consistent with the phenomenology of the correlated  $2\pi$  state.

#### 4.4 A new fit to the proton data

As outlined in Section 4.2.8, in the  $\delta$  expansion, it should be possible to fit purely  $\Delta(1232)$  parameters in the resonance region, leaving only  $\alpha_{E1}^{(p)}$  and  $\beta_{M1}^{(p)}$  to be fit to low-energy data. This section presents the results of a fit using this strategy.

All the experiments have an overall normalisation error. We incorporate this by adding a piece to the usual  $\chi^2$  function:

$$\begin{aligned} \chi^2 &= \chi_{\text{stat.}}^2 + \chi_{\text{sys.}}^2 \\ &= \sum_{j=1}^{N_{\text{sets}}} \sum_{i=1}^{N_j} \left( \frac{\mathcal{N}_j (d\sigma_{ij}/d\Omega)_{\text{expt}} - (d\sigma_{ij}/d\Omega)_{\text{theory}}}{\mathcal{N}_j \Delta_{ij}} \right)^2 + \sum_{j=1}^{N_{\text{sets}}} \left( \frac{\mathcal{N}_j - 1}{\mathcal{N}_j \delta_j} \right)^2, \end{aligned} \quad (4.19)$$

where  $(d\sigma_{ij}/d\Omega)_{\text{expt}}$  and  $\Delta_{ij}$  are the value and statistical error of the  $i$ th observation from the  $j$ th experimental set,  $\delta_j$  is the fractional systematic error of set  $j$ , and  $\mathcal{N}_j$  is an overall normalisation for set  $j$ . The additional parameters  $\mathcal{N}_j$  are to be optimised by minimising the combined  $\chi^2$ . This can be done analytically, leaving a  $\chi^2$  that is a function of  $\alpha_{E1}^{(p)}$  and  $\beta_{M1}^{(p)}$  alone. The number of degrees of freedom in the final minimisation is reduced by the number of independent data sets used. For more details on this formalism, see Ref. [212]. The best justification we have found in the modern literature for the precise form of this expression (specifically, the inclusion of  $\mathcal{N}_j$  in the denominators) is from d’Agostini [213].

We perform a fit at modified third order,  $\mathcal{O}(e^2\delta^3)$  plus the counterterms of Eq. (4.11), then one at fourth order,  $\mathcal{O}(e^2\delta^4)$ . For reasons which will become clear below, we regard the latter only as a consistency check on the former. The basic ingredients of the modified third-order calculation were described in Section 4.2 and shown in Figs. 4.2–4.5. These are nucleon Born diagrams and pion- and  $\Delta$ -pole diagrams,  $\pi N$  loops,  $\pi\Delta$  loops and the photon-nucleon seagull terms from  $\mathcal{L}^{(4)}$  which give LEC contributions  $\delta\alpha_{E1}^{(p)}$  and  $\delta\beta_{M1}^{(p)}$  to the polarisabilities. The nucleon Born diagrams are calculated to fourth order as given by McGovern [197], and they are indistinguishable from the full relativistic form given by Babusci et al. [88] for the energies of interest. The pion-pole contributions are given by Bernard et al. [98]; this form does not change at fourth order and is indeed relativistically invariant, although at higher orders, form factors would still enter at the vertices. The  $\pi N$  loops are given at third order by Bernard et al. [98] and at fourth order by McGovern [197]. At both third and fourth order, we use  $\omega_s = \sqrt{s} - M_N$  to shift the threshold to the correct place. The  $\pi\Delta$  loops are given by Hildebrandt et al. [14] in his Appendix B, except that we use  $\omega_{\text{Breit}}$  throughout in place of  $\omega_s$  and  $\omega_u$  to preserve crossing symmetry. The  $s$ - and  $u$ -channel  $\Delta$ -pole diagrams are calculated using the Lagrangian of Pascalutsa and Phillips [205]; the expressions given in Appendix A3 of that paper refer to a redundant, covariant set of operators which we reduce to our usual six in the Breit frame. Strict consistency in the  $\delta$  counting would require us to use the third-order nucleon Born contribution at this order. However, since the main contribution at fourth order consists of terms of order  $\omega^2$  in  $A_1$  and  $A_2$ , polarisabilities extracted at different orders will be more comparable if these terms are always included. With regard to the  $\Delta$  pole, Pascalutsa and Phillips have detailed which terms are leading or sub-leading in the low-energy and resonance regions; following their scheme, we include all terms in both regions to avoid discontinuities. At third and fourth order, the  $\gamma N\Delta$  vertices and  $\Delta$  propagator should strictly be expanded in powers of  $\omega/M_N$ ,  $\Delta/M_N$  and  $\omega/\Delta$ , but again, to avoid artificial shifts in polarisabilities in going from one order to the next, we keep the full Dirac structures. The  $\Delta$  parameters we use are  $\Delta_M = 293$  MeV and  $g_{\pi N\Delta} = 1.425$ , which are fit to the Breit-Wigner peak position and width, the latter via the relativistic formula. These, and not the pole position, must be used if the resonance is to be reproduced.

First we present our main result, from a modified  $\mathcal{O}(e^2\delta^3)$  calculation. Our strategy is to first determine the  $\gamma N\Delta$  couplings by considering the resonance region. By eye it is apparent that with typical values of  $\alpha_{E1}^{(p)} = 11$  and  $\beta_{M1}^{(p)} = 3.4$  and with  $b_2/b_1 = -0.34$ , a reasonably convincing overall reproduction of the MAMI data up to the peak around 325 MeV can be obtained with  $b_1 = 3.7$  (close to the Pascalutsa and Vanderhaeghen value of  $b_1 = 3.76$  [206]). Above the peak, the cross section falls off too slowly at forward angles and too fast at backward angles, but we hardly expect to fit well at these high energies. (See Fig. 4.8, solid blue curve.) For that reason, unlike Pascalutsa and Phillips, we do not adjust  $b_2$ . Below the peak, the fit is always better to the MAMI data than the LEGS data (where they disagree) even if the peak height is raised. In view of this problem, and considering the fact that the former will dominate statistically, we choose to fit only to the MAMI data.

Thus we fit  $b_1$  to the MAMI data from 200 MeV up to 325 MeV, then we fit  $\alpha_{E1}^{(p)}$  and  $\beta_{M1}^{(p)}$  to the low-energy data up to 170 MeV, iterating until convergence is reached. If we exclude the Hallin data, we obtain a solution with a good  $\chi^2$ . Looking at individual experiments, however, we see that the Baranov data at 150 MeV (which we treat as an independent data set, following Ref. [212]) have a  $\chi^2$  per degree of freedom (d.o.f.) of over 3 and should therefore be excluded from the fits. The Olmos de León data, which form nearly half the total, are fit with an acceptable  $\chi^2$  of 73 for 65 d.o.f. If we include the 27 Hallin points in this energy range, though, the  $\chi^2$  of 41 for 27 d.o.f. is hard to accept, and we prefer to quote our best results without it. (The specific  $\chi^2$  above is taken from the fit constrained by the Baldin sum rule but is hardly changed if that constraint is lifted.)

The central result for the modified  $\mathcal{O}(e^2\delta^3)$  fit without using the Baldin sum rule is then (rounded to one decimal place)

$$\alpha_{E1}^{(p)} = 10.5 \pm 0.5(\text{stat}) \pm 0.8(\text{theory}) \quad , \quad \beta_{M1}^{(p)} = 2.7 \pm 0.5(\text{stat}) \pm 0.8(\text{theory}) \quad (4.20)$$

with  $\chi^2 = 106.1$  for 124 d.o.f. (or  $\alpha_{E1}^{(p)} + \beta_{M1}^{(p)} = 13.2 \pm 0.9$  and  $\alpha_{E1}^{(p)} - \beta_{M1}^{(p)} = 7.8 \pm 0.6$ , since the principal axes of the  $\chi^2_{\min} + 1$  ellipses align fairly closely with these axes). These are obtained with  $b_1 = 3.66 \pm 0.03$ . With the Baldin constraint of  $\alpha_{E1}^{(p)} + \beta_{M1}^{(p)} = 13.8 \pm 0.4$ , the result is  $\alpha_{E1}^{(p)} - \beta_{M1}^{(p)} = 7.7 \pm 0.6$  with  $\chi^2 = 106.5$  for 125 d.o.f. and the same  $b_1$  as before, which gives

$$\alpha_{E1}^{(p)} = 10.7 \pm 0.3(\text{stat}) \pm 0.2(\text{Baldin}) \pm 0.8(\text{theory}), \quad \beta_{M1}^{(p)} = 3.1 \mp 0.3(\text{stat}) \pm 0.2(\text{Baldin}) \pm 0.8(\text{theory}). \quad (4.21)$$

If the low-energy fits are repeated with  $b_1$  varied within its limits,  $\alpha_{E1}^{(p)} - \beta_{M1}^{(p)}$  changes by less than 0.1. Varying the upper cutoff between 300 and 350 MeV scarcely changes  $\alpha_{E1}^{(p)} - \beta_{M1}^{(p)}$ . Restoring the two omitted data sets (Hallin and Baranov  $150^\circ$ ) also results in an upward shift in  $\alpha_{E1}^{(p)} - \beta_{M1}^{(p)}$  of 0.1. We therefore conclude that our fit is stable. Visually, the agreement with the bulk of the data continues far above the low-energy region, without any obvious systematic problems, as can be seen in Fig. 4.9.

To arrive at the quoted theory error on our results, we note that we perform an  $\mathcal{O}(e^2\delta^3)$  fit in a framework in which the polarisabilities first enter at  $\mathcal{O}(e^2\delta^2)$ . We would expect corrections to be of order  $\delta^2 \sim 16\%$  of the lowest-order result, or  $\delta \sim 40\%$  of the shift between the LO and NLO results; taking  $(\alpha_{E1}^{(p)} + \beta_{M1}^{(p)})/2 \approx 7$  to set the scale for the first approach gives 1.1, while taking the shifts in the values of  $\alpha_{E1}^{(p)}$  and  $\beta_{M1}^{(p)}$  from third order to fourth order to be  $\approx 2$  gives 0.8 in the second approach. In view of the similarity between our third- and fourth-order results (see later), the stability under inclusion or exclusion of data sets, and the values obtained in the  $\mathcal{O}(P^4)$  and  $\mathcal{O}(\epsilon^3)$  fits [14, 198], we consider the latter to be already conservative and so we use it.

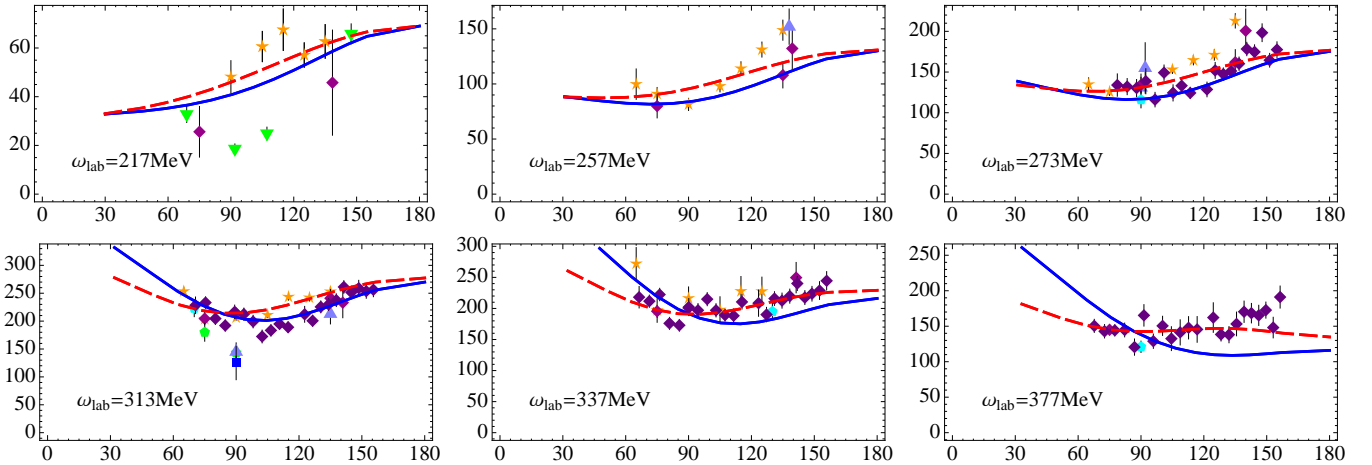


Figure 4.8: (Colour online) Comparison of third-order (blue, solid) and fourth-order (red, dashed) cross sections with Compton-scattering data in the intermediate- and high-energy regions. Centre-of-mass (cm) cross section in nb/sr plotted in bins of 8 MeV as a function of cm photon angle. In both cases,  $\alpha_{E1}^{(p)} = 10.5$  and  $\beta_{M1}^{(p)} = 2.8$ ;  $b_1 = 3.66$  and  $3.47$ , respectively. See Table 3.1 for key.

Next we look at the  $\mathcal{O}(e^2\delta^4)$  fit, which differs from the previous one by the inclusion of the NLO pieces of  $\pi N$  loops (in the  $\chi$ EFT expansion). The first observation is that, with  $\alpha_{E1}^{(p)}$  and  $\beta_{M1}^{(p)}$  as above but with a somewhat reduced  $b_1$  of 3.48, the general trend of the data in the resonance region and above is improved; the exaggerated angular dependence of the third-order cross section is tamed (see Fig. 4.8). However, at low energy, the fit is systematically worse, with the fourth-order curve lying above the third-order one—and above the data—at all angles. If we repeat the fit procedure detailed above, the value  $b_1 = 3.48$  is confirmed, but the best fit constrained by the Baldin sum rule has a  $\chi^2$  of 170; relaxing the Baldin constraint drops the  $\chi^2$  to 137 but with  $\alpha_{E1}^{(p)} + \beta_{M1}^{(p)} = 18.7$ . In fact, this is not



a surprise: McGovern and Hildebrandt et al. independently found that adding either NLO pion loops or the  $\Delta$  separately raised the cross section around the photoproduction threshold and improved the fit compared with third-order pions alone; adding both is too great a correction.

With both  $\alpha_{E1}^{(p)}$  and  $\beta_{M1}^{(p)}$  as fit parameters, the primary contribution of the  $\Delta(1232)$  at low energies is via the spin polarisability  $\gamma_{M1M1}^{(p)}$ . Just as inclusion of the  $\Delta$  at third order requires promotion of the strictly fourth-order counterterms for  $\alpha_{E1}$  and  $\beta_{M1}$ , it would appear that, at fourth order, promotion of one or more fifth-order counterterms for the spin polarisabilities is required. Various strategies are possible: we could promote all four and fit them all, or we could find out which is the most important and fit just that one, or we could take  $\gamma_{M1M1}$  as the one with the largest  $\Delta$  contribution. With any of these strategies, we can get an acceptable low-energy fit. However, there are very flat directions in parameter space if we promote all four, and in the absence of further constraints, it is not clear what we learn from the procedure. In fact, the best low-energy results from promoting a single polarisability are obtained with  $\gamma_{M1M1}$ , so we choose this; the Baldin-constrained results are then  $\alpha_{E1}^{(p)} - \beta_{M1}^{(p)} = 7.6 \pm 0.8$  and  $\gamma_{M1M1}^{(p)} = 2.6 \pm 0.5$  with  $\chi^2 = 116.7$ ; this is obtained with  $b_1 = 3.59$ .

It is reassuring to note that the fitted value of  $\gamma_{M1M1}^{(p)}$  is “sensible” when compared to DR estimates (see Table. 4.2), whereas unfitted it is distinctly large at 6.4. However, in view of the choices we have had to make in obtaining  $\gamma_{M1M1}^{(p)}$ , we would caution against treating our result as a chiral-EFT extraction of this parameter. Only low-energy polarisation measurements will have real power to constrain spin polarisabilities. It should also be noted that the fit at higher energies is degraded in the forward direction. For this reason, we prefer to consider the third-order results for  $\alpha_{E1}^{(p)}$  and  $\beta_{M1}^{(p)}$  of Eqs. (4.20) and (4.21) as the most reliable, using the fourth-order fit simply for reassurance that these results are stable against the inclusion of higher orders.

Our results agree within errors with the results of Beane et al. and Hildebrandt et al. (see Table. 4.2). The errors quoted on the former were taken from the limits of the  $1\sigma$  curve ( $\chi_{\min}^2 + 2.3$ ) as a function of  $\alpha_{E1}^{(p)}$  and  $\beta_{M1}^{(p)}$  and hence are large compared with those obtained from the more conventional  $\chi_{\min}^2 + 1$  measure used here (equivalent to marginalising over the other parameter) which explains our tighter errors. In general, fits which include data above 170 MeV prefer higher values of both  $\alpha_{E1}^{(p)}$  and  $\beta_{M1}^{(p)}$ , which may account for their higher central values. Like Baranov et al. [212], we find that most low-energy data sets, old and new, are compatible with one another (including, with the caveats of Section 3.3, the Olmos de León data set which was not available to Baranov at the time), and our results are again compatible with his but with a distinctly smaller  $\alpha_{E1}^{(p)} - \beta_{M1}^{(p)}$ .

Further details of the calculation described in this section are the subject of a forthcoming paper [214].

## 4.5 Other methods

We close this section by briefly discussing other approaches which incorporate the  $\pi N$  and  $\Delta(1232)$  dynamics that are key to describing  $\gamma p$  data in this energy domain.

The approach of Gasparyan and Lutz [215, 216] emphasises causality and unitarity. In these works, Compton scattering is analysed using the  $\chi$ PT Lagrangian. Partial-wave amplitudes are obtained by an analytic continuation of amplitudes computed in ( $\Delta$ -less)  $\chi$ PT in the sub-threshold region. An integral equation that implements  $\pi N$ -analyticity and unitarity of the six Compton amplitudes is used to extrapolate to the kinematic region of interest. The difference from the work presented in Section 4.1 is that, in Refs. [215, 216], the input for pion photoproduction that saturates the integral equation is from  $\mathcal{O}(P^3)$   $\chi$ PT, not from data. Hence, multi-pion states have not, as yet, been included in the  $s$ -channel integral. Moreover, the absence of an explicit  $\Delta(1232)$  field in the Lagrangian is an additional dynamical assumption in this approach.

Nevertheless, this assumption is somewhat vindicated by comparison with the data—at least for the

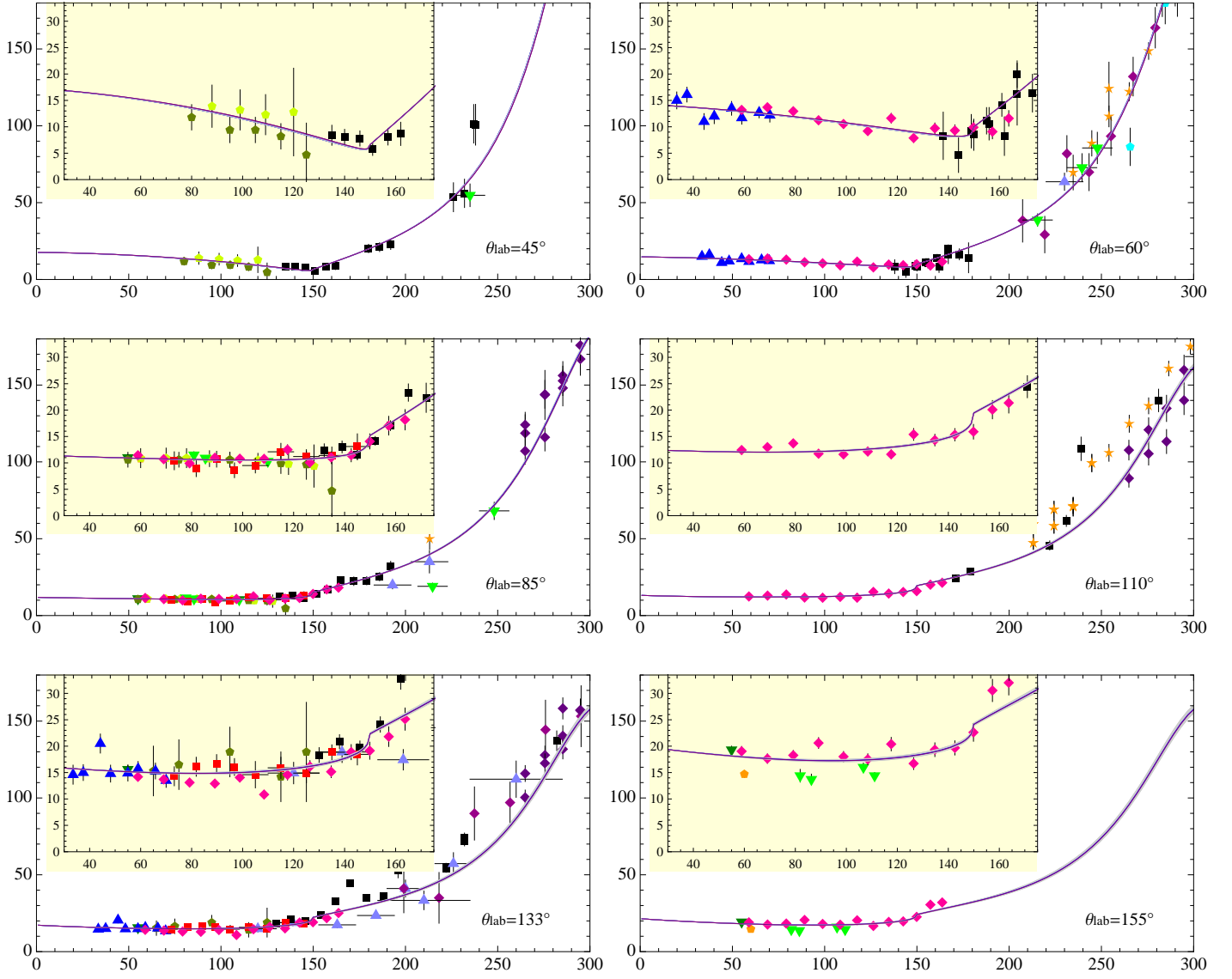


Figure 4.9: (Colour online) Comparison of third-order result with Compton-scattering data. Lab cross section in nb/sr plotted in bins of  $10^\circ$  lab angle as a function of lab photon energy in MeV. The insets show the fit region. The fits with and without the Hallin data are both plotted, but are indistinguishable. The barely visible narrow grey band shows the variation within the statistical error of the one-parameter fit. See Table 3.1 for key.

specific regulator choice and  $\mathcal{O}(P^3)$  calculation discussed in Ref. [215]. Gasparyan and Lutz can explain the  $\gamma p$  data up to energies of roughly  $\omega_{\text{lab}} \approx 450$  MeV with a quality comparable to that obtained in the  $\mathcal{O}(e^2\delta^3)$  computation (c.f. Fig. 4.9). Broadly speaking, this happens because photoproduction multipoles in this approach are in good agreement with extant data, and the constraints of gauge invariance, analyticity, and unitarity are all implemented. In contrast to the DR results displayed in Section 4.1 or the  $\chi$ EFT results discussed in Section 4.4, the  $\gamma p$  cross sections displayed in Ref. [215] are not a fit, since there are no additional free parameters in the Compton amplitude at this order. Because the calculation of sub-threshold amplitudes is matched to  $\chi$ PT, the  $\mathcal{O}(P^3)$  results for  $\alpha_{E1}^{(p)}$  and  $\beta_{M1}^{(p)}$  of Eq. (4.13) are obtained. The  $\chi$ PT results for  $\gamma_{E1M2}^{(p)}$  and  $\gamma_{M1E2}^{(p)}$  shown in Eq. (4.13) are also recovered, but the values found for  $\gamma_{E1E1}^{(p)}$  and  $\gamma_{M1M1}^{(p)}$  are closer to those obtained in DRs.

Finally, we consider the dressed  $K$ -matrix model of Kondratyuk and Scholten [217, 218], a relativistic approach that respects crossing symmetry. Two-body  $\pi N$ -unitarity is maintained by computing the scattering amplitude  $T$  in a coupled-channels ( $\pi N$ , photoproduction and Compton scattering) approach. Analyticity constraints are fully respected for one-particle reducible diagrams, but violated by the one-particle irreducible diagrams. The degrees of freedom used are the nucleon, the  $\Delta(1232)$ , and the  $\rho$  and  $\sigma$  mesons, together with higher nucleon resonances. Most parameters are determined by a combined fit to  $\pi N$ ,  $\gamma p \rightarrow \pi N$  and  $\gamma p$  data. For Compton scattering, the two key parameters are in the  $\gamma\gamma\sigma$  vertex, and they are adjusted to reproduce the backward  $\gamma p$  cross section at moderate energies. In order to reproduce the differential cross section around pion-production threshold, and in particular the cusp seen there, the one-particle irreducible diagrams shown in Fig. 4.3 are added to the calculation in an ad hoc and approximate way. As in Ref. [215], the good description of  $\pi N$  data and photoproduction up to  $\omega_{\text{lab}} \approx 450$  MeV, together with the implementation of analyticity and unitarity, helps ensure a fairly successful result for  $\gamma p$  cross sections. After the fit to the data was performed, polarisabilities were extracted from the model, with results similar to the DR and  $\chi$ PT evaluations:  $\alpha_{E1}^{(p)} = 12.1$ ,  $\beta_{M1}^{(p)} = 2.4$ . The small value of  $\beta_{M1}$  again results from the  $\sigma$  meson cancelling most of the  $\Delta(1232)$  contribution. The diagrams of Fig. 4.3 are crucial to describing  $\alpha_{E1}^{(p)}$  and  $\gamma_{E1E1}^{(p)}$ , but are only a small perturbation in  $\beta_{M1}^{(p)}$ . Together with the subsequent results of Ref. [218], this implies that reducibility and analyticity are not the best guides for constructing a consistent description of Compton-scattering data for  $\omega_{\text{lab}} < 350$  MeV. It also reminds us that, especially for structure constants at higher orders in the  $\omega$  expansion,  $\pi N$  and  $\Delta(1232)$  physics play a key role and ultimately determine many aspects of the shape of Compton observables.

## 5 Compton scattering from two- and three-nucleon systems

Does the neutron have a similar Compton response as the proton? We saw in Section 4.2 that  $\chi$ EFT predicts the isoscalar polarisabilities to be one order in  $P/\Lambda_\chi \approx \frac{1}{5}$  larger than the isovector ones, indicating that neutron and proton polarisabilities should agree at the 20% level. This is not unexpected, since the largest contributions to nucleon polarisabilities of all kinds come from charged-pion dynamics and excitation of the  $\Delta(1232)$ , and both of these mechanisms are predominantly isoscalar.

As already mentioned, the structure functions  $\bar{A}_i$  (2.11) of the neutron can be probed indirectly by embedding it into a light, stable nucleus. In  $\chi$ EFT, elastic Compton scattering has indeed been explored for the deuteron in Refs. [91–93, 101, 136, 199, 219–222] and for  ${}^3\text{He}$  in Refs. [69–71]. Since the deuteron is isoscalar, its Compton amplitude is sensitive only to the isoscalar polarisabilities. Neutron polarisabilities are then obtained by combination with the proton polarisabilities found in the preceding section, Eqs. (4.20) and (4.21). We first concentrate on the deuteron, since this is the only case for which data are presently available, and we compare these data to non- $\chi$ EFT calculations in Section 5.5. The case of  ${}^3\text{He}$  is discussed in Sections 5.6 and 6.1 below. In that case, both isoscalar and isovector polarisabilities affect the cross section, but  ${}^3\text{He}$  behaves approximately as a free-neutron target for polarisation observables.

In nuclei, nuclear effects such as meson-exchange currents and nuclear binding act in concert with the single-nucleon Compton amplitude. EFT allows the rigorous and systematic calculation of such effects in a model-independent way and with a well-defined theoretical uncertainty. Analysing the proton, deuteron and  ${}^3\text{He}$  in one common EFT framework can thus lead to high-accuracy determinations of the proton and neutron polarisabilities. However, the corresponding coherent Compton-scattering experiments are challenging, as described in Section 3.4, and the accuracy claimed in an EFT calculation must be checked by comparing to data. To overdetermine polarisabilities by multiple extractions from experiments on different systems thus provides important cross-checks on both experiment and theory.

## 5.1 $\chi$ EFT for few-nucleon systems

The effective theory of few-nucleon systems is significantly more involved than that discussed in Section 4.2, as the shallow binding of light nuclei complicates the picture. The S-wave NN scattering lengths  $a(^3S_1) \approx 5$  fm and  $a(^1S_0) \approx -24$  fm are much larger than typical large-distance scales of the one-nucleon sector, such as the pion Compton wavelength. Concomitantly, the deuteron binding energy  $B_d \approx 2.225$  MeV is small compared to the typical QCD energy scale, and the corresponding “binding momentum” (inverse size)  $\gamma \equiv \sqrt{M_N B_d} \approx 46$  MeV  $\approx 1/a(^3S_1)$  is appreciably less than even the typical “chiral”  $\chi$ EFT scale  $m_\pi$ . Therefore, low-energy S-wave NN rescattering is nonperturbative at low energies. Iterates of the NN potential are not suppressed by chiral symmetry and must at least partially be resummed.

In practice this is achieved by defining a leading-order NN potential, which is then iterated via the Schrödinger equation, in order to generate the LO wave function of the nuclear bound state. In  $\chi$ EFT, at LO, the long-range part of the NN potential is given by one-pion exchange, constructed from the chiral Lagrangian, Eqs. (4.8) to (4.10). Weinberg proposed [223, 224] that this long-range potential should be supplemented at LO by two S-wave contact interactions, whose strengths are determined from the above-mentioned fine-tuned physical scales. This potential yields a Hamiltonian which is unbounded from below, and so a cutoff must be placed on the Schrödinger equation in order to obtain physically sensible predictions. Refs. [225–229] have pointed out that additional contact interactions (e.g. in attractive P waves) must be added to this LO potential in order to make the NN phase shifts independent of the cutoff used in solving the Schrödinger equation. A number of proposals for dealing with orders beyond LO also exist (see, e.g., Refs. [230–234]). The question of how to build a  $\chi$ EFT for NN scattering that is valid over a large range of cutoffs must be regarded as presently unresolved.

However, Epelbaum and Meißner argue in Ref. [235] that the  $\chi$ EFT proposed by Weinberg for few-nucleon systems is consistent if the cutoff is kept at  $\lesssim 800$  MeV, namely roughly the mass of the  $\rho$  meson. Weinberg’s proposal is that all diagrams contributing to the nuclear potential are classified according to their  $\chi$ PT order. For example, the NLO potential includes two-pion exchange (constructed from the first-order vertices in Eq. (4.10)), together with additional contact interactions. The entire potential at a fixed order is then inserted into the Schrödinger equation to obtain the nuclear wave function. For cutoffs in the range 500 to 800 MeV, NN potentials based on this power counting have been constructed to N<sup>3</sup>LO, with very little cutoff dependence observed in this range [236, 237]. Furthermore, this N<sup>3</sup>LO potential produces a  $\chi^2$  per degree of freedom with respect to the NN data which is comparable to that of “high-precision” NN potential models. Consistent three-nucleon forces have also been obtained to N<sup>3</sup>LO [238–240]. This method has been successfully applied in a number of reactions on deuterium:  $\pi d$ ,  $e^- d$ ,  $\dots$ ; see e.g. [168] for a recent review. It is this scheme that we shall use to construct  $\chi$ EFT deuteron wave functions. Additional details regarding the pros and cons of this procedure can be found e.g. in [164–167]. But, as far as Compton scattering is concerned, we will demonstrate in Section 5.2.4 that *any* NN potential can be used for deuteron Compton scattering at the energies and level of accuracy of the present data—as long as that potential captures the correct long-distance physics of one-pion exchange and reproduces NN scattering data reasonably well. The advantage of Weinberg’s power counting for the NN potential and operators of nuclear Compton scattering is that the consequences of chiral-symmetry breaking are included in the calculation in a straightforward manner, and a potential of the minimal complexity needed to obtain results at the desired level of accuracy is employed.

## 5.2 Compton scattering from the deuteron in $\chi$ EFT

### 5.2.1 Scales and regimes

We now turn to the presentation of  $\chi$ EFT calculations of  $\gamma d$  scattering. As before, we begin by examining the  $\chi$ EFT variant without dynamical  $\Delta(1232)$  degrees of freedom and postpone including

the  $\Delta$  to Section 5.2.3. Thus we first count in powers of the generic scale  $P$  and still define the leading-order nuclear Thomson term<sup>11</sup> as  $e^2 \sim P^2$ .

The deuteron binding momentum is not the only new scale in few-nucleon systems. In the one-nucleon sector of Section 4.2, recoil effects are suppressed because the nucleon mass is much larger than the energy of any pions or photons participating in the reactions of interest. Recoil between two nucleons cannot be neglected, however, because they have the same mass. The nonrelativistic kinetic energy of a nucleon with momentum  $\vec{p}$  propagating close to its mass shell in the few-nucleon system is thus  $E \approx \vec{p}^2/(2M_N) \sim P^2 \ll |\vec{p}| \sim P$ . After interaction with a photon, its propagator is given by

$$\frac{iM_N}{M_N E \pm M_N \omega - (\vec{p} \pm \vec{k})^2} \quad , \quad (5.1)$$

which converts the photon energy into a new NN momentum scale  $\sqrt{M_N \omega} \gg \omega$  which is “hard” relative to  $\omega$ . The (+) sign applies to photon absorption by the nucleon and the (−) sign to photon emission. This scale only appears when the photon’s energy-momentum flow must be routed through a nucleon and not when two photons couple instantaneously to the same nucleon; cf. discussion of Fig. 5.1 below.

While a fourfold expansion in the low  $\chi$ EFT scales  $\omega$ ,  $\sqrt{M_N \omega}$ ,  $\gamma$  and  $m_\pi$  is possible, it is more convenient to approximately identify scales until only one is left. We set  $\gamma \sim m_\pi$  and define two different **regimes** of photon energy, relative to energy scales built out of the chiral scale  $P$  [199, 220–222].

**Regime I** has comparable chiral and hard photon scales,  $\sqrt{M_N \omega} \sim m_\pi \sim P$ , i.e.  $\omega \sim 20$  MeV, so that the intermediate-state propagator (5.1) scales as  $P^{-2}$ . This Regime is discussed in Section 5.2.2.

**Regime II**, on the other hand, treats the photon energy as a soft scale which is close to the chiral one,  $\omega \sim 140$  MeV  $\sim P$ , so that the hard scale is  $\sqrt{M_N \omega} \sim P^{\frac{1}{2}}$  and the intermediate-state propagator (5.1) counts as  $P^{-1}$ , i.e. one order less. Numerically, this implies  $\sqrt{M_N \omega} \sim 360$  MeV, which is still small compared to the breakdown scale of  $\chi$ EFT when the  $\Delta(1232)$  is included dynamically. But convergence for these energies is in powers of  $\sqrt{M_N \omega}/\Lambda_\chi$  and hence not as rapid as in Regime I. This will be discussed in Section 5.2.3, where we also include a dynamical  $\Delta(1232)$  as we did in the single-nucleon sector of Section 4.2.7.

We will see that the mechanisms probed in each Regime are quite different. The transition from one to the other is obviously not abrupt but rather gradual, and the central values defined here provide only a priori estimates. For example, Regime II involves an expansion in  $(\gamma^2, m_\pi^2)/(M_N \omega)$  which breaks down completely when  $\omega \sim m_\pi^2/M_N \lesssim 20$  MeV. The discussion in Section 5.2.3 will even show that its higher-order terms already have a marked effect for  $\omega \approx 50$  MeV. Since the available deuteron data lie in that intermediate region,  $49 \text{ MeV} \leq \omega_{\text{lab}} \leq 95 \text{ MeV}$ , we will analyse them in Section 5.3 by a formulation which is applicable in both Regimes, introduced in Section 5.2.4.

## 5.2.2 Very low energies and the Thomson limit

The Thomson limit of vanishing photon energy (see Eqs. (1.1) and (2.3)) imposes a stringent constraint on the few-nucleon Compton amplitudes in Regime I since the photon cannot resolve the target structure or spin:

$$\lim_{\omega \rightarrow 0} T(\omega, \theta) = -\frac{Z^2 e^2}{M_X} \vec{\epsilon}'^* \cdot \vec{\epsilon} + \mathcal{O}(\omega) \quad . \quad (5.2)$$

Since  $e^2 \sim P^2$ , the amplitude indeed scales as  $P^2$ . While such a low-energy expansion breaks down as  $\omega$  approaches the first intrinsic low-energy scale of the object, it not only dominates the deuteron amplitude for  $\omega \lesssim B_d$ , but constrains the cross section throughout Regime I; see Section 5.2.4.

<sup>11</sup>Different power-counting notations exist in the literature, including renaming the parameter to  $Q$ . In some, the deuteron Compton amplitudes start at order  $e^2 Q^{-1}$  [93, 96, 241, 242], but our choice allows an intuitive translation between the one- and two-nucleon sectors; see also the note below Eq. (5.3).



The significance of the Thomson limit comes from the fact that it is based on gauge invariance. This, in turn, implies that the total matrix element of all electromagnetic current operators is conserved<sup>12</sup>, including photon couplings to charged mesons like the pion which provide nuclear binding. Thus, Friar used the Thomson constraint in conjunction with the generalised Siegert theorem to avoid specifying the exact form of meson-exchange current operators [9, 243]. In later work, Arenhövel and Weyrauch constructed explicit expressions for these operators and showed that the theorem enforces cancellations between different contributions [244, 245]. These significant simplifications and stringent numerical tests form the foundation of the modern theoretical description of deuteron Compton scattering in Regime I [77, 91–93, 246–251]. Ultimately, the practical importance of the Thomson limit is not only the *fact* that it is fulfilled, but also *how* it is fulfilled. Here, we motivate the results of Refs. [6, 9, 243–245] from the EFT perspective, cf. [93, 96, 241, 242].

An exact low-energy theorem must be observed at each individual order in the generic expansion parameter of any EFT. In the one-nucleon sector of Section 4.2, the Thomson limit is automatically fulfilled; but NN rescattering complicates the picture in few-nucleon systems. Figure 5.1 shows all leading-order,  $\mathcal{O}(P^2)$ , contributions in Regime I. In diagram (a), the one-nucleon seagull term is con-

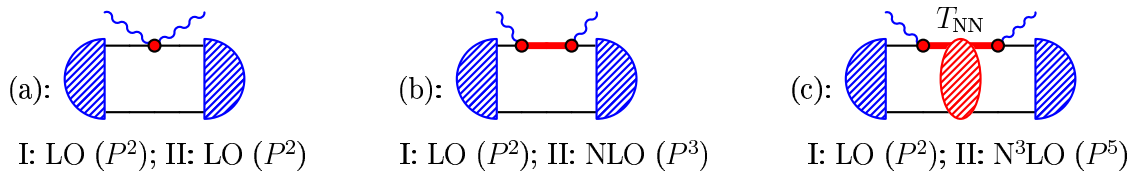


Figure 5.1: (Colour online) Deuteron Compton scattering in Regime I at LO,  $\mathcal{O}(P^2)$ : one-nucleon seagull term (a); intermediate-nucleon propagation without, (b), and with rescattering (c; hatched ellipse:  $T_{\text{NN}}$ ). Thick (red) line: nucleon carrying photon energy as in Eq. (5.4); dot: coupling from  $\mathcal{L}_{\pi\text{N}}^{(2)}$  via minimal substitution and the magnetic moment. Crossed and permuted diagrams not displayed. Also indicated is the order at which each graph contributes in Regimes I and II, respectively.

voluted with the deuteron wave function, and no momentum is transferred at zero energy:

$$T_{\text{seagull}}(\omega \rightarrow 0) = \langle \Psi_{\text{d}} | \left( -\frac{e^2}{M_{\text{N}}} \vec{\epsilon}'^* \cdot \vec{\epsilon} \right) | \Psi_{\text{d}} \rangle = -\frac{e^2}{M_{\text{N}}} \vec{\epsilon}'^* \cdot \vec{\epsilon} . \quad (5.3)$$

This is the Thomson limit for an individual nucleon, i.e. twice the deuteron result, and would therefore overpredict the deuteron cross section by a factor of 4. Sachs and Austern showed that contributions (b) and (c) yield an amplitude  $+e^2 (\vec{\epsilon}'^* \cdot \vec{\epsilon}) / (2M_{\text{N}})$  at zero energy, and so cancel half of the seagull diagram for the correct Thomson limit<sup>13</sup> [6]. This occurs because, in contrast to (a), the photon energy in (b) and (c) flows through the two-nucleon state between emission and absorption, with the (highlighted) intermediate-state propagators of the form in Eq. (5.1):

$$\frac{iM_{\text{N}}}{\omega^2 \pm M_{\text{N}}\omega - \gamma^2 - \vec{q}^2} . \quad (5.4)$$

The (+) sign applies to the diagrams in Fig. 5.1(b) and (c), while the (−) sign applies to the “crossed” graphs. In Regime I,  $M_{\text{N}}\omega \sim \gamma^2 \sim P^2$ , the propagator scales as  $P^{-2}$ , and loop momenta  $q \sim P$  dominate. Intuitively, the initial coherent two-nucleon state is not perturbed very much by photon absorption and propagates coherently on a typical length scale  $1/q \gtrsim 1/m_{\pi}$ , which is larger than the anomalously large NN scattering lengths. Multiple NN interactions are therefore not parametrically suppressed before

<sup>12</sup>Gauge invariance and current conservation are identical in the absence of on-shell photons in loops, as in all Compton calculations to date.

<sup>13</sup>A 0.1% correction from relativistic effects at higher orders replaces  $2M_{\text{N}}$  with the deuteron mass,  $M_{\text{d}} = 2M_{\text{N}} - B_{\text{d}}$ .

another photon is emitted to produce the final deuteron–photon state, and rescattering must be resummed. Power counting bears this picture out. Diagram (c) contributes at LO, just like (a) and (b) in this Regime, since the scattering amplitude of two nucleons close to their mass shell scales as  $T_{\text{NN}} \sim P^{-1}$ , as in any EFT with fine-tuned NN scales [93, 96, 164, 165, 241, 242].

Clearly, the three contributions are of very different computational complexity: (a) is analytically known in the Thomson limit (5.3), irrespective of the deuteron wave function used; (b) contains a convolution of the propagator (5.4) with  $|\Psi_d\rangle$ , which is usually not known in closed form; (c) involves an off-shell rescattering matrix  $T_{\text{NN}}$  and thus depends not only on  $|\Psi_d\rangle$ , but also directly on all NN partial waves and the potential used to generate them. In addition, only the sum of diagrams (b) and (c) is independent of the UV regulator. Since the Thomson limit requires that the sum of the last two must give  $-\frac{1}{2}$  of the seagull, it can be used as a nontrivial check of numerical evaluations. This condition must hold irrespective of the particular potential or wave function chosen and does not even depend on the particle content of the theory. After recent numerical improvements in the  $\chi$ EFT implementation of Hildebrandt et al. [91–93], the cancellation is fulfilled for each helicity amplitude with a relative numerical accuracy of  $\leq 0.01\%$ .

All contributions at NLO ( $P^3$ ) in Regime I are listed in Fig. 5.2, providing a projected relative accuracy of  $(P/\Lambda_\chi)^2 \approx 1/5^2 \approx 4\%$ . For them, the constraint is even more intricate. Since the Thomson

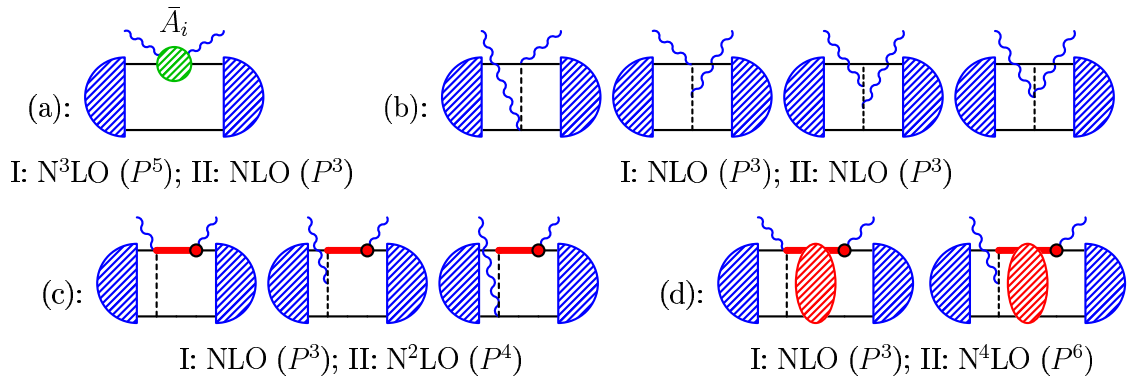


Figure 5.2: (Colour online) Deuteron Compton scattering in Regime I at NLO,  $\mathcal{O}(P^3)$ : one-nucleon structure terms (a); photons coupling to the same pion-exchange currents (b); or to exchange current and nucleon without, (c), and with, (d), rescattering. Crossed and permuted diagrams not displayed.

limit is already fulfilled at LO, all NLO contributions must sum to zero as  $\omega \rightarrow 0$ . Equation (2.11) implies that the one-nucleon structure amplitudes  $\bar{A}_i$  of (a) trivially obey the constraint since they vanish as  $\omega \rightarrow 0$ . In (b), wave functions are convoluted by six-dimensional integrals with an instantaneous meson-exchange current to which the photons couple directly. The other graphs involve convolutions of intermediate-state nucleon propagators without, (c), and with, (d), rescattering amplitudes  $T_{\text{NN}}$  which have to be constructed separately. Fortunately, Arenhövel and Weyrauch demonstrated three decades ago that, while (b), (c) and (d) are individually large and cutoff-dependent, they indeed cancel at  $\omega = 0$  in the sum for any potential and wave function [244, 245]. Since rather different techniques are employed to calculate the different contributions, this provides another nontrivial cross-check. In the  $\chi$ EFT implementation of Hildebrandt et al. [91–93], it holds in each helicity amplitude to a relative accuracy of  $\leq 0.9\%$ . The Thomson limit therefore provides a stringent check on the numerical implementation and the consistent treatment of the potential, the wave function and the NN current operator. Subsequent numerical improvements result in the Thomson limit now being restored to better than 0.2%.

### 5.2.3 Beyond the Thomson limit: reducing rescattering contributions, adding the $\Delta(1232)$

At higher energies,  $\omega \sim P \approx 140$  MeV and  $\sqrt{M_N\omega} \sim P^{\frac{1}{2}}$ , the Thomson limit is not directly significant [96, 199, 222, 241, 242]. The struck nucleon is far off-shell,  $E \sim \sqrt{M_N\omega} \gg q^2, \gamma^2, \omega^2$ , and at LO the intermediate-state propagator (5.4) becomes  $i/\omega$ . The nucleon behaves as if static, and the standard  $\chi$ EFT counting of the one-nucleon sector prevails. Physically, each nucleon propagates incoherently, i.e. as if the other were absent, because its wavelength  $1/q \sim 1/\sqrt{M_N\omega} \approx 1/(360 \text{ MeV})$  is much shorter than the rescattering scale  $1/\gamma \approx 1/(50 \text{ MeV})$ . The struck nucleon has little time to scatter with its partner before the second photon is radiated to restore the coherent final state. Thus, rescattering is suppressed and can be treated perturbatively. This leads to significant computational simplifications and changes the relative importance of many contributions.

The formal power counting, indicated in Figs. 5.1 and 5.2, comes to the same conclusion. The seagull in Fig. 5.1(a) has no two-nucleon intermediate state and thus still scales as  $P^2$ , constituting LO. Since an intermediate-state propagator (Eq. (5.4) and thick lines in Figs. 5.1 and 5.2) now scales only as  $i/\omega \sim P^{-1}$ , each of its occurrences moves a diagram to one order higher. A diagram with one intermediate NN state (but without rescattering, Fig. 5.1(b)) is demoted from LO to NLO ( $P^3$ ) and the diagrams of Fig. 5.2(c) from NLO to N<sup>2</sup>LO ( $P^4$ ). Since  $T_{\text{NN}} \sim P^0$  now, each rescattering in Figs. 5.1(c) and 5.2(d) costs one additional power of  $P$  (c.f. Regime I). In addition, there is one more power of  $P$  than in the Regime I counting of this diagram from each intermediate-state NN propagator that is present. Thus, these two graphs are each demoted by at least  $P^3$ , to order  $P^5$  (N<sup>3</sup>LO) and beyond. On the other hand, the nucleon-structure contributions  $\bar{A}_i$  of Fig. 5.2(a) are enhanced from order  $P^5$  (N<sup>3</sup>LO) in Regime I to order  $P^3$  (NLO) since they scale with  $\omega^2/m_\pi$ , see (2.11) and Section 4.2.2. The meson-exchange diagrams of Fig. 5.2(b) still count as NLO,  $P^3$ . Contributions from loop momenta  $q \sim P^{\frac{1}{2}}$  make the counting proceed in half-integer powers of  $P$  which however only appear beyond NLO.

This implies that, up to N<sup>3</sup>LO corrections, contributions from the off-shell matrices  $T_{\text{NN}}$  of NN rescattering are absent in Regime II. This simplification was first observed by Beane et al. [222] and is crucial to the success of the  $\chi$ EFT deuteron Compton-scattering calculations in Refs. [136, 199, 222]. The Compton amplitude for the deuteron can then be computed as

$$T_{\gamma d} = \langle \Psi_d | [T_{\gamma N} + T_{\gamma \text{NN}}] | \Psi_d \rangle . \quad (5.5)$$

Both contributions are direct convolutions of irreducible photonuclear kernels with deuteron wave functions.  $T_{\gamma N}$  is the single-nucleon Compton amplitude, and  $T_{\gamma \text{NN}}$  the irreducible amplitude for  $\gamma \text{NN} \rightarrow \gamma \text{NN}$ , with all NN interactions truncated after (before) the departure (arrival) of the outgoing (incoming) photon. A complete calculation for  $T_{\gamma N}$  at N<sup>2</sup>LO ( $P^4$ ) therefore consists of only the diagrams of Figs. 5.1(a) and (b) and Fig. 5.2(a), and for  $T_{\gamma \text{NN}}$  consists of the ‘‘exchange current’’ diagrams of Figs. 5.2(b) and (c). For other light nuclei, the only change is to replace the wave function in Eq. (5.5) with that of the target nucleus.

The pioneering work of Beane et al. [222] used all NLO ( $P^3$ ) contributions in Regime II, namely the isoscalar exchange currents of Fig. 5.2(b) and the one-body mechanisms of Figs. 5.1(a) and (b), and 5.2(a) with the single-nucleon  $T_{\gamma N}$  amplitude computed in  $\chi$ EFT without explicit  $\Delta(1232)$  at the matching order,  $\mathcal{O}(P^3)$ . The amplitude is thus complete up to corrections  $\sim (\gamma^2, m_\pi^2)/(M_N\omega)$ , which indicates effects in the amplitude of a few percent at  $\omega = 100$  MeV, increasing to  $\approx 10\%$  at the lower end of the data range. Indeed, agreement with higher-energy data is good, but the 49 MeV data of Lucas [25] are significantly overestimated; see Fig. 5.3. The two-body currents due to Compton scattering from one-pion exchange turned out to be sizable at all energies and are crucial to reasonably describe all of the data.

Subsequently, Beane et al. fitted the scalar nucleon polarisabilities from deuteron data [198, 199]. They extended the calculation to N<sup>2</sup>LO by incorporating the  $P^4$  mechanisms for single-nucleon scatter-

ing discussed in Section 4.2 and the two-body mechanisms of Fig. 5.2(c). At this order, these two-body diagrams are indeed *all* contributions to  $T_{\gamma NN}$  with one vertex from  $\mathcal{L}_{\pi N}^{(2)}$  and one from  $\mathcal{L}_{\pi N}^{(1)}$ .

Neither implementation included the effects of an explicit  $\Delta(1232)$  degree of freedom. As discussed in Section 4.2.6, the  $\Delta$  contributes substantially in the one-nucleon sector, in particular at backward angles for  $\omega \gtrsim 100$  MeV due to the rise of  $\beta_{M1}$  to about four times its static value. It would therefore be expected to have a similarly large effect in the deuteron, in particular for Hornidge’s SAL data at  $\omega_{\text{lab}} = 94.5$  MeV [26]. Except in the one-nucleon amplitude itself, no new contributions arise with a dynamical  $\Delta$ . Since the deuteron is isoscalar, there is no  $\Delta N$  component in its wave function. The dynamical  $\Delta\Delta$  component is strongly suppressed below  $\omega \sim 2\Delta_M$ . No explicit  $\Delta$  appears in intermediate-nucleon graphs analogous to Figs. 5.1(b,c) and 5.2(c,d), or in two-body currents similar to Fig. 5.2(b). The two-nucleon part at order  $P^3$  (NLO) in the  $\Delta$ -less theory is thus identical to the one at orders  $\epsilon^3$  and  $e^2\delta^3$  with explicit  $\Delta$ . We continue to use  $P$  to parameterise contributions of the two-nucleon sector for the variants with or without an explicit  $\Delta$ , and to indicate the counting of the single-nucleon amplitudes embedded in Fig. 5.2(a) separately. Recall that for diagrams with only pions and nucleons, the three power countings translate as  $P^n \sim \epsilon^n \sim e^2\delta^{2n-4}$ , see Sections 4.2.6 to 4.2.8.

To summarise, an explicit  $\Delta(1232)$  does not appear in the two-nucleon contributions until high orders, and one can therefore insert any of the three versions in Section 4.2 for the single-nucleon contributions: without a dynamical  $\Delta(1232)$  at  $\mathcal{O}(P^4)$ ; with explicit  $\Delta$  at  $\mathcal{O}(\epsilon^3)$ , modified by adding the LECs  $\delta\alpha_{E1}^{(s)}$ ,  $\delta\beta_{M1}^{(s)}$ ; and with even more pion-nucleon loops at  $\mathcal{O}(e^2\delta^4)$ . Since the two-nucleon sector must be treated to the same order, the latter case warrants including the two-nucleon contributions of Fig. 5.2(c). As discussed in Section 4.2, a single-nucleon calculation at order  $\epsilon^3$  is actually equivalent to one at order  $e^2\delta^3$  for  $\omega \sim m_\pi$ , i.e. over the whole energy range of Regimes I and II. The proton fit above used the resummed, covariant  $\Delta$  propagator, but that is not necessary here. All published deuteron data lie below the pion-production threshold, so we can treat the nonzero  $\Delta$  width and relativistic effects perturbatively and consider corrections for the pion-threshold position to be negligible [92, 136], in contrast to the single-nucleon case in Section 4.2.

Hildebrandt et al. performed such a NLO calculation in Regime II, with a dynamical  $\Delta(1232)$  at modified order  $\epsilon^3$  [136]. The total accuracy is  $\epsilon^2$  relative to LO, i.e. N<sup>2</sup>LO, as the first order in which not all contributions are consistently retained in both the one- and two-nucleon sectors. The formulation does not improve the accuracy found by Beane et al. [222] at lower energies, but it markedly improves the agreement with Hornidge’s SAL data [26]; cf. discussion of Fig. 5.3 below.

## 5.2.4 A unified description of Regimes I and II

The deuteron database covers 49 to 95 MeV, i.e. energies that overlap both Regimes I and II. An accuracy better than 10% necessary for a meaningful extraction of nucleon polarisabilities can therefore only be achieved if one incorporates *all* the effects which are LO or NLO in either Regime I or Regime II, as well as the energy dependence of the  $\Delta(1232)$  at  $e^2\delta^3 \sim \epsilon^3$  (modified) that so prominently affects  $\beta_{M1}(\omega)$ . This guarantees both the correct Thomson limit and an accurate description at higher energy.

This was achieved by Hildebrandt et al. [91–93]. Combining the discussions of Regime I and II above, we see that when all diagrams of Figs. 5.1 and 5.2 are included, one actually performs a calculation which is complete for the two-nucleon sector up to N<sup>2</sup>LO ( $P^4$ ) corrections in both Regimes simultaneously and can move smoothly between them. In Regime I, the only higher-order diagram is the nucleon-structure contribution of Fig. 5.2(a). In Regime II, one includes all corrections at N<sup>2</sup>LO (Fig. 5.2(c)) as well as several higher-order contributions, as in Figs. 5.1(c) and 5.2(d). In each Regime, the accuracy of the two-nucleon diagrams is still set by the last order for which all terms are included, namely  $P^3$  in Regime I and  $P^4$  in Regime II. The accuracy of the single-nucleon sector must match and thus can at most include all diagrams at orders  $P^4$  without explicit  $\Delta(1232)$ , or, with it,  $\epsilon^3$  and  $e^2\delta^4$ , respectively.

One may wonder about the predicted decrease in accuracy at lower energies, where an EFT descrip-

tion is supposed to be better. However, since the Thomson limit is already fulfilled at LO, higher-order corrections approach zero order-by-order as  $\omega$  is decreased. The relative size of the total NLO correction is thus not given by  $P$  at low energies, but rather is proportional to  $P$  multiplied by powers of  $\omega$ . As the importance of the Thomson limit decreases in Regime II, the relative size approaches  $P$ .

It is this formulation which we will use to extract the isoscalar electric and magnetic dipole polarisabilities from all deuteron data in Section 5.3. Since isovector polarisabilities enter only at higher orders in  $\chi$ EFT, agreement with deuteron data should be good when the isoscalar amplitudes obtained in a proton fit are inserted into the deuteron calculation, which is then parameter-free. This is confirmed in the following discussion.

First, we assess the transition between Regimes I and II. Figure 5.3 compares two otherwise identical calculations in  $\chi$ EFT with a dynamical  $\Delta(1232)$  at order  $e^2\delta^3 \sim \epsilon^3$  (both modified) [91, 92] with the same static scalar polarisabilities of Eq. 4.13. The first takes the unified approach; the other follows

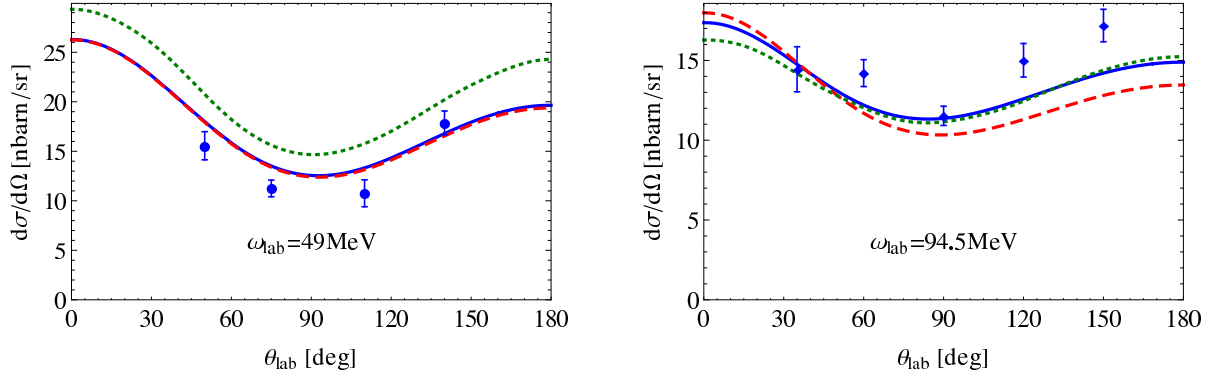


Figure 5.3: (Colour online) Comparison of the deuteron data at 49 and 94.5 MeV with  $\chi$ EFT predictions (data key in Table 3.2). Solid (blue): with both dynamical  $\Delta(1232)$  and rescattering (“unified approach”, modified order  $\epsilon^3 \sim e^2\delta^3$ ); dotted (green): with  $\Delta(1232)$ , but without rescattering (strict Regime II counting); dashed (red): without dynamical  $\Delta(1232)$ , but with rescattering (“unified”  $\mathcal{O}(P^3)$ ). Static scalar polarisabilities are always set at the  $\mathcal{O}(P^3)$  values:  $\alpha_{E1}^{(s)} = 10\beta_{M1}^{(s)} = 12.5$ .

Refs. [136, 222] for strict Regime II counting at NLO, using only (5.5) and no rescattering. The results indeed converge to each other with increasing  $\omega$  as claimed by Beane et al. [222], but the calculation with the correct Thomson limit clearly provides a better description of the data at  $\omega_{\text{lab}} = 49$  MeV. In the strict Regime II calculation, corrections from higher orders in  $(\gamma^2, m_\pi^2)/(M_N\omega)$  (including rescattering) increase dramatically as the deuteron breakup at  $\omega_{\text{cm}} = B_d$  is approached from above, as also seen in Fig. 5.4. Comparison with Fig. 4.9 shows that the deuteron and proton results are of similar size for  $\gtrsim 70$  MeV. The angular distribution becomes quickly skewed: forward scattering becomes weaker than backward scattering for  $\omega_{\text{cm}} \gtrsim 80$  MeV, and weaker than even the  $90^\circ$  cross section above 100 MeV.

Of course, this is exactly the effect of the  $\Delta(1232)$  discussed above. In Fig. 5.3, we compare the deuteron data to the parameter-free predictions of the unified calculation with two variants of the single-nucleon amplitudes which produce the static polarisabilities of Eq. (4.13): without a dynamical  $\Delta$  at order  $P^3$ , and with an explicit  $\Delta$  at order  $e^2\delta^3 \sim \epsilon^3$  (modified). The results are depicted in Fig. 5.3 for the lowest- and highest-energy deuteron data. At low energies, including the  $\Delta$  as a dynamical degree of freedom has no significant effect, and either variant agrees well with the data, as required by the decoupling theorem. With increasing energy, however, effects of the  $\Delta$  are particularly important to match the angular dependence of Hornidge’s SAL backward-angle data at 94.5 MeV [26]. As mentioned in Section 5.2.3, this was first demonstrated in the variant without rescattering contributions by Hildebrandt et al. [92, 136]. Indeed, the strong energy dependence from the  $\Delta$  excitation helps resolve the discrepancy between these data and earlier calculations in both  $\chi$ EFT (Section 5.2.3) or models (Section 5.5 below). An alternative remedy is to exclude the two backward-angle points since



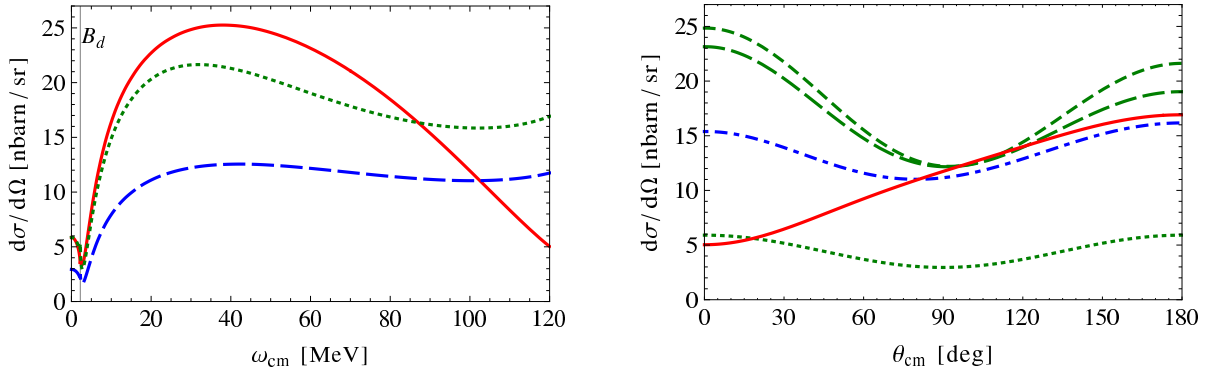


Figure 5.4: (Colour online) Energy and angle dependence of unpolarised deuteron Compton scattering in the centre-of-mass frame in the unified approach of  $\chi$ EFT with explicit  $\Delta(1232)$  and the static scalar polarisabilities set to the  $\mathcal{O}(P^3)$  values  $\alpha_{E1}^{(s)} = 10\beta_{M1}^{(s)} = 12.5$ ; see Eq. (4.13). Left: at  $\theta_{\text{cm}} = 0^\circ$  (solid red line),  $90^\circ$  (dashed blue),  $180^\circ$  (dotted green). Right: at the Thomson limit (dotted green),  $\omega_{\text{cm}} = 30$  MeV (short-dashed green), 60 MeV (long-dashed green), 90 MeV (dash-dotted blue), 120 MeV (solid red).

they correspond to a momentum transfer beyond  $\chi$ EFT without explicit  $\Delta(1232)$  even at  $\mathcal{O}(P^4)$ , as described in Section 4.2.8 [198, 199].

For the rest of this section, we address some more technical issues of this approach [91–93]. Quite different numerical implementations were merged. The Compton amplitudes involving the one- and two-nucleon kernels  $T_{\gamma N}$  and  $T_{\gamma NN}$  of Eq. (5.5) are numerically evaluated as three- and six-dimensional integrals, respectively, against the deuteron wave function, following Beane et al. [222]. The two-nucleon-reducible contributions may be represented in the form:

$$\epsilon_i \langle \Psi_d | \left[ \mathbf{J}_i G(-B_d + \omega) \mathbf{J}_j^\dagger + \mathbf{J}_j^\dagger G(-B_d - \omega) \mathbf{J}_i \right] | \Psi_d \rangle \epsilon_j . \quad (5.6)$$

The second term represents the crossed diagrams not shown in Figs. 5.1(b) and (c) and 5.2(c) and (d).  $\mathbf{J}$  denotes the NN current operator including mesonic currents and  $G$  is the (interacting) NN Green’s function, i.e. the off-shell  $S$ -matrix of the NN system. Therefore, Eq. (5.6) includes both free propagation of the NN pair and rescattering via  $T_{NN}$ . It is constructed in coordinate space following Arenhövel et al. [244, 245, 252]; cf. [253, Chapter 3.7.1] and the particularly clear presentation by Karakowski [249]. The fact that the cross section at the Thomson limit is now obtained to better than 0.2% accuracy [93] when the three contributions are combined provides a nontrivial check.

Besides providing a unified framework for energies from the Thomson limit to the pion-production threshold, a crucial benefit of keeping higher-order rescattering diagrams even in Regime II is that they also considerably reduce the dependence on the deuteron wave function; see Fig. 5.5. For the counting which is valid only in Regime II, Beane et al. had established that the dependence of the cross-section predictions on the NN wave function amounts to about 10% at 94.5 MeV at NLO [222]. The effect is not diminished at N<sup>2</sup>LO ( $P^4$ ), as they subsequently demonstrated in Ref. [199] using wave functions calculated from a variety of NN potentials based on  $\chi$ EFT [254, 255]. Since all deuteron wave functions share the same long-distance physics, the variability is associated with differences in the short-distance physics of the photon–deuteron interaction. This is largely independent of angle and represents an irreducible theoretical uncertainty of calculations that strictly employ the Regime II power counting, severely compromising the accuracy with which  $\alpha_{E1}^{(s)}$  could be extracted from the deuteron data [199]. However, as discussed in Section 5.2.2, the Thomson limit dictates wave-function independence as  $\omega \rightarrow 0$ . Figure 5.5 shows that with the zero-energy point thus fixed, the dependence is reduced even at 100 MeV from about  $\pm 5\%$  to  $\lesssim \pm 0.5\%$ , and is therefore virtually eliminated in the

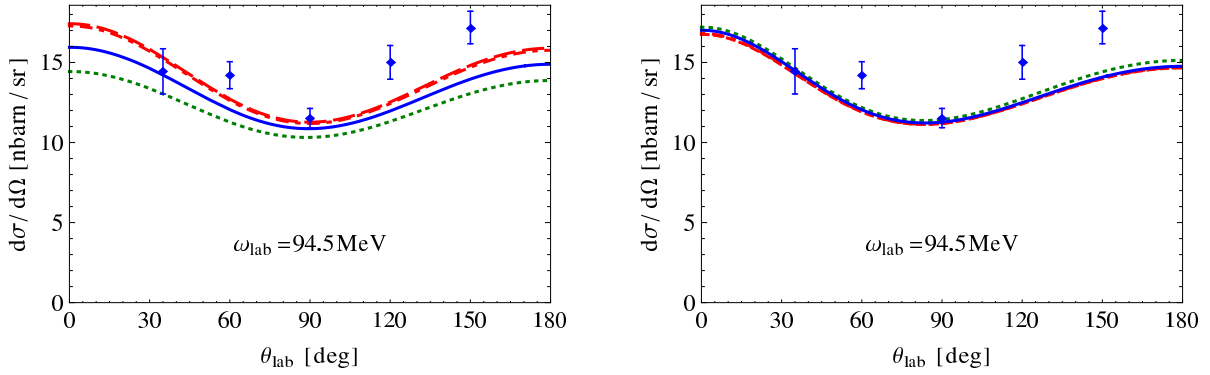


Figure 5.5: (Colour online) Unpolarised deuteron Compton cross section and data [26] at high energies without (left) and with (right) rescattering effects in NLO  $\chi$ EFT with explicit  $\Delta(1232)$ , using the static scalar values from Eq. (4.13). Deuteron wave functions:  $\chi$ EFT at N<sup>2</sup>LO (cutoff 650 MeV, identical to Fig. 5.3; blue solid) and NLO (cutoff 600 MeV with  $B_d = 2.175$  MeV, green dotted) [254]; AV18 (red dot-dashed) [256]; Nijmegen 93 (red dashed) [257].

experimentally relevant energy range [91, 92]. Therefore, a wave function derived from any modern, “high-precision” potential can be used.

The dependence on the choice of NN potential could still be of importance when the partial waves which enter rescattering in the NN intermediate state are computed. However, Hildebrandt et al. [91, 92] compared rescattering contributions derived from the AV18 potential [256] with those from a rather crude LO  $\chi$ EFT potential [258]. They found that nearly perfect agreement at the Thomson limit still resulted, and there was only a  $\lesssim 4\%$  deviation at 90 MeV.

Hildebrandt et al. [91–93] also combined one “high-order chiral” or “high-precision traditional” potential for rescattering with a deuteron wave function generated by another potential. These apparent mismatches did not affect the degree to which the Thomson limit is restored, nor did they show significant differences in a variety of unpolarised and polarised observables at  $\lesssim 100$  MeV. This is an excellent test for independence from details of different short-distance physics and implies that issues of matching electromagnetic currents with both the wave function and the potential can be neglected. Indeed, such effects related to gauge invariance only appear two orders higher than considered here.

All of this suggests that cross sections and polarisabilities in the present approach will be essentially unchanged once a fully systematic  $\chi$ EFT is established which is cutoff-independent over a wide range of cutoffs and has a strict perturbative expansion. The use of Weinberg’s power counting for the NN potential and NN operators yields results which should differ from the result in this full theory by only a small amount, thanks largely to the stringent constraint imposed by the Thomson limit.

### 5.3 A new fit to the deuteron data

We now use the  $\chi$ EFT variant from Section 5.2.4, which is valid from the Thomson limit to the pion production threshold, for a new extraction of the isoscalar electric and magnetic dipole polarisabilities from the available deuteron Compton scattering data: Lucas (Illinois) [25], Hornidge (SAL) [26] and Lundin (MAX-Lab) [27]. Comparisons to the static values for the proton will then allow us to assess whether isovector (scalar dipole) polarisabilities are indeed small, as predicted by  $\chi$ EFT. However, first we recall the conclusion of Section 3.4 that the deuteron data are not as refined as the proton data, cf. Table 3.2. Limited angle and energy coverage, as well as difficulties in cleanly differentiating elastic and inelastic events, gives rise to large statistical and systematic errors. It therefore comes as no surprise that the experimental errors are at least as large as the residual theoretical uncertainties in extractions of the polarisabilities [91, 92, 136, 198, 199]. This is confirmed by our re-analysis.

We present an update of the deuteron results by Hildebrandt et al. [91, 92]. As discussed in Sections 5.2.3 and 5.2.4, it actually represents a complete (modified)  $\mathcal{O}(e^2\delta^3)$  calculation in both the two- and one-nucleon sectors, valid from the Thomson limit up to  $\omega \sim m_\pi$ . All two-nucleon contributions are included which enter at this order in either Regime I or II, Figs. 5.1 and 5.2. The single-nucleon sector diagrams are listed in Figs. 4.2, 4.3 and 4.5. They contain the two short-distance coefficients  $\delta\alpha_{E1}^{(s)}$  and  $\delta\beta_{M1}^{(s)}$  (last graph of Fig. 4.4), which, strictly speaking, only enter at order  $e^2\delta^4$ . They also include the  $\Delta(1232)$ , but in the deuteron calculation it is treated nonrelativistically and without a width, as described in Section 4.2.6. With one exception all parameters are the same as for the proton fit, including the  $\Delta$  parameters  $\Delta_M = 293$  MeV,  $g_{\pi N\Delta} = 1.425$ . The exception is the  $\gamma N\Delta$  coupling for which we use the translation to the nonrelativistic value  $b_1 = 5$ , as explained in Section 4.2.8. This treatment of the  $\Delta(1232)$  is justified by the excellent agreement with the relativistic, nonzero-width approach in the region of the deuteron data,  $\omega_{\text{lab}} \lesssim 100$  MeV; see the comparison of the energy dependence of the polarisabilities in the two approaches in Fig. 4.7. The final fits are insensitive to varying the value of  $b_1$  by as much as 5%. In practice, we use the  $\chi$ EFT deuteron wave function at N<sup>2</sup>LO (cutoff 650 MeV) in the implementation of Epelbaum et al. [254] and the AV18 potential [256] for NN rescattering. As discussed in Section 5.2.4, this combination provides an adequate  $\chi$ EFT representation of the two-nucleon system and the residual dependence on the deuteron wave function, NN potential and numerical implementation is minuscule. These parameters are also used in Figs. 5.3 to 5.5 and 5.7.

The presentation here differs from that of Hildebrandt et al. [91, 92] in the following: a new parameter set ( $b_1$ ,  $g_{\pi N\Delta}$ ,  $\Delta_M$ ) for the  $\Delta(1232)$  from the Breit-Wigner parameters and the proton Compton data, and not from the pole position; a more careful analysis of systematic errors and summation of statistical and point-to-point systematic errors in quadrature, as discussed in Section 3.4; an implementation of correlated systematic errors of the experiments by a floating normalisation as in the proton case (4.19); and small technical improvements to implement the Thomson limit and increase numerical accuracy, see Section 5.2.2. However, the relatively large experimental errors make the fit rather insensitive to the procedure used, and so none of these changes substantially alters the conclusions of Refs. [91, 92].

As in the proton case, the fractional error in the extracted polarisabilities is  $\delta^2$ , namely one order past the last one for which all contributions are consistently retained in both the one- and two-nucleon sectors. Up to higher-order corrections, the results should also agree with those of the version without rescattering but with a dynamical  $\Delta(1232)$ , fitted in Regime II,  $\omega \sim m_\pi$ . Refs. [92, 136] performed fits of  $\alpha_{E1}^{(s)}$  and  $\beta_{M1}^{(s)}$  to the same data without rescattering. However, the assumption  $\omega \sim m_\pi$  fails at the lower end of the data, as demonstrated in Fig. 5.3, and the residual wave-function dependence of the extracted values is rather large, namely  $\pm 1$ , cf. Fig. 5.5. Therefore, we do not use this criterion to estimate higher-order corrections, even though we note that our final values given below agree with theirs within error bars. Ultimately, higher-order effects in the chiral amplitudes at order  $e^2\delta^4$  and beyond provide by far the largest residual uncertainty, estimated at  $\pm 0.8$ . As in Section 4.4, this estimate is justified by assuming that the uncertainty is of order  $\delta^1$  of the LO-to-NLO correction; c.f. also [136].

With the anticipated accuracy established, the isoscalar spin-independent polarisabilities read:

$$\alpha_{E1}^{(s)} = 10.5 \pm 2.0(\text{stat}) \pm 0.8(\text{theory}) \quad , \quad \beta_{M1}^{(s)} = 3.6 \pm 1.0(\text{stat}) \pm 0.8(\text{theory}) \quad (5.7)$$

from a  $\chi^2$  fit, with the corresponding cross sections shown in Fig. 5.6. As before, the statistical error is determined from the projection of the  $\chi_{\text{min}}^2 + 1$  contours onto the  $\alpha_{E1}^{(s)}$  and  $\beta_{M1}^{(s)}$  axes. For 29 data points and 5 free parameters, one finds a total  $\chi^2 = 24.3$ , or 1.01 per degree of freedom. The small differences compared to the results reported in Refs. [91, 92],  $\alpha_{E1}^{(s)} = 11.5 \pm 1.4(\text{stat}) \pm 1(\text{theory})$  and  $\beta_{M1}^{(s)} = 3.4 \pm 1.6(\text{stat}) \pm 1(\text{theory})$ , are well within statistical uncertainties and stem from the minor differences discussed above. The collective data set appears consistent since each experiment contributes about equally to the overall  $\chi^2$ , and the extracted parameters remain nearly unchanged when one data set is eliminated. This confirms the assessment in Section 5.2.4 that the angular dependence of

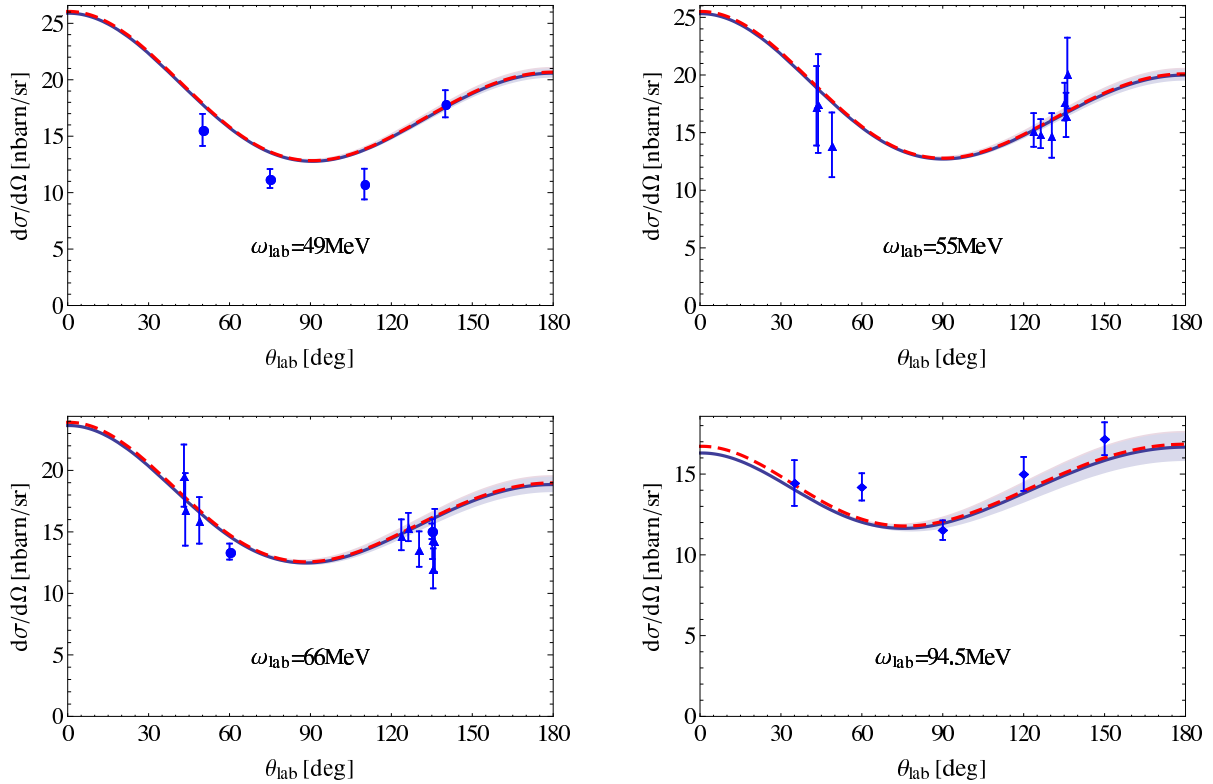


Figure 5.6: (Colour online) Cross sections in the two-parameter (dashed) and one-parameter (solid) determinations of the isoscalar spin-independent dipole polarisabilities. Bands: statistical error of the one-parameter fit. Data symbols from Table 3.2, statistical errors only.

Hornidge’s SAL data is described well by the theory. The floating normalisation of that set is about 10% lower than the other two, which in turn both have a floating normalisation close to 1. All floating normalisations are thus compatible with the correlated systematic uncertainties (3% for Lucas, 5% for Hornidge, 7.5% for Lundin) stated in Section 3.4. Only more accurate experiments, such as those ongoing at MAX-Lab [138, 139], can reveal if the lower normalisation of the Hornidge data is more than a statistical accident.

The results (5.7) are in good agreement with the proton values, confirming that isovector effects in  $\alpha_{E1}$  and  $\beta_{M1}$  are indeed small. They also add up, within error bars, to the isoscalar Baldin sum rule,  $\alpha_{E1}^{(s)} + \beta_{M1}^{(s)} = 14.5 \pm 0.3$ , Eq. (2.9). One can therefore use the Baldin constraint to reduce statistical uncertainties in a one-parameter fit for  $\alpha_{E1}^{(s)} - \beta_{M1}^{(s)} = 7.3 \pm 1.8(\text{stat}) \pm 0.8(\text{theory})$ , thereby obtaining very similar results with about half the statistical error:

$$\begin{aligned}
 \alpha_{E1}^{(s)} &= 10.9 \pm 0.9(\text{stat}) \pm 0.2(\text{Baldin}) \pm 0.8(\text{theory}) \\
 \beta_{M1}^{(s)} &= 3.6 \mp 0.9(\text{stat}) \pm 0.2(\text{Baldin}) \pm 0.8(\text{theory})
 \end{aligned}
 \tag{5.8}$$

The total  $\chi^2$  is unchanged, but drops to 0.97 per degree of freedom since the number of degrees of freedom is increased to 25. The cross sections of this fit, shown in Fig. 5.6, also compare well with both the two-parameter fit and the data. Extractions including a dynamical  $\Delta(1232)$  [91, 92] lead to systematically higher values for  $\beta_{M1}^{(s)}$  than those without it [198, 199], since the enhancement in the Hornidge (SAL) data at backward angles must be compensated in the latter case by decreasing  $\alpha_{E1}^{(s)} - \beta_{M1}^{(s)}$ , cf. Section 5.2.4. In addition, agreement with the Baldin sum rule was marginal in Refs. [198, 199].

Comparing with the results of Section 4.4, we see that the static polarisabilities of the proton, (4.20) and (4.21), and isoscalar nucleon, (5.7) and (5.8), are identical within error bars. They may thus be

combined to obtain the neutron polarisabilities in the two-parameter analysis as

$$\alpha_{E1}^{(n)} = 10.5 \pm 4.0(\text{stat}) \pm 0.8(\text{theory}) \quad , \quad \beta_{M1}^{(n)} = 4.4 \pm 2.1(\text{stat}) \pm 0.8(\text{theory}) \quad , \quad (5.9)$$

and in the one-parameter fit using the Baldin sum rule as  $\alpha_{E1}^{(n)} - \beta_{M1}^{(n)} = 7.0 \pm 3.6(\text{stat}) \pm 0.8(\text{theory})$ ,

$$\begin{aligned} \alpha_{E1}^{(n)} &= 11.1 \pm 1.8(\text{stat}) \pm 0.4(\text{Baldin}) \pm 0.8(\text{theory}) \\ \beta_{M1}^{(n)} &= 4.1 \mp 1.8(\text{stat}) \pm 0.4(\text{Baldin}) \pm 0.8(\text{theory}) \end{aligned} \quad (5.10)$$

with statistical errors added in quadrature. These results are in good agreement with those of the quasi-free experiments [68], while having somewhat smaller uncertainties. We note again that the proton results were obtained in a slightly different  $\chi$ EFT variant, in which  $\Delta(1232)$  propagation is treated relativistically and its width is included non-perturbatively. However, since the omitted terms are of higher order and therefore parametrically small, the two variants must agree within the theoretical uncertainties; cf. Fig. 4.7. In turn, comparing proton and isoscalar results confirms that the scalar dipole polarisabilities of the proton and neutron are largely isoscalar, i.e. that both share essentially the same two-photon response. It is curious to note that the proton-neutron difference of the magnetic polarisability appears to have a statistically insignificant tendency to be slightly negative,  $\beta_{M1}^{(v)} \approx -1 \pm 2$ , in line with a recent constraint from its contribution to the electromagnetic self-energy of the proton-neutron mass difference [18].

Finally, smaller theoretical uncertainties are expected from a fully consistent extraction of order  $e^2\delta^4$  which is under way and uses the same variant to the same order for both the proton and deuteron data, plus chirally-consistent interactions throughout [137]. Higher-quality data with carefully formulated correlated and point-to-point systematic errors would reduce the sizable statistical error.

## 5.4 EFTs for very low energies

### 5.4.1 Compton scattering without pions

Since  $\omega \ll m_\pi$  in Regime I, a photon cannot resolve details of pion-cloud effects and one can formulate a more radical EFT by integrating out the pion into contact interactions amongst nucleons and with photons. This is the low-energy version of  $\chi$ EFT, called “pion-less” EFT (EFT( $\not{\pi}$ )). Its typical momentum scale is  $\gamma \approx 50$  MeV; its breakdown scale  $\Lambda_{\not{\pi}} \sim m_\pi$  is set by the mass of the pion as the lightest particle not included as a dynamical degree of freedom; and its expansion parameter is  $Q_{\not{\pi}} \equiv \gamma/\Lambda_{\not{\pi}}$ . The lack of finite-range forces considerably simplifies calculations, which can be carried out to high orders with relative ease, and indeed analytic results are common. This EFT has been used for model-independent subtractions of “nuclear effects” and predictions in a variety of very low-energy processes, also with electro-weak probes; see e.g. [164, 165, 259, 260] for reviews. In such calculations, the expansion parameter is established as being in the range  $Q_{\not{\pi}} \approx 1/3$  to  $1/5$  for  $p_{\text{typ}} \sim \gamma$ , and accuracy of better than 1% has been achieved. Since gauge invariance and LETs such as the Thomson limit are automatically fulfilled exactly, one can check the numerics of  $\chi$ EFT. Indeed, any consistent theoretical framework, whatever its detailed treatment of meson-exchange currents, “off-shell effects”, cutoff dependence, etc., must agree with the EFT( $\not{\pi}$ ) result within the mutual accuracies at energies where EFT( $\not{\pi}$ ) is applicable. EFT( $\not{\pi}$ ) is thus a theoretically rigorous yet numerically simple tool to study reactions at very low energies.

For NN scattering, the theory is equivalent to Bethe’s Effective Range Expansion of the  $^1S_0$  and  $^3S_1$  channels [51–55], and at NLO in  $Q_{\not{\pi}}$ , the scattering lengths and effective ranges are the only LECs. In the latter, momentum-dependent NN couplings also give rise to photon couplings by minimal substitution.

A particularly compact NLO two-nucleon Lagrangian is given in Refs. [261, 262]. At this order,  $^3S_1$ - $^3D_1$  mixing is still absent, and the deuteron is a pure S-state. Since contributions with two isovector



magnetic-moment interactions are relatively large, they have typically been promoted by one order,  $(\kappa^{(v)})^2 \approx 5.5 \sim Q_{\not{\pi}}^{-1}$  [220–222].

In the one-nucleon sector, the NLO terms relevant for Compton scattering are identical to those in  $\chi$ EFT with all pion-nucleon couplings set to zero, and lead to the Petrun'kin amplitudes (2.5). The photons couple to a point-like nucleon with spin and anomalous magnetic moment, and structure effects enter through the photon-nucleon seagull terms of the effective Lagrangian (2.10). As discussed there, only the static polarisabilities are relevant for  $\omega \ll \Lambda_{\not{\pi}}$  (2.13). At the same order, the relevant two-nucleon diagrams are just those in which one or both photons couple to the “effective range” NN contact terms.

EFT( $\not{\pi}$ ) is applicable in all of Regime I ( $\omega \lesssim 20$  MeV). In that range, one can again count the photon energy as either soft or hard, but now relative to the low scale  $\gamma$  [220, 221, 263]. When  $\omega \lesssim 3$  MeV  $\sim B_d = \gamma^2/M_N \sim Q_{\not{\pi}}^2$  is counted as soft, the photon wavelength is larger than the deuteron size, and the photon energy may barely be sufficient to disintegrate it. This is the region of the very first Compton-scattering calculation on a composite nuclear system, by Bethe and Peierls in 1935 [4]. Here, one tests the stiffness of the deuteron as a whole against deformation in the photon field, parameterised by the electric and magnetic scalar and tensor polarisabilities of the *deuteron*. Tensor polarisabilities probe the deformation of its quadrupole component. Closed-form expressions exist for each, often to high orders. Since it can be shown that the polarisabilities of the individual nucleons only enter at the  $\lesssim 0.1\%$  level [263, 264], we do not describe these in more detail here but refer to the original literature [164, 220, 265–267] and mention that these parameter-free predictions usually agree very well with other theoretical and experimental determinations [268–272].

At higher energies, the photon wavelength is comparable to the deuteron size, and  $\omega \sim \gamma \sim Q_{\not{\pi}}$  is counted as hard. However, the expansion is only justified if the hard scale in the intermediate-state propagator is also small compared to the breakdown scale,  $M_N \omega \lesssim m_\pi^2$ , i.e.  $\omega \lesssim 20$  MeV as in Regime I of  $\chi$ EFT. The nucleon polarisabilities then enter because of their  $\omega^2$  dependence, in principle as  $Q_{\not{\pi}}^2 \sim 10\%$  corrections, i.e. at N<sup>2</sup>LO. To this order, this region was studied in EFT( $\not{\pi}$ ), with a projected accuracy of order  $Q_{\not{\pi}} \sim 30\%$  for  $\alpha_{E1}^{(s)}$  and  $\beta_{M1}^{(s)}$  [221, 263, 264, 273]. As the energy increases, the relative importance of each contribution changes. While partial-wave mixing is still absent at N<sup>2</sup>LO, two new short-distance NN effects enter. The first one couples the  $^1S_0$  and  $^3S_1$  waves by a spin-flipping magnetic photon, with its LEC  $L_1$  determined by  $np \rightarrow d\gamma$  at thermal energies. In addition, Chen et al. [273] pointed out the importance of a seagull term from the relativistic correction to the nucleon magnetic-moment interaction, i.e. from the spin-orbit coupling. On top of the scalar amplitudes analogous to  $A_{1,2}$ , they also noted that vector amplitudes dependent on the deuteron spin and analogous to  $A_{3,6}$  appear at N<sup>2</sup>LO and contribute about 20% at these energies. At leading nonvanishing order, they receive contributions from the magnetic moment, spin-orbit coupling and  $L_1$ , and add about 4 nb/sr to the backward cross section at  $\omega = 50$  MeV. Since all three are magnetic, spin-flip effects, they are most prominent in backward-angle scattering and thus can mimic a false signal of the combination  $\alpha_{E1}^{(s)} - \beta_{M1}^{(s)}$ .

In Fig. 5.7 the data at  $\omega_{\text{lab}} = 49$  and 55 MeV are compared to the cross section of two EFT( $\not{\pi}$ ) variants which differ only by higher-order contributions and thus map out a band whose width of  $\approx 5\%$  may indicate a typical theoretical uncertainty at N<sup>2</sup>LO [273]. However, the formal expansion parameter  $\sim \sqrt{M_N \omega}/m_\pi \approx 1.5$  at these energies suggests non-convergence even for the lowest-energy data set at 49 MeV. In addition, in EFT( $\not{\pi}$ ) the deuteron is still a pure S-wave state at this order, the tensor components of the Compton amplitude are zero, and rescattering through higher NN partial waves is absent. Since all of these effects add to the cross section and are well described by pion-exchange contributions, it is no surprise that EFT( $\not{\pi}$ ) misses overall strength compared to the  $\chi$ EFT version. The lack of the deuteron tensor component and of rescattering is most prominent at forward angles where the  $\chi$ EFT result is up to 20% higher than EFT( $\not{\pi}$ ), while both agree within errors at backward angles.

Nonetheless, this breakdown should be gradual, not catastrophic, so that EFT( $\not{\pi}$ ) may serve for

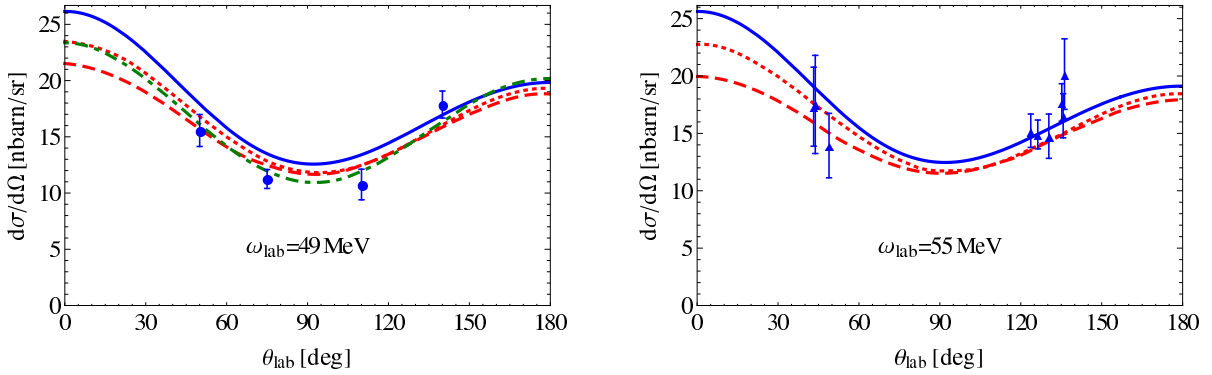


Figure 5.7: (Colour online) Deuteron Compton scattering in  $EFT(\pi)$  and  $\chi EFT$ , compared with data at 49 and 55 MeV in the lab frame (symbols from Table 3.2, stat. errors only). Solid (blue) line: NLO  $\chi EFT$  with dynamical  $\Delta(1232)$  and rescattering [91–93]; dashed/dotted (red):  $N^2LO EFT(\pi)$  with resummed/perturbative effective-range corrections [273]; dash-dotted (green):  $\chi EFT$  in the KSW scheme with perturbative pions at NLO [221] (left panel only). All calculations use the static scalar polarisabilities (4.13) and are rescaled to the flux factor (2.17).

qualitative explorations [263]. Indeed, Chen et al. fitted the scalar polarisabilities at  $N^2LO$  to data at 49 and 55 MeV as  $\alpha_{E1}^{(s)} = 12.3 \pm 1.4$ ,  $\beta_{M1}^{(s)} = 5.0 \pm 1.6$ , and  $\alpha_{E1}^{(s)} = 14.2 \pm 2.1$ ,  $\beta_{M1}^{(s)} = 9.3 \pm 2.5$  (statistical errors only) in two variants which should differ by higher-order terms [273]. The difference is again an indicator of systematic uncertainties, but the rather large values and disagreement with the isoscalar Baldin sum rule (2.9) reflect the fact that the fit must also mock up the physics not captured in  $EFT(\pi)$  at this order. Extractions in  $EFT(\pi)$  are thus not reliable for the current data, but the relative sensitivity of observables to the polarisabilities may be captured. For example, Chen et al. studied the double-polarisation observables  $\Sigma_{x/z}^{circ}$  (2.25) and the beam asymmetry  $\Sigma_3$  (2.23) on a vector-polarised deuteron to  $N^2LO$  [97]. Parallel results in  $\chi EFT$  [71, 93, 101, 274] will be discussed in Section 6.

Can nucleon polarisabilities be extracted instead from high-accuracy data inside the formal radius of convergence of  $EFT(\pi)$ ,  $\omega \lesssim 20$  MeV? No data exist, but  $HI\gamma S$  can provide the high beam intensity for cross sections at  $\lesssim 10\%$  (i.e.  $N^2LO$ ) accuracy needed for polarisabilities with 30% errors [99]. Unfortunately, this is not competitive with the accuracy of  $\chi EFT$  at higher energies, where signals from nucleon polarisabilities are much stronger; see Section 5.2.3. An attempt to decrease the error by an  $N^3LO$  calculation runs into several unknowns, including contact terms between two photons and two nucleons which parameterise the part of the deuteron polarisabilities not determined by long-range NN properties.

#### 5.4.2 Perturbative pions

Figure 5.7 also contains the result of a calculation at 49 MeV in the KSW variant of  $\chi EFT$ , in which pion effects are considered small enough to be included perturbatively [56, 275]. While it still allows for analytic expressions, with the Thomson limit manifestly fulfilled, it also adds some aspects of the pionic tensor force. However, its radius of convergence appears at best marginally larger than that of  $EFT(\pi)$  [276]. Since  $EFT(\pi)$  is recovered by setting the pion-nucleon coupling  $g_A$  to zero and adjusting the parameters, it is not surprising that its results are close to resummed  $EFT(\pi)$ . Indeed, Refs. [219–221] also provided the first “pion-less” Compton results. In Fig. 5.7, we rescaled the NLO calculation of Ref. [220] from the nonrelativistic flux factor to the version in Eq. (2.17) used for the other curves. This 5% change allows the dynamical content of the different theories to be isolated, based on different

kinematics used<sup>14</sup>. Finally, Chen’s investigation of unpolarised scattering off a tensor-polarised deuteron in the KSW approach [219] led Karakowski to address the same quantity in a potential model [249, 250].

## 5.5 Deuteron Compton scattering: model calculations

Several calculations of deuteron Compton scattering were performed in the 1950s and 1960s [277–281]. The earliest were based on the impulse approximation, which is poor because of the large size of the exchange currents depicted in Fig. 5.2(b). In the 1980s, Weyrauch and Arenhövel performed detailed calculations of deuteron Compton scattering that included these effects [245]. They also performed an energy-dependent multipole decomposition of the deuteron amplitude, akin to that for the nucleon amplitude in Section 2.2. From these dynamical deuteron polarisabilities, all deuteron Compton-scattering observables can be reconstructed, with predictions as a function of  $\omega$  available in Ref. [245].

Formulating the problem in terms of these quantities has the advantage that their imaginary parts can be obtained from the optical theorem and information on  $\gamma d \rightarrow NN$  from dispersion relations, parallel to the discussion in Section 4.1. This accounts for the NN-reducible piece of the Compton amplitude, see Eq. (5.6), and Fig. 5.1(b) and (c), as well as Fig. 5.2(c) and (d). The remaining effects are part of the amplitude  $T_{\gamma d}$  of all diagrams that do not include an NN intermediate state, Eq. (5.5), called the “seagull amplitude” in Ref. [245] and elsewhere. As already discussed in Section 5.2.2, significant cancellations between the NN-reducible and NN-irreducible diagrams lead to the correct Thomson limit.

Based on this, Weyrauch employed current conservation to simplify the expressions and derived an explicit representation of the NN Green’s function  $G$ , Eq. (5.6), using a separable NN interaction [246, 247]. This avoids DRs for the deuteron amplitudes. Subsequently, Wilbois [248], and later Karakowski and Miller [249, 250], used increasingly sophisticated NN potentials and added contributions beyond those mandated by current conservation, such as leading relativistic corrections and some meson-exchange currents beyond the Siegert theorem. Both arrived at similar cross sections.

The most sophisticated and most widely used calculations employing these techniques in a one-boson-exchange framework were carried out by Levchuk and L’vov [77, 251]. The NN current operator  $\mathbf{J}$  in Eq. (5.6) and the irreducible diagrams of  $T_{\gamma d}$  (5.5) are derived by minimal substitution from the one-boson-exchange Hamiltonian, including form factors. This avoids Siegert-like theorems and makes it straightforward to compute important dynamical effects, e.g. nonstatic corrections to the exchange propagators and  $\Delta(1232)$  effects, both of which Ref. [77] considered.

Turning to results, Wilbois claimed in Ref. [248] that the model dependence of the differential cross section due to the choice of NN potential is  $\approx 1\%$  or less for photon energies up to 100 MeV. Levchuk and L’vov [77] found a variation of  $\approx 5\%$  for different versions of the Bonn OBEPR potential [282], a higher cross section than those of Refs. [248–250], and more angular variation at photon energies  $\geq 70$  MeV. Several checks in Ref. [77] were used to ensure that current conservation and its consequences had been implemented at a reasonable level of accuracy. For example, the Thomson limit is violated by 6%. All implementations agreed that rescattering effects in the cross section are  $\approx 10\%$  at 50 MeV and decrease further by 100 MeV, in line with the subsequent  $\chi$ EFT findings of Fig. 5.3 in Section 5.2.4.

Of all the studies discussed in this subsection, only Refs. [77, 248–251] included terms in the single-nucleon Compton amplitude beyond the nucleon Born terms. The first four included the static values of  $\alpha_{E1}^{(s)}$  and  $\beta_{M1}^{(s)}$ , but no higher functional dependence on  $\omega$ . While good agreement with the forward-angle Lucas data [25] was found at low energies, it is not surprising that the rise of the differential cross section at backward angles in the higher-energy SAL data [26] could not be reproduced, in view of the

---

<sup>14</sup>Incidentally, the authors of Ref. [221] meant to include the minuscule contribution from the slope parameters  $\alpha_{E\nu}^{(s)}$  and  $\beta_{M\nu}^{(s)}$  in (2.13) as the leading energy-dependent effects in the scalar polarisabilities, but made the mistake of using instead the values of the leading momentum dependence of the *generalised polarisabilities* for photons of nonzero virtuality.

importance of the  $\Delta(1232)$  established in Section 5.2.3. The study of Levchuk and L'vov [77] implemented the most sophisticated single-nucleon amplitude of these models. A nonrelativistic reduction of the Dirac-Pauli Hamiltonian was performed and terms up to  $\mathcal{O}(1/M_N^2)$  were kept in the resulting Hamiltonian. They then added the contributions from the static values of  $\alpha_{E1}^{(s)}$ ,  $\beta_{M1}^{(s)}$ , the four spin polarisabilities and four fourth-order polarisabilities, including the slope parameters of Eq. (2.13). The eight higher-order polarisabilities were taken from the fixed- $t$  DR calculation of Babusci et al. [88]. As discussed in Section 2.2, this incorporates all dynamics of the Compton amplitude, up to this order in  $\omega$ . Nevertheless, they could not describe the backward-angle Hornidge (SAL) points, which led Hornidge et al. to infer a value of  $\beta_{M1}^{(n)} \approx 10$ —very different from  $\beta_{M1}^{(p)}$  [26]. However, this problem is now known to be the result of a coding mistake [283, 284]. Preliminary results from calculations that rectify this error, and improve on the treatment of the Thomson limit in Ref. [77], indicate that it is no longer necessary to employ a value of  $\beta_{M1}^{(n)}$  that differs appreciably from  $\beta_{M1}^{(p)}$  in order to reproduce these data [283, 284].

A similar model was used to calculate the inelastic reaction,  $\gamma d \rightarrow \gamma' np$  by Levchuk et al. [140, 285, 286]. The full set of diagrams for this process was not computed, since the focus in these works was on making predictions for the inelastic deuteron Compton reaction in neutron quasi-free kinematics. In this Regime, the most important diagrams correspond to photon scattering on quasi-free nucleons, NN rescattering, and the effect of meson-exchange currents and the  $\Delta(1232)$ . The OBEPR potential was again employed to compute the deuteron wave function and NN amplitude. The nucleon Compton amplitudes were taken from the DR calculation of Ref. [287]. Using these ingredients, Wissmann et al. [286] showed that the cross section above 200 MeV in the neutron quasi-free peak is large enough for an accurate extraction of  $\alpha_{E1}^{(n)}$ . These computations gave strong theoretical motivation to extract  $\alpha_{E1}^{(n)}$  from measurements of the inelastic reaction in quasi-free kinematics, as performed in Refs. [66, 68]. Different NN models predict triple-differential cross sections in this region that vary by 3% [68]. From a theoretical perspective, the absence of a full, current-conserving calculation of  $\gamma d \rightarrow \gamma' np$  is of some concern. Also, as emphasised in Section 4.1, significant model assumptions exist in the DRs of Ref. [287] that were used to analyse these data, and the unanimity in DR predictions disappears at these higher energies. The impact of different  $\gamma N \rightarrow \pi N$  multipole analyses in the DR construction of the single-nucleon amplitude was assessed in Refs. [68, 286], but this is not the only source of uncertainty in the DR calculation. Overall, the model uncertainty of  $\pm 1.1$  quoted by Kossert et al. is probably an underestimate [288]. Lastly, Levchuk et al. [140] emphasise that, in the kinematics relevant for this reaction, the  $\pi^0$  pole part, Eq. (2.6), has a marked impact on the cross section. As discussed in Section 3.5, Kossert et al. exploited this sensitivity in order to perform a simultaneous extraction of  $\alpha_{E1}^{(n)} - \beta_{M1}^{(n)}$  and  $\gamma_\pi^{(n)}$ , assuming the Baldin sum-rule value (2.7) for  $\alpha_{E1}^{(n)} + \beta_{M1}^{(n)}$  [68].

## 5.6 Compton scattering from ${}^3\text{He}$

The first computations of elastic Compton scattering on the  ${}^3\text{He}$  nucleus were performed in the past five years by Shukla (née Choudhury) et al., using the  $\chi\text{EFT}$  framework without explicit  $\Delta(1232)$  degrees of freedom at NLO ( $P^3$ ) [69–71]. Since the focus was on photon energies of 60 to 120 MeV, one can use the Regime II approximation of instantaneous interaction kernels, Eq. (5.5). A variety of potentials were employed in the calculation of the  ${}^3\text{He}$  wave function  $|\Psi_{{}^3\text{He}}\rangle$ . Effects from a three-nucleon irreducible kernel  $T_{\gamma\text{NNN}}$  begin only at  $\text{N}^3\text{LO}$ , and the  $\chi\text{EFT}$  expansion converges well. Given an expected accuracy of  $\lesssim 20\%$ , the authors present exploratory studies on the kinds of information about neutron polarisabilities that are accessible in such experiments.

Not surprisingly,  ${}^3\text{He}$  has a significantly larger cross section for coherent Compton scattering than the deuteron, due to the presence of two protons in the nucleus. Since the proton Thomson terms interfere with the neutron polarisability amplitudes in Regime II, neutron polarisabilities have a larger absolute effect on cross sections for  ${}^3\text{He}$  than for the deuteron; see Figure 5.8. Compared to the proton

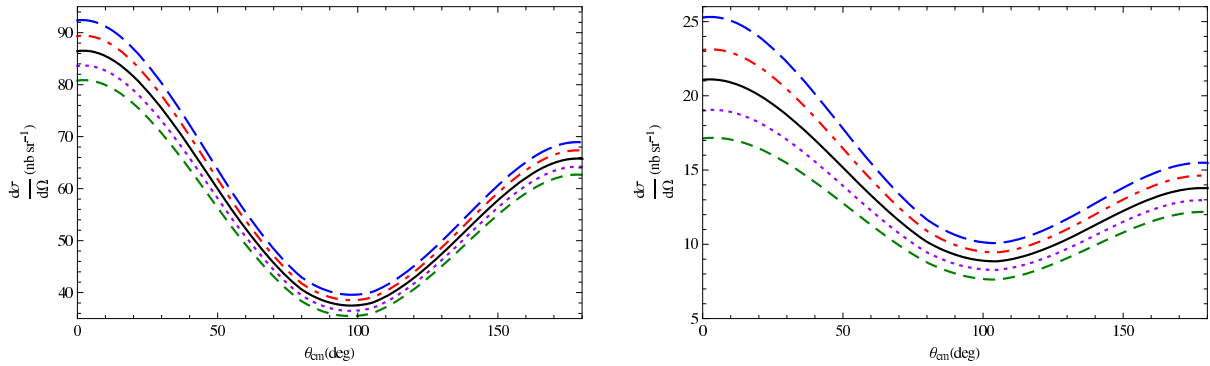


Figure 5.8: (Colour online) Sensitivity of the differential cross sections for Compton scattering on  ${}^3\text{He}$  in the centre-of-mass frame at NLO (Regime II,  $P^3$ ) in  $\chi\text{EFT}$  without explicit  $\Delta(1232)$  on  $\alpha_{E1}^{(n)}$  at 60 (left) and 120 MeV (right). Solid (black) curve: central value  $\alpha_{E1}^{(n)} = 12.2$ ; long-dashed (blue):  $\alpha_{E1}^{(n)} - 4$ , dot-dashed (red):  $-2$ , dotted (magenta):  $+2$ , dashed (green):  $+4$ . From Ref. [70].

and deuteron results of Figs. 4.9 and 5.4, the process scales roughly with  $Z^2$  and is indeed coherent at the lower end,  $\omega_{\text{cm}} \approx 60$  MeV, while cross sections are enhanced over the single-charge results only by  $Z$  for 120 MeV.

The sensitivity of the cross section to the scalar polarisabilities of the neutron was tested by including the higher-order terms  $\delta\alpha_{E1}^{(n)}$ ,  $\delta\beta_{M1}^{(n)}$  for variations about the  $\mathcal{O}(P^3)$  predictions (4.13). The example in Fig. 5.8 shows a significant effect from the neutron electric polarisability. Varying the magnetic polarisability produces effects of a similar magnitude. Experimental prospects and possible improvements will be discussed in Section 6, together with results for double-polarisation observables.

## 6 The future

We conclude by outlining the experimental and theoretical progress which can be expected in this area over the next few years.

### 6.1 The case for investigating spin polarisabilities

An exciting new frontier in low-energy Compton scattering from light nuclei is the use of polarised beams and targets to isolate specific polarisabilities of interest. In particular, the future holds considerable promise for gaining access to the dipole spin polarisabilities which have thus far been rather poorly constrained (see Section 2.2). The values extracted from experiments on the proton can be compared to those of the neutron measured in, e.g.,  ${}^3\text{He}$ , and to different combinations of isoscalar spin polarisabilities accessible on the deuteron.  $\chi\text{EFT}$  predictions at order  $\epsilon^3 \sim e^2\delta^3(\text{modified})$  exist for the sensitivity of the following observables to both scalar and spin polarisabilities: circularly or linearly polarised beams on polarised protons (and, perhaps less useful, neutrons) [90, 92] and circularly or linearly polarised beams on unpolarised or vector polarised deuterons [93]. A study of many deuteron observables was first conducted in the “ $\Delta$ -less” version at NLO ( $P^3$ ) with strict Regime II counting in Refs. [71, 101].

For both the deuteron and the proton, the sensitivity to  $\gamma_{E1E1}$  seems particularly large for  $\Delta_x^{\text{circ}}$  (2.24), the difference of scattering a right-circularly polarised photon on a target polarised in either direction perpendicular to the scattering plane. A good signal for  $\gamma_{M1M1}$  is also seen in the observable  $\Delta_z^{\text{lin}}$ , for which the target is polarised parallel to the beam and the photons are linearly polarised either in the scattering plane or perpendicular to it. For all targets, the spin polarisabilities can be reliably extracted at photon energies  $\gtrsim 100$  MeV, after measurements at  $\lesssim 70$  MeV provide high-accuracy



determinations of the scalar polarisabilities so that they do not contaminate the residual uncertainties of the spin polarisabilities [93]. Since full information on sensitivities and impact of constraints like the Baldin sum rule cannot adequately be conveyed on paper, Ref. [93] focused only on prominent examples and made the complete results available as an interactive *Mathematica* notebook<sup>15</sup>.

As an example of a double-polarised observable in  ${}^3\text{He}$ , Fig. 6.1 shows predictions at 120 MeV for  $\Delta_z^{\text{circ}}$ . In addition to the first  ${}^3\text{He}$  Compton-scattering calculation discussed in Section 5.6, Shukla et al. [69–71] demonstrated that polarised  ${}^3\text{He}$  behaves as an “effective polarised neutron” in Compton scattering. For this case, at least up to NLO, the Compton response is dominated by the nuclear configuration in which the two protons are paired in a relative S-wave, and the spin of the nucleus is carried by the neutron. The two-body currents at NLO were found to be almost completely independent of the  ${}^3\text{He}$  target spin. These two facts lead to  ${}^3\text{He}$  double-polarisation observables that look very similar to the neutron asymmetries in Refs. [90, 92, 98]. In each panel, one of the four neutron spin polarisabilities in the basis of (2.12) is varied. This shows that a measurement of  $\Delta_z^{\text{circ}}$  at this energy should enable an extraction of the combination  $\gamma_1^{(n)} - (\gamma_2^{(n)} + 2\gamma_4^{(n)}) \cos \theta_{\text{cm}} = -(\gamma_{E1E1}^{(n)} + \gamma_{E1M2}^{(n)}) - (\gamma_{M1E2}^{(n)} + \gamma_{M1M1}^{(n)}) \cos \theta_{\text{cm}}$ .  $\Delta_x^{\text{circ}}$  (2.24) was found to be sensitive to a different combination of neutron spin polarisabilities.

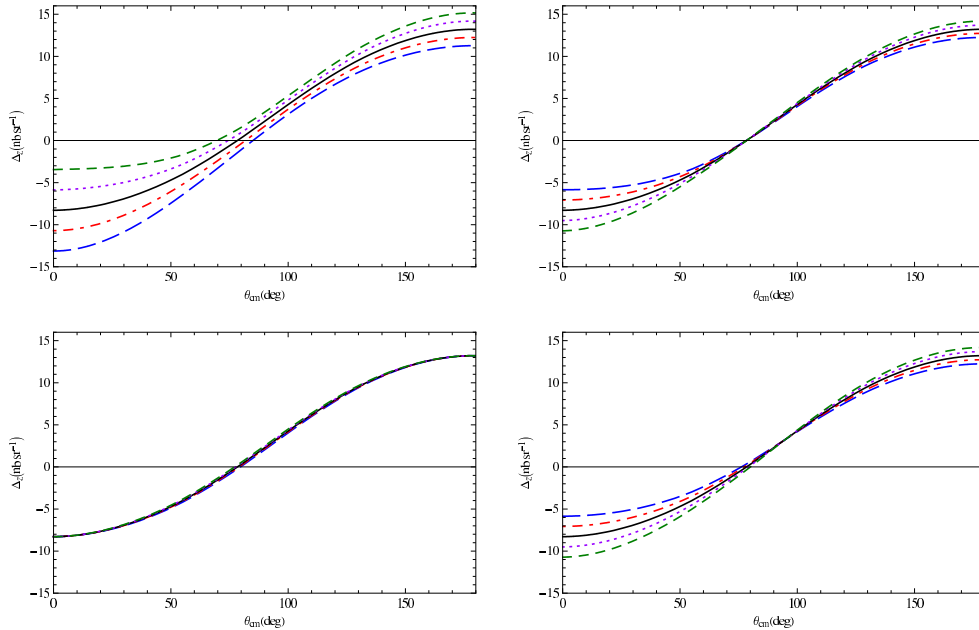


Figure 6.1: (Colour online) Sensitivity of the double-polarisation observable  $\Delta_z^{\text{circ}}$  in  ${}^3\text{He}$  Compton scattering in the centre-of-mass frame at NLO (Regime II) in  $\chi\text{EFT}$  without explicit  $\Delta(1232)$  at 120 MeV when varying the neutron spin polarisabilities  $\gamma_1^{(n)}$  (top left),  $\gamma_2^{(n)}$  (top right),  $\gamma_3^{(n)}$  (bottom left) and  $\gamma_4^{(n)}$  (bottom right), around the  $\mathcal{O}(P^3)$  values (4.13). Solid (black) curve: unperturbed NLO result; variations  $\delta\gamma_i^{(n)}$  of  $-100\%$  (long-dashed blue),  $-50\%$  (dot-dashed red),  $+50\%$  (dotted magenta) and  $+100\%$  (short-dashed green) of the central value. From Ref. [70].

<sup>15</sup>Ref. [93] contains two coding errors. All “isoscalar” variations quoted should be interpreted as variations around the isoscalar values for the neutron polarisabilities *only*. Fortunately, this leaves the conclusions qualitatively unchanged, albeit with all sensitivities doubled. Finally, the variation of  $\gamma_{E1E1}$  around its (correct) central value was implemented with wrong signs.

## 6.2 Experiment

The High Intensity Gamma-Ray Source (HI $\gamma$ S) will soon perform its first Compton scattering experiment that is dedicated to the extraction of nucleon polarisabilities. At HI $\gamma$ S, the photons produced in a free-electron laser (FEL) are backscattered by the electrons in the FEL storage ring to produce a high-intensity beam of nearly monochromatic, 100% polarised photons, with either linear or circular photon polarisation [99]. The photon energy resolution depends on the collimation of the incident beam, but resolution of 2-3% with photon fluxes of  $\sim 10^7$  Hz is readily possible. Photon energies up to 80 MeV are already available at HI $\gamma$ S, and the region around pion threshold is anticipated to be accessible in 2 to 3 years. Because the HI $\gamma$ S photon beam does not involve bremsstrahlung, it is extremely clean, with very low background.

Early Compton scattering at HI $\gamma$ S will focus on exploiting the high intensity of the beam to perform precision measurements on the proton and deuteron. Unpolarised measurements on deuterium will be done at 65 and 100 MeV using a scintillating active target [289]. For the first time, Compton scattering will be measured by detecting the recoil deuteron in coincidence with the scattered photon, an advance which is expected to greatly reduce backgrounds from inelastic scattering and other beam-induced processes. This new data set will overlap with the existing data of Refs. [25–27], but will have significantly better statistics than these previous experiments.

Single- and double-polarised measurements are anticipated to be a high priority at HI $\gamma$ S [99]. For example, another active target will be used for the photon-beam asymmetry  $\Sigma_3$  (2.23) at  $90^\circ$  and 82 MeV [290]. This experiment will isolate  $\alpha_{E1}^{(p)}$  at an angle of  $90^\circ$  using linearly polarised photons, since  $\beta_{M1}^{(p)}$  does not contribute to  $\Sigma_3$  at that angle, as discussed in Section 2.4. The lowest energy with published beam-asymmetry data is presently  $\omega_{\text{cm}} = 213.1$  MeV [123–125], so this experiment represents a substantial increase of the kinematic range.

Entirely new investigations of double-polarisation observables on the proton are planned at both HI $\gamma$ S and Mainz. At HI $\gamma$ S, a circularly polarised beam of energy 100 MeV incident on a newly designed, scintillating, transversely polarised proton target will enable a measurement of the double-spin asymmetry,  $\Sigma_x^{\text{circ}}$  (2.25), and provide access to  $\gamma_{E1E1}^{(p)}$  [291]. Meanwhile, experiments with a polarised beam and a polarised  $^3\text{He}$  target will be carried out at a photon energy of 125 MeV [292] to explore the neutron spin polarisabilities. HI $\gamma$ S would also be the ideal place to measure the double-polarisation observables on the deuteron discussed above. Such a programme requires a polarised deuterium target, although as yet there are no specific plans at HI $\gamma$ S for such experiments. However, we reiterate that they could provide complementary information on neutron spin polarisabilities to the  $^3\text{He}$  experiments already scheduled.

A measurement of unpolarised Compton scattering on  $^6\text{Li}$  at 60 MeV has already been completed at HI $\gamma$ S [293], and data taking at 80 MeV is planned. With suitable theoretical interpretation, such cross sections could provide an alternative path to the extraction of  $\alpha_{E1}^{(n)}$  and  $\beta_{M1}^{(n)}$ . The path towards such an extraction is further advanced for  $Z = 2$  nuclei, as seen for  $^3\text{He}$  in Section 5.6. Another good candidate for complementary information is  $^4\text{He}$ , since it is both a scalar and isoscalar target, with cross sections that are comparable in magnitude to those on  $^3\text{He}$ . In these Helium nuclei, nuclear binding is not as complex as in  $^6\text{Li}$ , and so measurements of their Compton cross sections would be very worthwhile. The prospects for advances in the theory of all these nuclear Compton reactions are discussed in Section 6.3.

Another avenue to measure nucleon polarisabilities has been pursued at the S-DALINAC at Darmstadt. A proof-of-principle experiment was performed at low energies using a bremsstrahlung beam and a high-pressure ionisation chamber [294]. This chamber, which could be filled with hydrogen or deuterium, functioned as both the target and as a particle detector for the recoiling hadron. Even with a continuous bremsstrahlung distribution for the incident photon beam, the coincident detection of the scattered photon in a  $25.4 \text{ cm} \times 35.6 \text{ cm}$  NaI detector and the struck-particle recoil in the active target volume provided sufficient kinematic over-determination to reduce backgrounds significantly. A test

measurement of  $\gamma p$  differential cross sections using bremsstrahlung endpoints of 60 and 79 MeV obtained data of comparable statistical quality to that of Federspiel [20] for  $30 \text{ MeV} \leq \omega_{\text{lab}} \leq 50 \text{ MeV}$ . Yevetska et al. claim that “expected yields from an experiment based on the technique described here are at least an order of magnitude larger than in the experiment of [Ref. [24]]” and conclude that high-statistics experiments using this setup are feasible. However, no full-scale production run is planned.

MAX-Lab at Lund is presently performing unpolarised measurements on the deuteron at 145 to 170 MeV. These will provide the first high-accuracy Compton scattering data on deuterium at higher energies [295]. Data from previous runs below 115 MeV are being analysed in parallel [138, 139]. For both, the experimental setup at Lund is the same as that described at the end of Section 3.4. While proton data exist up to the  $\Delta(1232)$  resonance (as discussed in Sections 3 and 4.4), there are no analogous measurements on the deuteron, so data on the neutron amplitude in this energy range are quite limited. One of the primary motivations for extending the Compton experiments at Lund above pion-production threshold is to provide benchmark data for EFT calculations that are envisioned for the near future (see below).

A new synchrotron light facility, MAX-IV, is presently being constructed at Lund [296]. Under a proposal to dedicate one of the beamlines to nuclear physics, its 1.5 GeV electron storage ring could open up new opportunities. Perhaps as soon as 2014, it will be possible to perform laser backscattering via a technique similar to that at LEGS and produce collimated photon beams of  $> 10^4 \text{ Hz}$  and polarisations of  $> 70\%$  for  $130 \text{ MeV} \leq \omega_{\text{lab}} \leq 157 \text{ MeV}$ . These could be used for Compton scattering and other photonuclear experiments [297]. Even at this early stage, a directed programme of Compton studies is being explored.

MAMI at Mainz has also been gearing up to perform polarised Compton experiments using the Crystal Ball detector [298]. These experiments cover the energy range 200–300 MeV and focus on the spin polarisabilities of the proton. Polarised photon beams are incident on either an unpolarised liquid hydrogen target or a polarised frozen-spin butanol target, with the target located at the centre of the Crystal Ball. Higher photon energies are mandatory for this detection scheme because, as seen in Section 3.2, Compton scattering cannot be separated from other processes unless the recoil proton is detected in coincidence with the scattered photon. MAMI produces linearly polarised beams using tagged coherent bremsstrahlung on a diamond radiator, and circularly polarised beams via a longitudinally polarised electron beam incident on an amorphous radiator. Three separate polarisation observables are measured:  $\Sigma_3$ , as well as  $\Sigma_x^{\text{circ}}$  and  $\Sigma_z^{\text{circ}}$ . These experiments have only recently begun, and so far only preliminary results have been obtained. Since MAMI already has a polarised  $^3\text{He}$  target, the possibility to perform similar experiments for  $\gamma^3\text{He}$  scattering also exists [299]. Such experiments, in concert with those at HI $\gamma$ S, will provide access to the proton and neutron spin polarisabilities.

We close our discussion of the future of experiments by reiterating a central conclusion from the proton analysis of Section 4.4. The unpolarised proton database is somewhat noisy, and the data that exist between 190 MeV and 250 MeV are contradictory and not of particularly high quality. The statement in Section 5.3 about improving the deuteron database also applies to the proton: data of higher quality with carefully formulated correlated and point-to-point systematic errors are needed. Theorists and experimentalists should work together in order to determine which of the sometimes-conflicting data sets are trustworthy and to ensure that part of the future experimental Compton programme enhances the set of measurements of unpolarised  $\gamma p$  scattering.

### 6.3 Theory

Indeed, it is notable that the last twenty years of the history of low-energy Compton scattering from protons and light nuclei has been marked by significant cooperation between experiment and theory (EFTs, DRs, . . .). We will now provide an outlook for the theoretical advances which can be anticipated, bearing in mind that the future path of theoretical developments is somewhat trickier to predict than

that of experimental work.

In Section 4.4, we presented results of an analysis of proton data up to energies around 350 MeV using  $\chi$ EFT with a resonant  $\Delta(1232)$  pole as well as  $\pi$ N loops at  $\mathcal{O}(e^2\delta^3)$ , with a first look at extending to  $\mathcal{O}(e^2\delta^4)$  (N<sup>2</sup>LO) by including higher-order  $\pi$ N loops. It was noted that in order to obtain a reasonable fit to the data at  $\mathcal{O}(e^2\delta^4)$ , a contact term had to be added to the calculation, thereby allowing the value of  $\gamma_{M1M1}$  to be tuned. This analysis is presently being refined. In particular, the impact of other spin polarisabilities on the fit must be examined, and the effect of  $\gamma$ N $\Delta$  vertex dressing must be incorporated. The resulting calculation will be complete up to  $\mathcal{O}(e^2\delta^4)$  in the low-energy region and up to  $\mathcal{O}(e^2\delta^0)$  in the vicinity of the resonance, and it is expected to produce robust constraints on the scalar polarisabilities  $\alpha_{E1}^{(p)}$  and  $\beta_{M1}^{(p)}$  [214].

In order to interpret the ongoing experiment at MAX-Lab described above, a theory capable of describing elastic scattering on the deuteron up to  $\omega_{\text{lab}} \approx 200$  MeV is required, taking into account that pion photoproduction channels are open. In particular, as the energy increases towards the  $\Delta(1232)$  peak, it is expected that resonant pion photoproduction will play an increasingly important role. The  $\delta$  expansion [205] mandates that the NN and N $\Delta$  channels should be treated on an equal footing in the vicinity of the resonance peak. But experience from the single-nucleon sector, combined with the power-counting arguments of Section 4.2, implies that this is only strictly necessary within about 50 MeV of the peak. Thus, the first step for analysing data up to 200 MeV will be a perturbative inclusion of  $\Delta$  effects, with pion production. However, it must be noted that a reliable calculation has to include the correct  $d\gamma \rightarrow d\pi^0$  and  $\gamma d \rightarrow NN\pi$  thresholds—just as the  $\pi$ N threshold had to be corrected in the proton calculation. The remedy in the NN sector is well-defined, see Refs. [300–305], but more elaborate than for the single-nucleon sector. At higher energies, the issues of chirally consistent currents [306–309], wave functions and potentials [226, 228, 229, 232–234, 310] must also be revisited. As discussed in Section 5.2.4, they are largely absent at lower energies, thanks to the strict constraint imposed by the Thomson limit.

Computing the deuteron breakup reaction  $\gamma d \rightarrow \gamma np$  in  $\chi$ EFT is a high priority for future work. The calculation of Levchuk and L’vov was used to extract  $\alpha_{E1}^{(n)}$  from data on this reaction in Ref. [68], as discussed in Section 5.5. It is important to analyse its model dependence using a theory with a consistent description of Compton interactions in the one- and two-nucleon sectors, along with defensible error bars. The quasi-free mechanisms are independent of the  $\chi$ EFT cutoff for low missing momenta, but corrections from final-state interactions could be sensitive to details of the short-distance physics in the NN system [310].  $\chi$ EFT therefore provides a diagnostic—the cutoff dependence of results—which facilitates studying the reliability of the calculation of effects in the NN sector.

The single-nucleon amplitude described in Section 4.4 and presented in Ref. [214] will also provide an alternative to the dispersion-relation methods used by Kossert et al. [68] for the analysis of the quasi-free data. In particular, one might be concerned that the asymptotic contributions to the dispersion-relation integrals introduces uncontrolled model dependence. The  $\chi$ EFT amplitude will be able to demonstrate the extent to which different assumptions about the short-distance  $\gamma$ N physics alter the extracted value of  $\alpha_{E1}^{(n)}$ . If  $\chi$ EFT confirms that the kinematics of Ref. [68] are ideal for a reliable extraction of  $\alpha_{E1}^{(n)}$  from inelastic deuteron Compton data, then a by-product of such an analysis could be a  $\chi$ EFT result for  $\gamma_{\pi}^{(n)}$ , to which these data are also sensitive (see Section 3.5). More broadly, such a calculation could be envisioned as a tool to search for other kinematics in order to optimise the extraction of neutron polarisabilities.

Turning from the 2N to the 3N sector, we have already argued that  ${}^3\text{He}$  provides a fine opportunity for obtaining information on the neutron Compton amplitude (see Sections 5.6 and 6.1). The experiments at HI $\gamma$ S and MAMI discussed in Section 6.2 aim to use this opportunity to provide data pertinent to the spin polarisabilities of the nucleon, but the calculations reported in Section 5.6 for  ${}^3\text{He}$  were clearly exploratory in nature. They neither contained a dynamical  $\Delta(1232)$  nor assessed the importance of rescattering in the 3N intermediate state. In combination, these effects can increase double-polarisation

observables by up to a factor of 2 [93].

In particular, the results from Compton scattering on deuterium presented in Section 5.2.4 suggest that rescattering significantly reduces the wave-function dependence seen in Refs. [69–71]. For the deuteron, rescattering increases some double-polarisation observables by up to 40% at 125 MeV [93]. It is therefore imperative to include the effect of rescattering for  ${}^3\text{He}$  in order to provide a precise  $\chi\text{EFT}$  extraction of neutron polarisabilities from forthcoming data. A Bochum-Jülich-Bonn-Washington (DC) collaboration is embarking on such a calculation, initially using the “ $\Delta$ -less”  $\chi\text{EFT}$  NN and NNN potential at  $\text{N}^2\text{LO}$ . As in the case of the deuteron, consistency between the  ${}^3\text{He}$  wave function, the nuclear interaction and the nuclear electromagnetic operators is a key ingredient. The correct  $\chi\text{EFT}$  implementation in the low-energy (Regime I) power counting can again be checked by the Thomson and Gell-Mann-Goldberger-Low low-energy theorems for the triton and  ${}^3\text{He}$ .

As for the proton and deuteron, we also expect the  $\Delta(1232)$  to have a large effect on observables at  $\omega_{\text{lab}} \gtrsim 90$  MeV. It is straightforward to include the single-nucleon amplitudes with an explicit  $\Delta$  at orders  $\epsilon^3$  and  $e^2\delta^4$ , respectively, into the  ${}^3\text{He}$  calculations. In contradistinction to the deuteron case,  $\Delta$  exchange currents can appear, and so a consistent  $\chi\text{EFT}$  calculation requires the  $\pi$ -exchange diagrams of Refs. [69–71] to be complemented by currents with  $\Delta$ s. In the kinematic domain  $0 \leq \omega \sim m_\pi$ , the  $\pi\text{N}\Delta$  interactions and corrections to the  $3\text{N} \rightarrow 3\text{N}$  Green’s function do not have to be resummed but can be treated in perturbation theory. In the longer term, a calculation that includes channels with up to one explicit  $\Delta(1232)$  and a resummation of intermediate-state interactions can be anticipated. It would compute the coherent reaction in a consistent manner over the entire kinematic range  $0 \leq \omega \leq 350$  MeV, similar to the ongoing effort for the deuteron. Inelastic Compton scattering on  ${}^3\text{He}$  could also be used to extract proton or neutron polarisabilities in specific kinematics, as for the deuteron.

Compton scattering from nuclei such as  ${}^4\text{He}$  and  ${}^6\text{Li}$  is becoming accessible to ab initio calculation. Bampa et al. recently applied the Lorentz Integral Transform (LIT) method to deuteron Compton scattering with a  $\chi\text{EFT}$  potential [311]. The currents were constructed via Siegert-like theorems. The results up to 60 MeV are promising. The same method is presently being applied to  ${}^6\text{Li}$  [312], for comparison with the recently completed  ${}^6\text{Li}$  experiment at 60 MeV at HI $\gamma$ S [293]. This computation will then be extended to higher energies by incorporating NN currents beyond the electric dipole and the full single-nucleon amplitude. The ability to accurately assess the impact of nucleon polarisabilities in Compton scattering from  ${}^6\text{Li}$  offers the tantalising prospect that they could be extracted there, where the cross section in the coherent region is about twice as large as in  ${}^3\text{He}$ —and roughly nine times larger than for the proton or deuteron.

## 6.4 Conclusion

An energy-dependent multipole analysis of Compton scattering provides important information on the scales, symmetries and mechanisms which govern the interactions amongst the low-energy constituents of the nucleon, and with photons. It facilitates exploration of the chiral symmetry and isospin dependence of the pion cloud, the properties of the  $\Delta(1232)$  resonance, and the question of which degrees of freedom dominate the response of the nucleon spin to electromagnetic fields. It is in this context that Chiral Effective Field Theory has emerged as a systematic and reliable tool to guide, predict and analyse experiments.

A window of opportunity seems to be emerging between the competing demands of theorists and experimentalists. With increasing nuclear mass, there is also an increase in the number and viability of potential target nuclei. Cross sections grow quadratically with the target charge  $Z$  at lower energies where the nucleons act coherently, and still linearly with  $Z$  at higher energies,  $\omega \gtrsim 100$  MeV. This makes high-accuracy experiments more feasible for heavier nuclear targets. Breakup experiments on such nuclei may permit the isolation of neutron properties in particular, but proton structure effects may also be enhanced thanks to the interference effects with more charges in the target. On the other



hand, interpreting such data in terms of the properties of the individual nucleons requires a model-independent analysis which treats nuclei by ab initio methods. This poses no difficulty for deuteron Compton scattering and is within reach for  ${}^3\text{He}$ . Given the recent progress, one can speculate that both  ${}^4\text{He}$  and  ${}^6\text{Li}$  may be treated in the same  $\chi\text{EFT}$  framework. This will also provide important benchmarks on the accuracy with which  $\chi\text{EFT}$  describes nuclear binding and the charged meson-exchange currents which are directly probed by the Compton photons.

In conclusion, the future is bright for Compton scattering from protons and light nuclei, both literally and figuratively. A number of high-luminosity facilities around the world conduct or plan to perform experiments that will map out the spin polarisabilities of the proton, with those of the neutron not far behind. More sophisticated experiments, with higher fluxes and improved target techniques, combined with ab initio computations based on  $\chi\text{EFT}$  Hamiltonians, current operators and photon-nucleon amplitudes, could permit the use of nuclei up to at least  $A = 6$ . The resulting values for the twelve static dipole polarisabilities of the proton and neutron will provide important benchmarks for lattice QCD computations and models of the nucleon. The picture that ultimately emerges of the manner in which mechanisms driven by chiral symmetry (like pion loops) compete with other shorter-distance effects (like the properties of the  $\Delta(1232)$  resonance) will provide fascinating and important insights into the similarities and differences of the two-photon responses of the proton and the neutron.

## Acknowledgements

We acknowledge our many collaborators, who have shared their insights on these topics with us. We are especially grateful to: Vadim Lensky and Vladimir Pascalutsa for correspondence regarding Ref. [184] and for supplying us with curves relevant to that calculation; Winfried Leidemann for information on future plans regarding application of the Lorentz Integral Transform to Compton scattering; Anatoly L’vov for discussion of the theoretical uncertainties associated with his calculations; Barbara Pasquini for comments on dispersion relations; Paul Hewson for a stunningly quick coding of some amplitudes; Deepshikha Shukla for helping to clarify numerical issues in deuteron Compton scattering; and the organisers and participants of the INT workshop 08-39W: “Soft Photons and Light Nuclei” (all) and of the INT programme 10-01: “Simulations and Symmetries” (JMcG, HWG and DRP), both of which also provided financial support. This work has been supported in part by UK Science and Technology Facilities Council grants ST/F012047/1, ST/J000159/1 (JMcG) and ST/F006861/1 (DRP), by the US Department of Energy under grants DE-FG02-06ER-41422 (GF), DE-FG02-95ER-40907 (HWG) and DE-FG02-93ER-40756 (DRP), by the US National Science Foundation CAREER award PHY-0645498 (HWG), and by University Facilitating Funds of the George Washington University (HWG).

# References

- [1] J. W. Strutt (3rd Lord Rayleigh), *Philos. Mag.* **XLI** (1871) 107, 274.
- [2] J. W. Strutt (3rd Lord Rayleigh), *Philos. Mag.* **XLVII** (1899) 375.
- [3] A. H. Compton, *Phys. Rev.* **21** (1923) 483.
- [4] H. Bethe and R. Peierls, *Proc. R. Soc. Lond.* **A148** (1935) 146.
- [5] W. Thirring, *Philos. Mag. (Series 7)* **41** (1950), 1193.
- [6] R. G. Sachs and N. Austern, *Phys. Rev.* **81** (1951) 705.
- [7] F. E. Low, *Phys. Rev.* **96** (1954) 1428.
- [8] M. Gell-Mann, M. L. Goldberger, *Phys. Rev.* **96** (1954) 1433-1438.
- [9] J.L. Friar, *Annals of Phys. (NY)* **95** (1975) 170.
- [10] M. Schumacher, *Prog. Part. Nucl. Phys.* **55** (2005) 567 [arXiv:hep-ph/0501167].
- [11] A. I. Lvov, *Int. J. Mod. Phys. A* **8** (1993) 5267.
- [12] M. Bawin and S. A. Coon, *Phys. Rev. C* **55** (1997) 419 [arXiv:nucl-th/9610028].
- [13] H. W. Griebhammer and T. R. Hemmert, *Phys. Rev. C* **65** (2002) 045207 [arXiv:nucl-th/0110006].
- [14] R. P. Hildebrandt, H. W. Griebhammer, T. R. Hemmert and B. Pasquini, *Eur. Phys. J. A* **20** (2004) 293 [arXiv:nucl-th/0307070].
- [15] D. Drechsel, B. Pasquini and M. Vanderhaeghen, *Phys. Rept.* **378** (2003) 99 [arXiv:hep-ph/0212124].
- [16] K. Pachucki, *Phys. Rev. A* **60** (1999) 3593.
- [17] C. E. Carlson and M. Vanderhaeghen, arXiv:1109.3779 [physics.atom-ph].
- [18] A. Walker-Loud, C. E. Carlson and G. A. Miller, arXiv:1203.0254 [nucl-th].
- [19] M. T. Hutt, A. I. L'vov, A. I. Milstein, M. Schumacher, *Phys. Rept.* **323** (2000) 457 [arXiv:nucl-th/9905026].
- [20] F. J. Federspiel et al., *Phys. Rev. Lett.* **67** (1991) 1511.
- [21] E. L. Hallin et al., *Phys. Rev.* **C48** (1993) 1497.
- [22] B. E. MacGibbon et al., *Phys. Rev.* **C52** (1995) 2097.
- [23] A. Zieger et al., *Phys. Lett. B* **278** (1992) 34.
- [24] V. Olmos de León et al., *Eur. Phys. J.* **A10** (2001) 207.
- [25] M. A. Lucas, Ph.D. thesis, University of Illinois (1994).
- [26] D. L. Hornidge, B. J. Warkentin, R. Igarashi, J. C. Bergstrom, E. L. Hallin, N. R. Kolb, R. E. Pywell, D. M. Skopik et al., *Phys. Rev. Lett.* **84** (2000) 2334. [nucl-ex/9909015].
- [27] M. Lundin et al., *Phys. Rev. Lett.* **90** (2003) 192501 [nucl-ex/0204014].
- [28] G. Dattoli, G. Matone, D. Prosperi, *Lett. Nuovo Cim.* **19** (1977) 601.
- [29] A. Schafer, R. Muller, D. Vasak, W. Greiner, *Phys. Lett.* **B143** (1984) 323.
- [30] R. Weiner, W. Weise, *Phys. Lett.* **B159** (1985) 85.
- [31] M. De Sanctis, D. Prosperi, *Nuovo Cim.* **A103** (1990) 1301.
- [32] S. Capstick, B. D. Keister, *Phys. Rev.* **D46** (1992) 84.
- [33] H. Liebl, G. R. Goldstein, *Phys. Lett.* **B343** (1995) 363 [arXiv:hep-ph/9411230].
- [34] E. M. Nyman, *Phys. Lett.* **B142** (1984) 388.
- [35] M. Chemtob, *Nucl. Phys.* **A473** (1987) 613.
- [36] N. N. Scoccola, W. Weise, *Phys. Lett.* **B232** (1989) 287.
- [37] N. N. Scoccola, W. Weise, *Nucl. Phys.* **A517** (1990) 495.
- [38] S. Saito, M. Uehara, *Phys. Lett.* **B325** (1994) 20.
- [39] Y. -b. Dong, A. Faessler, T. Gutsche, J. Kuckei, V. E. Lyubovitskij, K. Pumsa-ard, P. -N. Shen, *J. Phys. G* **G32** (2006) 203 [arXiv:hep-ph/0507277].
- [40] Y. B. Dong, D. Y. Chen, *Nucl. Phys.* **A766** (2006) 183.
- [41] W. Detmold, B. C. Tiburzi, A. Walker-Loud, *Phys. Rev.* **D73** (2006) 114505 [arXiv:hep-lat/0603026].
- [42] J. C. Christensen, W. Wilcox, F. X. Lee, L. -m. Zhou, *Phys. Rev.* **D72** (2005) 034503.
- [43] F. X. Lee, L. Zhou, W. Wilcox, J. C. Christensen, *Phys. Rev.* **D73** (2006) 034503.
- [44] M. Lujan, A. Alexandru and F. Lee, arXiv:1111.6288 [hep-lat].
- [45] W. Detmold, B. C. Tiburzi, A. Walker-Loud, *Phys. Rev.* **D79** (2009) 094505 [arXiv:0904.1586].
- [46] W. Detmold, B. C. Tiburzi, A. Walker-Loud, *Phys. Rev.* **D81** (2010) 054502 [arXiv:1001.1131].
- [47] M. Engelhardt, *PoS LAT2009* (2009) 128 [arXiv:1001.5044 [hep-lat]].

- [48] M. Engelhardt, PoS **LATTICE2011** (2011) 153 [arXiv:1111.3686 [hep-lat]].
- [49] A. Alexandru and F. Lee, PoS **LATTICE2010** (2010) 131 [arXiv:1011.6309 [hep-lat]].
- [50] F. X. Lee and A. Alexandru, arXiv:1111.4425 [hep-lat].
- [51] J. M. Blatt and J. D. Jackson, Phys. Rev. **76** (1949) 18.
- [52] H. A. Bethe, Phys. Rev. **76** (1949) 38.
- [53] J. Schwinger, hectographed notes on nuclear physics, Harvard University 1947.
- [54] G. F. Chew and M. L. Goldberger, Phys. Rev. **75** (1949) 1637.
- [55] F. C. Barker and R. E. Peierls, Phys. Rev. **75** (1949) 3122.
- [56] D. B. Kaplan, M. J. Savage and M. B. Wise, Nucl. Phys. B **534** (1998) 329 [arXiv:nucl-th/9802075].
- [57] J. Gegelia, Phys. Lett. B **429** (1998) 227.
- [58] M. C. Birse, J. A. McGovern and K. G. Richardson, Phys. Lett. B **464** (1999) 169 [arXiv:hep-ph/9807302].
- [59] U. van Kolck, Nucl. Phys. A **645** (1999) 273 [arXiv:nucl-th/9808007].
- [60] S. R. Beane, W. Detmold, P. M. Junnarkar, T. C. Luu, K. Orginos, A. Parreno, M. J. Savage and A. Torok et al., arXiv:1108.1380 [hep-lat].
- [61] G. Colangelo et al., Eur. Phys. J. C **71** (2011) 1695 [arXiv:1011.4408 [hep-lat]].
- [62] E. E. Scholz, S. Borsanyi, S. Durr, Z. Fodor, S. D. Katz, S. Krieg, A. Schafer and K. K. Szabo, arXiv:1111.3729 [hep-lat].
- [63] S. Weinberg, Phys. Lett. **B295** (1992) 114. [hep-ph/9209257].
- [64] K. W. Rose et al., Phys. Lett. B **234** (1990) 460.
- [65] K. W. Rose et al., Nucl. Phys. A **514** (1990) 621.
- [66] N. R. Kolb et al., Phys. Rev. Lett. **85** (2000) 1388.
- [67] K. Kossert et al., Phys. Rev. Lett. **88** (2002) 162301.
- [68] K. Kossert, M. Camen, F. Wissmann, J. Ahrens, J. R. M. Annand, H. J. Arends, R. Beck, G. Caselotti et al., Eur. Phys. J. **A16** (2003) 259.
- [69] D. Choudhury, A. Nogga and D. R. Phillips, Phys. Rev. Lett. **98** (2007) 232303 [arXiv:nucl-th/0701078].
- [70] D. Shukla, A. Nogga and D. R. Phillips, Nucl. Phys. A **819** (2009) 98 [arXiv:0812.0138 [nucl-th]].
- [71] D. Choudhury, Ph.D. Thesis Ohio University (2006).
- [72] R. E. Prange, Phys. Rev. **110** (1958) 240.
- [73] M. Jacob and J. Mathews, Phys. Rev. **117** (1960) 854.
- [74] S. Ragusa, Phys. Rev. D **47** (1993) 3757.
- [75] A. M. Baldin, Nucl. Phys. **18** (1960) 310.
- [76] L. I. Lapidus, Sov. Phys. JETP **16** (1963) 964.
- [77] M. I. Levchuk and A. I. L'vov, Nucl. Phys. A **674** (2000) 449 [arXiv:nucl-th/9909066].
- [78] D. Babusci, G. Giordano, G. Matone, Phys. Rev. **C57** (1998) 291 [arXiv:nucl-th/9710017].
- [79] M. C. M. Rentmeester, R. G. E. Timmermans, J. L. Friar and J. J. de Swart, Phys. Rev. **C67** (1999) 044001
- [80] O. Klein and T. Nishina, Z. Phys. **A 52** (1929) 853
- [81] J. L. Powell, Phys. Rev. **75**, (1949) 32.
- [82] V. A. Petrun'kin, Sov. Phys. JETP **13** (1961) 808.
- [83] V. A. Petrun'kin, Sov. J. Particles Nucl. **12** (1981) 278.
- [84] V. I. Ritus, ZhETP **32** (1957) 1536 [Sov. Phys. JETP **5** (1957) 1249].
- [85] A. P. Contogouris, Nuovo Cim. **25** (1962) 104.
- [86] Y. Nagashima, Progr. Theor. Phys. **33** (1965) 828.
- [87] W. Pfeil, H. Rollnik and S. Stankowski, Nucl. Phys. B **73** (1974) 166.
- [88] D. Babusci, G. Giordano, A. I. L'vov, G. Matone and A. M. Nathan, Phys. Rev. C **58** (1998) 1013 [arXiv:hep-ph/9803347].
- [89] B. R. Holstein, D. Drechsel, B. Pasquini and M. Vanderhaeghen, Phys. Rev. C **61** (2000) 034316 [arXiv:hep-ph/9910427].
- [90] R. P. Hildebrandt, H. W. Grieffhammer and T. R. Hemmert, Eur. Phys. J. A **20** (2004) 329 [arXiv:nucl-th/0308054].
- [91] R. P. Hildebrandt, H. W. Grieffhammer and T. R. Hemmert, Eur. Phys. J. A **46** (2010) 111 [arXiv:nucl-th/0512063].

- [92] R. P. Hildebrandt, “Elastic Compton Scattering from the Nucleon and Deuteron,” Ph.D. Thesis Technische Universität München (2005), arXiv:nucl-th/0512064.
- [93] H. W. Griebhammer and D. Shukla, Eur. Phys. J. A **46** (2010) 249 [arXiv:1006.4849 [nucl-th]]; erratum ibid. in press. Interactive *Mathematica 8.0* notebook available from hgrie@gwu.edu upon request.
- [94] B. R. Holstein, arXiv:hep-ph/0010129.
- [95] R. Miskimen, *Measuring the Spin-Polarizabilities of the Proton at HI $\gamma$ S*, presentation at the INT workshop on Soft Photons and Light Nuclei, 17 June 2008, and private communication.
- [96] H. W. Griebhammer, Prog. Part. Nucl. Phys. **55** (2005) 215 [arXiv:nucl-th/0411080].
- [97] J. W. Chen, X. d. Ji and Y. c. Li, Phys. Rev. C **71** (2005) 044321 [arXiv:nucl-th/0408004].
- [98] V. Bernard, N. Kaiser and U. G. Meißner, Int. J. Mod. Phys. E **4** (1995) 193 [arXiv:hep-ph/9501384].
- [99] H. R. Weller, M. W. Ahmed, H. Gao, W. Tornow, Y. K. Wu, M. Gai and R. Miskimen, Prog. Part. Nucl. Phys. **62** (2009) 257.
- [100] H. Weller et al., HIGS-E-18-09; H. Weller, private communication.
- [101] D. Choudhury and D. R. Phillips, Phys. Rev. C **71** (2005) 044002 [arXiv:nucl-th/0411001].
- [102] L. C. Maximon, Phys. Rev. C **39** (1989) 347.
- [103] G. E. Pugh et al., Phys. Rev. **105** (1957) 982.
- [104] C. L. Oxley, Phys. Rev. **110** (1958) 733.
- [105] L. G. Hyman, R. Ely, D. H. Frisch and M. A. Wahlig, Phys. Rev. Lett. **3** (1959) 93.
- [106] G. Bernardini et al., Nuovo Cimento **18** (1960) 1203.
- [107] V. I. Goldansky et al., Nucl. Phys. **18** (1960) 473.
- [108] P. Baranov et al., Phys. Lett. B **52** (1974) 122.
- [109] P. Baranov et al., Sov. J. Nucl. Phys. **21** (1975) 355.
- [110] J. W. DeWire, M. Feldmann, V. L. Highland, R. Littauer Phys. Rev. **124** (1961) 909.
- [111] P. S. Baranov, L. I. Slovokhotov, G. A. Sokol and L. N. Shtarkov, Sov. Phys. JETP **23** (1966) 242.
- [112] P. S. Baranov et al, Sov. J. Nucl. Phys. **3** (1966) 791.
- [113] E. R. Gray and A. O. Hanson, Phys. Rev. **160** (1967) 1212.
- [114] H. Genzel, M. Jung, R. Wedemeyer, and H. J. Weyer Z. Phys. A **279** (1976) 399.
- [115] A. Hüniger et al., Nucl. Phys. A **620** (1997) 385.
- [116] J. Peise et al., Phys. Lett. B **384** (1996) 37.
- [117] C. Molinari et al., Phys. Lett. B **371** (1996) 181.
- [118] S. Wolf et al., Eur. Phys. J. **A12** (2001) 231.
- [119] G. Galler et al., Phys. Lett. B **503** (2001) 245.
- [120] F. Wissmann et al., Nucl. Phys. A **660** (1999) 232.
- [121] M. Camen et al., Phys. Rev. **C65** (2002) 032202.
- [122] J. Tonnison, A. M. Sandorfi, S. Hoblit and A. M. Nathan, Phys. Rev. Lett. **80** (1998) 4382.
- [123] G. Blanpied et al., Phys. Rev. **C64** (2001) 025203.
- [124] G. Blanpied et al., Phys. Rev. Lett. **76** (1996) 1023.
- [125] G. Blanpied et al., Phys. Rev. Lett. **79** (1997) 4337.
- [126] G. Barbiellini et al., Phys. Rev. **174** (1968) 1665.
- [127] F. Wissmann, *Compton Scattering: Investigating the Structure of the Nucleon with Real Photons*, Springer Tracts in Modern Physics, Volume 200 (2004).
- [128] Yu. A. Alexandrov et al., Sov. J. Nucl. Phys. **44** (1986) 900.
- [129] L. Koester et al., Physica B **137** (1986) 2282.
- [130] J. Schmiedmayer, H. Rauch and P. Riehs, Phys. Rev. Lett. **61** (1988) 1065.
- [131] J. Schmiedmayer, P. Riehs, J. A. Harvey and N. W. Hill, Phys. Rev. Lett. **66** (1991) 1015.
- [132] L. Koester et al., Z. Phys. A **329** (1988) 229.
- [133] L. Koester et al., Phys. Rev. **C51** (1995) 3363.
- [134] T. L. Enik et al., Phys. At. Nucl. **60** (1997) 567.
- [135] A. Laptev et al., J. Nucl. Sci. Tech. Suppl. 2 (2002) 327 .
- [136] R. P. Hildebrandt, H. W. Griebhammer, T. R. Hemmert and D. R. Phillips, Nucl. Phys. A **748** (2005) 573 [arXiv:nucl-th/0405077].
- [137] H. W. Griebhammer, J. A. McGovern and D. R. Phillips, in preparation. Interactive *Mathematica*



8.0 notebook available from hgrie@gwu.edu upon request.

- [138] L. Myers, Ph.D. thesis, University of Illinois (2010).
- [139] K. Shoniyozov et al., in progress.
- [140] M. I. Levchuk, A. I. L'vov and V. A. Petrun'kin, *Few-Body Syst.* **16** (1994) 101.
- [141] M. I. Levchuk and A. I. L'vov, *Nucl. Phys. A* **674** (2000) 449 [arXiv:nucl-th/9909066].
- [142] A. I. L'vov, V. A. Petrun'kin and M. Schumacher, *Phys. Rev. C* **55** (1997) 359.
- [143] B. Pasquini, D. Drechsel, M. Vanderhaeghen, *Eur. Phys. J.* **ST198** (2011) 269 [arXiv:1105.4454 [hep-ph]].
- [144] D. M. Akhmedov and L. V. Filkov, *Yad. Fiz.* **33** (1981) 1083.
- [145] A. I. Lvov, *Sov. J. Nucl. Phys.* **34** (1981) 597 [*Yad. Fiz.* **34** (1981) 1075].
- [146] D. Drechsel, M. Gorchtein, B. Pasquini, M. Vanderhaeghen, *Phys. Rev.* **C61** (1999) 015204. [arXiv:hep-ph/9904290].
- [147] S. B. Gerasimov, *Sov. J. Nucl. Phys.* **2** (1966) 430.
- [148] S. D. Drell, A. C. Hearn, *Phys. Rev. Lett.* **16** (1966) 908.
- [149] M. Gell-Mann, M. L. Goldberger, W. E. Thirring, *Phys. Rev.* **95** (1954) 1612.
- [150] B. Pasquini, P. Pedroni, D. Drechsel, *Phys. Lett.* **B687** (2010) 160. [arXiv:1001.4230 [hep-ph]].
- [151] M. Schumacher, M. I. Levchuk, *Nucl. Phys.* **A858** (2011) 48. [arXiv:1104.3721 [hep-ph]].
- [152] G. Höhler, *Pion-nucleon scattering* (Springer, Berlin, 1983).
- [153] M. Schumacher, *Prog. Part. Nucl. Phys.* **55** (2005) 567 [arXiv:hep-ph/0501167].
- [154] M. Schumacher, *Eur. Phys. J.* **A30** (2006) 413. [hep-ph/0609040].
- [155] M. Schumacher, *Eur. Phys. J.* **A31** (2007) 327. [arXiv:0704.0200 [hep-ph]].
- [156] M. Schumacher, *Nucl. Phys.* **A826** (2009) 131. [arXiv:0905.4363 [hep-ph]].
- [157] B. R. Holstein, A. M. Nathan, *Phys. Rev.* **D49** (1994) 6101. [arXiv:hep-ph/9402248 [hep-ph]].
- [158] A. I. L'vov, A. M. Nathan, *Phys. Rev.* **C59** (1999) 1064. [nucl-th/9807032].
- [159] B. Pasquini, D. Drechsel and M. Vanderhaeghen, *Phys. Rev. C* **76** (2007) 015203 [arXiv:0705.0282 [hep-ph]].
- [160] S. Scherer, *Adv. Nucl. Phys.* **27** (2003) 277 [arXiv:hep-ph/0210398].
- [161] S. Scherer and M. R. Schindler, *Quantum chromodynamics and chiral symmetry*, *Lect. Notes Phys.* **830** (2012) 1, Springer pub.
- [162] J. Bijnens, *Prog. Part. Nucl. Phys.* **58** (2007) 521. [hep-ph/0604043].
- [163] V. Bernard, *Prog. Part. Nucl. Phys.* **60** (2008) 82 [arXiv:0706.0312 [hep-ph]].
- [164] S. R. Beane, P. F. Bedaque, W. C. Haxton, D. R. Phillips and M. J. Savage, in "At the frontier of particle physics", M. Shifman (ed.), World Scientific, 2001 [nucl-th/0008064].
- [165] P. F. Bedaque and U. van Kolck, *Ann. Rev. Nucl. Part. Sci.* **52** (2002) 339 [nucl-th/0203055].
- [166] E. Epelbaum, H. -W. Hammer, U.-G. Meißner, *Rev. Mod. Phys.* **81** (2009) 1773. [arXiv:0811.1338 [nucl-th]].
- [167] R. Machleidt and D. R. Entem, *Phys. Rept.* **503** (2011) 1 [arXiv:1105.2919 [nucl-th]].
- [168] D. R. Phillips, *J. Phys. GG* **36** (2009) 104004 [arXiv:0903.4439 [nucl-th]].
- [169] S. Weinberg, *Phys. Rev. Lett.* **17** (1966) 616.
- [170] J. Gasser, H. Leutwyler, *Annals Phys.* **158** (1984) 142.
- [171] G. Colangelo, J. Gasser and H. Leutwyler, *Nucl. Phys. B* **603** (2001) 125 [arXiv:hep-ph/0103088].
- [172] I. Caprini, G. Colangelo and H. Leutwyler, *Int. J. Mod. Phys. A* **21** (2006) 954 [arXiv:hep-ph/0509266].
- [173] J. Gasser, M. E. Sainio, A. Svarc, *Nucl. Phys.* **B307** (1988) 779.
- [174] E. E. Jenkins, A. V. Manohar, *Phys. Lett.* **B255** (1991) 558.
- [175] E. E. Jenkins, A. V. Manohar, In *Dobogokoe 1991, Proceedings, Effective field theories of the standard model* 113 and Calif. Univ. San Diego - UCSD-PTH 91-30 (91/10,rec.Dec.) 26 p. (201392) (see Conference Index).
- [176] A. Krause, *Helv. Phys. Acta* **63** (1990) 3.
- [177] G. Ecker, *Phys. Lett. B* **336** (1994) 508 [hep-ph/9402337].
- [178] G. Ecker and M. Mojžiš, *Phys. Lett. B* **365** (1996) 312 [hep-ph/9508204].
- [179] N. Fettes, U.-G. Meißner and S. Steininger, *Nucl. Phys. A* **640** (1998) 199 [hep-ph/9803266].
- [180] U.-G. Meißner, G. Muller and S. Steininger, *Annals Phys.* **279** (2000) 1 [hep-ph/9809446].
- [181] N. Fettes, U.-G. Meißner, M. Mojžiš a and S. Steininger, *Annals Phys.* **283** (2000) 273 [Erratum-ibid. **288** (2001) 249] [hep-ph/0001308].



- [182] V. Bernard, N. Kaiser, J. Kambor and U. G. Meißner, Nucl. Phys. B **388** (1992) 315.
- [183] V. Bernard, N. Kaiser, U. G. Meißner, Phys. Rev. Lett. **67** (1991) 1515.
- [184] V. Lensky, V. Pascalutsa, Eur. Phys. J. **C65** (2010) 195. [arXiv:0907.0451 [hep-ph]].
- [185] V. Bernard, N. Kaiser, J. Kambor and U. G. Meißner, Phys. Rev. D **46** (1992) 2756.
- [186] M. N. Butler and M. J. Savage, Phys. Lett. B **294** (1992) 369 [hep-ph/9209204].
- [187] K. B. Vijaya Kumar, A. Faessler, T. Gutsche, B. R. Holstein and V. E. Lyubovitskij, Phys. Rev. D **84** (2011) 076007 [arXiv:1108.0331 [hep-ph]].
- [188] A. Aleksejevs and S. Barkanova, J. Phys. G **38** (2011) 035004 [arXiv:1010.3457 [nucl-th]].
- [189] V. Bernard, N. Kaiser, A. Schmidt and U. G. Meißner, Phys. Lett. B **319** (1993) 269 [hep-ph/9309211].
- [190] X. -D. Ji, C. -W. Kao and J. Osborne, Phys. Rev. D **61** (2000) 074003 [hep-ph/9908526].
- [191] K. B. Vijaya Kumar, J. A. McGovern and M. C. Birse, hep-ph/9909442.
- [192] K. B. Vijaya Kumar, J. A. McGovern and M. C. Birse, Phys. Lett. B **479** (2000) 167 [hep-ph/0002133].
- [193] G. C. Gellas, T. R. Hemmert and U.-G. Meißner, Phys. Rev. Lett. **85** (2000) 14 [nucl-th/0002027].
- [194] M. C. Birse, X. -D. Ji and J. A. McGovern, Phys. Rev. Lett. **86** (2001) 3204 [nucl-th/0011054].
- [195] G. C. Gellas, T. R. Hemmert and U. G. Meißner, Phys. Rev. Lett. **86** (2001) 3205.
- [196] V. Bernard, N. Kaiser, U. G. Meißner and A. Schmidt, Z. Phys. A **348** (1994) 317 [hep-ph/9311354].
- [197] J. A. McGovern, Phys. Rev. C **63** (2001) 064608 [Erratum-ibid. C **66** (2002) 039902] [nucl-th/0101057].
- [198] S. R. Beane, M. Malheiro, J. A. McGovern, D. R. Phillips, U. van Kolck, Phys. Lett. **B567** (2003) 200. [arXiv:nucl-th/0209002].
- [199] S. R. Beane, M. Malheiro, J. A. McGovern, D. R. Phillips and U. van Kolck, Nucl. Phys. A **747** (2005) 311 [arXiv:nucl-th/0403088].
- [200] T. R. Hemmert, B. R. Holstein and J. Kambor, Phys. Lett. B **395** (1997) 89 [hep-ph/9606456].
- [201] T. R. Hemmert, B. R. Holstein and J. Kambor, J. Phys. G **24** (1998) 1831 [hep-ph/9712496].
- [202] M. N. Butler, M. J. Savage and R. P. Springer, Nucl. Phys. B **399** (1993) 69 [hep-ph/9211247].
- [203] T. R. Hemmert, B. R. Holstein and J. Kambor, Phys. Rev. D **55** (1997) 5598 [hep-ph/9612374].
- [204] T. R. Hemmert, B. R. Holstein, J. Kambor and G. Knochlein, Phys. Rev. D **57** (1998) 5746 [nucl-th/9709063].
- [205] V. Pascalutsa, D. R. Phillips, Phys. Rev. **C67** (2003) 055202. [nucl-th/0212024].
- [206] V. Pascalutsa and M. Vanderhaeghen, Phys. Rev. D **73** (2006) 034003 [arXiv:hep-ph/0512244].
- [207] V. Pascalutsa, M. Vanderhaeghen and S. N. Yang, Phys. Rept. **437** (2007) 125 [arXiv:hep-ph/0609004].
- [208] N. C. Mukhopadhyay, A. M. Nathan, L. Zhang, Phys. Rev. **D47** (1993) 7.
- [209] V. Pascalutsa, Phys. Rev. D **58** (1998) 096002 [hep-ph/9802288].
- [210] V. Pascalutsa and R. Timmermans, Phys. Rev. C **60** (1999) 042201 [nucl-th/9905065].
- [211] V. Lensky and V. Pascalutsa, Pisma Zh. Eksp. Teor. Fiz. **89** (2009) 127 [JETP Lett. **89** (2009) 108] [arXiv:0803.4115 [nucl-th]].
- [212] P. S. Baranov, A. I. Lvov, V. A. Petrunkin and N. L. Shtarkov, Phys. Part. Nucl. **32** (2001) 376.
- [213] G. D'Agostini Nuclear Instruments and Methods in Physics Research A **346** (1994) 306.
- [214] J. A. McGovern, H. W. Grieffhammer and D. R. Phillips, in preparation.
- [215] A. Gasparyan, M. F. M. Lutz, Nucl. Phys. **A848** (2010) 126. [arXiv:1003.3426 [hep-ph]].
- [216] A. M. Gasparyan, M. F. M. Lutz and B. Pasquini, Nucl. Phys. A **866** (2011) 79 [arXiv:1102.3375 [hep-ph]].
- [217] S. Kondratyuk, O. Scholten, Phys. Rev. **C64** (2001) 024005. [nucl-th/0103006].
- [218] S. Kondratyuk, O. Scholten, Phys. Rev. **C65** (2002) 038201. [nucl-th/0109038].
- [219] J. W. Chen, Nucl. Phys. A **653** (1999) 375 [arXiv:nucl-th/9810021].
- [220] J. W. Chen, H. W. Grieffhammer, M. J. Savage and R. P. Springer, Nucl. Phys. A **644** (1998) 221 [arXiv:nucl-th/9806080].
- [221] J. W. Chen, H. W. Grieffhammer, M. J. Savage and R. P. Springer, Nucl. Phys. A **644** (1998) 245 [arXiv:nucl-th/9809023].
- [222] S. R. Beane, M. Malheiro, D. R. Phillips and U. van Kolck, Nucl. Phys. A **656** (1999) 367

- [arXiv:nucl-th/9905023].
- [223] S. Weinberg, Phys. Lett. **B251** (1990) 288.
- [224] S. Weinberg, Nucl. Phys. B **363** (1991) 3.
- [225] D. Eiras and J. Soto, Eur. Phys. J. A **17** (2003) 89 [nucl-th/0107009].
- [226] A. Nogga, R. G. E. Timmermans and U. van Kolck, Phys. Rev. C **72** (2005) 054006 [arXiv:nucl-th/0506005].
- [227] M. Pavon Valderrama and E. Ruiz Arriola, Phys. Rev. C **74** (2006) 064004 [Erratum-ibid. C **75** (2007) 059905] [nucl-th/0507075].
- [228] M. C. Birse, Phys. Rev. C **74** (2006) 014003 [arXiv:nucl-th/0507077].
- [229] C. J. Yang, C. Elster and D. R. Phillips, Phys. Rev. C **80** (2009) 034002 [arXiv:0901.2663 [nucl-th]].
- [230] S. R. Beane, P. F. Bedaque, M. J. Savage and U. van Kolck, Nucl. Phys. A **700** (2002) 377 [nucl-th/0104030].
- [231] S. R. Beane, D. B. Kaplan and A. Vuorinen, Phys. Rev. C **80** (2009) 011001 [arXiv:0812.3938 [nucl-th]].
- [232] M. C. Birse, arXiv:1012.4914 [nucl-th].
- [233] B. Long and C. J. Yang, Phys. Rev. C **85** (2012) 034002. [arXiv:1111.3993 [nucl-th]].
- [234] M. P. Valderrama, Phys. Rev. C **84** (2011) 064002. [arXiv:1108.0872 [nucl-th]].
- [235] E. Epelbaum and U.-G. Meißner, nucl-th/0609037.
- [236] D. R. Entem and R. Machleidt, Phys. Rev. C **68** (2003) 041001 [nucl-th/0304018].
- [237] E. Epelbaum, W. Glöckle and U.-G. Meißner, Nucl. Phys. A **747** (2005) 362 [nucl-th/0405048].
- [238] U. van Kolck, Phys. Rev. C **49** (1994) 2932.
- [239] V. Bernard, E. Epelbaum, H. Krebs and U.-G. Meißner, Phys. Rev. C **77** (2008) 064004 [arXiv:0712.1967 [nucl-th]].
- [240] V. Bernard, E. Epelbaum, H. Krebs and U.-G. Meißner, Phys. Rev. C **84** (2011) 054001 [arXiv:1108.3816 [nucl-th]].
- [241] H. W. Griebhammer, In *Proceedings of 11th International Conference on Meson-Nucleon Physics and the Structure of the Nucleon (MENU 2007), Julich, Germany, 10-14 Sep 2007*, p. 141 [arXiv:0710.2924 [nucl-th]].
- [242] H. W. Griebhammer, *Introduction to Effective Field Theories*, lectures at the US National Nuclear Physics Summer School 2008, George Washington University, Washington (DC), USA, 16th – 27th June 2008, available at <http://home.gwu.edu/~hgrie/lectures/lectures.0806.NNPSS2008-GW.djvu>.
- [243] J. L. Friar, Phys. Rev. C **16** (1977) 1504.
- [244] H. Arenhövel, Z. Phys. A **297** (1980) 129.
- [245] M. Weyrauch and H. Arenhövel, Nucl. Phys. A **408** (1983) 425.
- [246] M. Weyrauch, Phys. Rev. C **38** (1988) 611.
- [247] M. Weyrauch, Phys. Rev. C **41** (1990) 880.
- [248] T. Wilbois, P. Wilhelm, H. Arenhövel, Few-Body Syst. Suppl. **9** (1995), 263.
- [249] J. Karakowski, arXiv:nucl-th/9901011.
- [250] J. J. Karakowski and G. A. Miller, Phys. Rev. C **60** (1999) 014001 [arXiv:nucl-th/9901018].
- [251] M. I. Levchuk and A. I. L'vov, Few-Body Syst. Suppl. **9** (1995), 439.
- [252] H. Arenhövel and M. Weyrauch, Nucl. Phys. A **457** (1986) 573.
- [253] T. Ericson and W. Weise, Pions and Nuclei, Clarendon Press, Oxford (1988).
- [254] E. Epelbaum, W. Gloeckle, U.-G. Meißner, Nucl. Phys. A **671** (2000) 295. [arXiv:nucl-th/9910064 [nucl-th]].
- [255] D. R. Phillips, T. D. Cohen, Nucl. Phys. A **668** (2000) 45. [nucl-th/9906091].
- [256] R. B. Wiringa, V. G. J. Stoks, R. Schiavilla, Phys. Rev. C **51** (1995) 38.
- [257] V. G. Stoks, R. A. Klomp, C. P. Terheggen and J. J. de Swart, Phys. Rev. C **49** (1994) 2950.
- [258] T.-S. Park, K. Kubodera, D.-P. Min and M. Rho, Nucl. Phys. A **646** (1999) 83.
- [259] E. Braaten and H. W. Hammer, Phys. Rept. **428** (2006) 259 [arXiv:cond-mat/0410417].
- [260] L. Platter, Few Body Syst. **46** (2009) 139 [arXiv:0904.2227 [nucl-th]].
- [261] D. B. Kaplan, Nucl. Phys. B **494** (1997) 471 [arXiv:nucl-th/9610052].
- [262] P. F. Bedaque and H. W. Griebhammer, Nucl. Phys. A **671** (2000) 357 [arXiv:nucl-th/9907077].

- [263] H. W. Griebhammer and G. Rupak, Phys. Lett. B **529** (2002) 57 [arXiv:nucl-th/0012096].
- [264] S. R. Beane and M. J. Savage, Nucl. Phys. A **694** (2001) 511 [arXiv:nucl-th/0011067].
- [265] X. d. Ji and Y. c. Li, Phys. Lett. B **591** (2004) 76 [arXiv:nucl-th/0311035].
- [266] J. W. Chen, G. Rupak and M. J. Savage, Nucl. Phys. A **653** (1999) 386 [arXiv:nucl-th/9902056].
- [267] D. R. Phillips, G. Rupak and M. J. Savage, Phys. Lett. B **473** (2000) 209 [arXiv:nucl-th/9908054].
- [268] J. L. Friar and S. Fallieros, Phys. Rev. C **29** (1984) 232.
- [269] J. G. Lucas and M. L. Rustgi, Nucl. Phys. A **112** (1968) 503.
- [270] J. L. Friar and G. L. Payne, Phys. Rev. C **55** (1997) 2764 [arXiv:nucl-th/9702019].
- [271] J. L. Friar and G. L. Payne, Phys. Rev. C **72** (2005) 014004 [arXiv:nucl-th/0503045].
- [272] N. L. Rodning, L. D. Knutson, W. G. Lynch and M. B. Tsang, Phys. Rev. Lett. **49** (1982) 909.
- [273] J. W. Chen, X. d. Ji and Y. c. Li, Phys. Lett. B **620** (2005) 33 [arXiv:nucl-th/0408003].
- [274] H. W. Griebhammer and D. Shukla, PoS C **D09** (2009) 060 [arXiv:0910.0053 [nucl-th]].
- [275] D. B. Kaplan, M. J. Savage and M. B. Wise, Phys. Lett. B **424** (1998) 390 [arXiv:nucl-th/9801034].
- [276] S. Fleming, T. Mehen and I. W. Stewart, Nucl. Phys. A **677** (2000) 313 [arXiv:nucl-th/9911001].
- [277] R. H. Capps, Phys. Rev. **108** (1957) 1032.
- [278] R. H. Capps, Phys. Rev. **106** (1957) 1031.
- [279] R. L. Schult and R. H. Capps, Phys. Rev. **119** (1960) 377.
- [280] A. Tenore and A. Verganelakis, Nuovo Cim. **35** (1965) 26.
- [281] S. Pokorski, Nuovo Cim. **50A** (1967) 957.
- [282] R. Machleidt, K. Holinde, C. Elster, Phys. Rept. **149** (1987) 1.
- [283] M. I. Levchuk and A. I. L’vov, in *Proceedings of the XII International Seminar on Electromagnetic Interactions of Nuclei (EMIN-2009), Moscow, September 2009*, p. 120.
- [284] M. I. Levchuk and A. I. L’vov, in *Proceedings of Internatinal School-Seminar “Acutal Problems of Microworld Physics” , Gomel, Belarus, July 2009*, p. 121.
- [285] M. I. Levchuk, Few Body Syst. **19** (1995) 77.
- [286] F. Wissmann, M. Schumacher, M. I. Levchuk, Eur. Phys. J. **A1** (1998) 193.
- [287] A. I. L’vov, V. A. Petrun’kin, M. Schumacher, Phys. Rev. **C55** (1997) 359.
- [288] A. I. L’vov, private communication.
- [289] H. Weller et al., HIGS Proposal P-18-09, Measuring Electric and Magnetic Polarizabilities of the Neutron using  $d(\gamma, \gamma)d$  (2009).
- [290] M. Ahmed et al., HIGS Proposal P-06-10, A Sum-Rule Independent Measurement of the Proton Polarizabilities (2010).
- [291] R. Miskimen et al., HIGS Proposal P-06-09, Measuring the Spin Polarizabilities of the Proton in Double-Polarized Real Compton Scattering (2009).
- [292] H. Gao et al., HIGS Proposal P-07-10, Compton Scattering from a High-Pressure Polarized  $^3\text{He}$  Target at HIGS (2010).
- [293] G. Feldman et al., HIGS Proposal P-08-10, Compton Scattering from  $^6\text{Li}$  (2010).
- [294] O. Yevetska et al., Nucl. Inst. and Meth. A, **618** (2010) 160.
- [295] G. Feldman et al., MAX-Lab Proposal 10-02, Compton Scattering from Deuterium above the Pion Production Threshold (2010).
- [296] The MAX IV Project, <http://www.maxlab.lu.se/maxlab/max4/index.html>, (2011).
- [297] K. Fissum, private communication (2011).
- [298] D. Hornidge, E. J. Downie, J. R. M. Annand and I. J. D. MacGregor, Mainz Proposal A2-11/09, Measurement of the Proton Spin Polarizabilities (2009).
- [299] E. Downie, private communication (2011).
- [300] V. Baru, C. Hanhart, A. E. Kudryavtsev and U.-G. Meißner, Phys. Lett. B **589** (2004) 118 [arXiv:nucl-th/0402027].
- [301] V. Lensky, V. Baru, J. Haidenbauer, C. Hanhart, A. E. Kudryavtsev and U.-G. Meißner, Phys. Lett. B **648** (2007) 46 [arXiv:nucl-th/0608042].
- [302] V. Lensky, V. Baru, J. Haidenbauer, C. Hanhart, A. E. Kudryavtsev and U.-G. Meißner, Eur. Phys. J. A **26** (2005) 107 [arXiv:nucl-th/0505039].
- [303] V. Lensky, J. Haidenbauer, C. Hanhart, V. Baru, A. E. Kudryavtsev and U.-G. Meißner, Int. J. Mod. Phys. A **22** (2007) 591 [arXiv:nucl-th/0609007].
- [304] V. Lensky, V. Baru, E. Epelbaum, C. Hanhart, J. Haidenbauer, A. E. Kudryavtsev, U.-G. Meißner,

- Eur. Phys. J. **A33** (2007) 339 [arXiv:0704.0443 [nucl-th]].
- [305] V. Baru, C. Hanhart, M. Hoferichter, B. Kubis, A. Nogga and D. R. Phillips, Nucl. Phys. A **872** (2011) 69 [arXiv:1107.5509 [nucl-th]].
- [306] A. N. Kvinikhidze, B. Blankleider, E. Epelbaum, C. Hanhart and M. P. Valderrama, Phys. Rev. C **80** (2009) 044004 [arXiv:0904.4128 [nucl-th]].
- [307] S. Pastore, L. Girlanda, R. Schiavilla, M. Viviani and R. B. Wiringa, Phys. Rev. C **80** (2009) 034004 [arXiv:0906.1800 [nucl-th]].
- [308] S. Kolling, E. Epelbaum, H. Krebs, U.-G. Meißner, Phys. Rev. **C80** (2009) 045502. [arXiv:0907.3437 [nucl-th]].
- [309] S. Kolling, E. Epelbaum, H. Krebs, U.-G. Meißner, Phys. Rev. **C84** (2011) 054008. [arXiv:1107.0602 [nucl-th]].
- [310] C.-J. Yang, “Subtractive renormalization of the NN interaction in chiral effective theory and the deuteron electro-disintegration calculation”, Ph. D. thesis, Ohio University (2010).
- [311] G. Bampa, W. Leidemann and H. Arenhovel, Phys. Rev. C **84** (2011) 034005 [arXiv:1107.2320 [nucl-th]].
- [312] W. Leidemann, private communication (2011).